POLITECNICO DI TORINO

Collegio di Ingegneria Meccanica, Aerospaziale e dell'Autoveicolo

Corso di Laurea Magistrale in
INGEGNERIA MECCANICA (MECHANICAL ENGINEERING)

Master thesis

Machine Learning Assisted Laser-Powder Bed Fusion Process Optimization for AISI 316L-Cu Alloy

Supervisor
Prof. Abdollah Saboori

Candidate
Alireza Moradi Ghasemabadi

December 2024

Abstract

Metal Additive Manufacturing (AM) has revolutionized the production of complex metal components by enabling the fabrication of intricate geometries with high precision. This technology's potential can be significantly enhanced by integrating artificial intelligence (AI) methods, particularly Machine Learning (ML), which offers advanced capabilities in establishing complex interrelationships and improving system and product quality control. ML algorithms present a transformative opportunity to address manufacturing challenges, optimize resource consumption, and enhance process efficiency by exploring the intricate linkages between process parameters, material properties, part geometry, microstructural characteristics, and their resultant properties. In metal AM processes such as Directed Energy Deposition (DED) and Laser Powder Bed Fusion (L-PBF), ML applications extend beyond process optimization to include defect detection, in-situ monitoring, and the enhancement of manufacturability and repeatability of components. This thesis investigates optimizing critical process parameters in L-PBF using ML techniques to establish a relationship between process parameters and defect content of AISI 316L-2.5%Cu. Recognizing these relationships enables the optimization of process parameters to attain specific objectives, such as high productivity, minimizing defect content, or low surface roughness. This optimization method facilitates applications, balancing productivity and quality, allowing the selection of parameters that satisfy both criteria. The prediction accuracy of seven ML algorithms, Bayesian Regression (BR), Decision Tree Regressor (DTR), Gradient Boosting Regressor (GBR), Gaussian Process Regressor (GPR), K-Nearest Neighbors Regressor (KNN), Random Forest Regressor (RFR), and Support Vector Regressor (SVR) were analyzed. Following the assessment of multiple models with varying training and testing sizes for the density of samples, the Support Vector Regression (SVR) model has been identified as the most effective model. The optimized process parameters, derived from the best-performing ML model prediction, demonstrated an accurate relationship between process parameters and defect content for achieving relative density values above 99.5% or high productivity. The findings of this thesis validate the effectiveness of ML in enhancing AM processes and underscore the potential of data-driven methodologies to advance the field of laser-based AM.

Keywords: Additive Manufacturing, Machine learning, Laser Powder Bed Fusion, Process parameter optimization

Acknowledgments

I would like to extend my deepest gratitude to my esteemed supervisor, Dr. Saboori, for his invaluable guidance, expertise, and unwavering support throughout this journey. His insights and encouragement have been instrumental in the completion of this thesis. I am genuinely grateful for his dedication and mentorship, which have made this achievement possible.

To my beloved wife, I owe my heartfelt appreciation for her constant encouragement and understanding. Her unwavering faith in me and her kindness have been my strength, providing the inspiration I needed during countless hours of study and writing. Thank you for always believing in me.

I am also profoundly grateful to my parents, whose love and support have been a steady source of motivation, even from afar. Their sacrifices, steadfast belief in my potential, and the values they instilled in me have been the foundation of my perseverance. I feel incredibly fortunate to have them in my life, always cheering me on.

To my friends and colleagues, thank you for being part of this journey with me. Your support, thoughtful discussions, and shared moments have enriched my research experience in ways I will always cherish.

Finally, I would like to express my sincere thanks to the faculty and staff of the Integrated Additive Manufacturing Lab at Politecnico di Torino. Their resources and collaborative environment have provided me with the foundation necessary to bring this research to life.

Table of Contents

Tables

Figures

Table of Abbreviations

Abbreviation	Definition
AM	Additive Manufacturing
BR	Bayesian Regression
CNN	Convolutional Neural Network
DA	Discriminant Analysis
DED	Directed Energy Deposition
DEM	Discrete Element Method
DEM	Discrete Element Method
DMLS	Direct Metal Laser Sintering
DTR	Decision Tree Regression
EB-PBF	Electron Beam Powder Bed Fusion
EBM	Electron Beam Melting
ELM	Extreme Learning Machines
GA	Genetic Algorithm
GMA	Gas Metal Arc
IoT	Internet of Things
k-NN	k-Nearest Neighbor
LBAM	Laser Beam Additive Manufacturing
L-PBF	Laser Powder Bed Fusion
ML	Machine Learning
NN	Neural Network
PA	Plasma Arc
PBF	Powder Bed Fusion
PSP	Process-Structure-Property
RHEA	Refractory High Entropy Alloys
ROC	Receiver Operating Characteristic
SeDANN	Sequential Decision Analysis Neural Network
SHS	Selective Heat Sintering
SLS	Selective Laser Sintering
SVR	Support Vector Regression
UQ	Uncertainty Quantification
CAM	Computer-Aided Manufacturing
CAD	Computer-Aided Design
W-EDM	Wire Electrical Discharge Machine
XCT	X-ray Computed Tomography
UTL	Unsupervised Transfer Learning
ANN	Artificial Neural Network
AE	Auto Encoder
OM	Optical Microscope
GPR	Gaussian Process Regression
RFR	Random Forest Regression
GBR	Gradient Boosting Regression
MAE	Mean Absoulute Error
MSE	Mean Squared Error
HAZ	Heat Affected Zone
UTS	Ultimate Tensile Strenght

1. Introduction

Additive manufacturing (AM) is an innovative approach that constructs materials layer by layer, allowing for the creation of complex geometries from CAD designs [1]. AM enhances design flexibility and allows the processing of various materials, including polymers, metals, ceramics, and composites[2]. In contrast to traditional manufacturing methods, AM offers significant benefits, including enhanced material utilization efficiency and the ability to produce structures that closely approximate their final shapes. Regarding complexity, AM facilitates the creation of complex geometries and unique designs, which traditional manufacturing methods cannot accomplish[3]. Electron beam melting (EBM) and selective laser melting (SLM) are two advanced powder bed fusion (PBF) AM techniques. SLM, also known as L-PBF, utilizes high-power lasers to melt powder layer by layer selectively. In contrast, EBM involves micro-melting specific areas of partially sintered powder, leading to distinct microstructures. Both techniques can yield exceptional mechanical properties when process parameters are carefully optimized[4–6]. Although the L-PBF process has demonstrated effectiveness in the rapid manufacturing of complex components, the potential applications of printed components can be limited because of some problems, such as the small value of densification[7], elevated surface roughness[8], tensile residual stresses[9], and anisotropic structures[10–12]. However, these problems can be resolved by optimizing and tuning process parameters to achieve the desired quality of LPBF-produced parts [11]. Achieving this goal requires an in-depth investigation of all critical parameters and their influence on the mechanical and microstructural properties of the fabricated components. Even though more than 130 distinct process parameters can influence the LPBF process[13], factors such as laser power, scanning speed, hatch spacing, and layer thickness are recognized as having the most significant impact on the characteristics of the printed structures [14,15]. Metal AM also has a limited number of compatible materials that restrict its applicability across various fields, especially in specialized industries requiring specific material properties, such as the biomedical sector. To address this issue, considerable effort has been dedicated to developing novel alloys with customizable properties. This thesis focuses on a 316L stainless steel alloy with a 2.5% copper addition, which is used to possess antibacterial properties, making it appropriate for applications within the biotechnology field.

ML techniques fill the gap between the requirement for accurate models and the need for repeated and extensive experimentation. When ML is combined with high-throughput trials, the search for optimal process parameters is accelerated while costs associated with experimentation and testing are significantly reduced. Unlike traditional physical models, ML algorithms have demonstrated their ability to generate valuable insights by training on datasets and making predictions based on acquired knowledge. Among ML approaches, supervised learning is particularly notable, as it uses labeled data divided into training and testing sets, with the primary aim of applying models that establish relationships between features and the target variable in the dataset. Supervised ML can further be categorized into two types: regression, which predicts continuous quantities, and classification, which involves predicting discrete class labels [16,17]. Regression models were used because the target variable (relative density) is continuous in this research.

The primary objective of this thesis is to demonstrate the capability of ML to generate precise predictions of process parameter defect content relation, especially when different priorities, such as productivity or surface quality, are prioritized. This predictive ability allows for accurately customizing the AM process to meet specific requirements without additional density testing, thereby improving the optimization process. This emphasis is directly associated with enhancing efficiency in AM and seeks to make substantial contributions to progress in this field of study. To reach these goals, the accuracy of seven supervised ML algorithms in predicting the process parameter defect content relation of AISI316L-Cu stainless steel specimens manufactured by L-PBF using different combinations of process parameters, including laser power, scanning speed, and hatch distance with constant layer thickness. The performance of each model was evaluated using R^2, MAE, and MSE error estimators.

Chapter 2, titled "State of the Art," thoroughly investigates the current ML approach and AM technologies, PBF and DED. As mentioned, the final quality of manufactured components is directly influenced by various parameters, including laser power, scan speed, hatch distance, and powder characteristics, which are defined in Chapter 2. This chapter also reviews the different categories of ML techniques, such as supervised, unsupervised, semi-supervised, and reinforcement learning, and their application to enhance AM processes. It also highlights recent developments in which researchers have applied ML algorithms to improve the efficiency of AM. These advancements include the optimization of parameters for enhanced mechanical properties, the regulation of geometric deviations, and the in-situ monitoring of defect detection.

Comprehensive descriptions of the methodologies employed in this research are available in Chapter 3, Materials and Methods. This chapter outlines the procedures implemented in sample modeling, including the experimental design framework established to modify the process parameter ranges and define sample fabrication methods, concentrating on how different process conditions affect the material properties. The characterization techniques employed to assess the mechanical and microstructural properties are explained in detail in this chapter, including X-ray computed tomography (XCT), Archimedes method, and metallographic techniques. XCT provides a non-destructive method for analyzing internal porosity. Archimedes density measurements, conversely, calculate the component overall density. Moreover, metallographic techniques are employed to measure porosity percentage and sample density by microstructural analysis. Comprehensive parameter optimization can be reached by using these characterization techniques, as they provide the necessary data for training and evaluating ML models.

Chapter four, "Results and Discussion," presents the results from the experiments and the evaluation of the ML models. The initial section of the chapter outlines the procedures for data acquisition and preprocessing, along with an outline of the data partitioning for training and testing purposes. The hyperparameter tuning process is clarified, wherein several ML models were applied to analyze the relationship between the process parameters and the sample outcomes. This chapter also addresses selecting the best model based on evaluation metrics to

achieve an optimized parameter set that fulfills the desired objectives. It examines how variations in process parameters influence porosity content within the samples.

The concluding chapter, entitled "Conclusion and Future Perspective," provides a summary of the thesis's key contributions and discusses potential avenues for future research. This chapter explains the significance of employing ML to enhance AM technologies. It also emphasizes the potential for AM to enhance sustainability and resource efficiency as ML techniques advance. The integration of larger, more complex datasets may yield models that are significantly more accurate and predictive. The results presented herein emphasize the capacity of ML and AM to transform material development, enabling the production of customized, high-performance components across various industries.

This thesis aims to advance the field of intelligent manufacturing by proposing a systematic methodology for developing materials in AM. This methodology will facilitate more efficient, sustainable, and adaptable production processes.

2. State of the art

AM has offered a substantial revolution in the manufacturing process of metal components. This technology facilitates the production of complex geometries with great precision. It also provides the capability to generate localized alterations in microstructure and properties through targeted adjustments in the manufacturing process. The persistent issue of achieving consistent and high-quality outcomes for varied applications persists despite the considerable efforts made by individuals over the years that have resulted in the commercialization of metal AM technologies [18]. Direct metal AM processes can primarily be classified into two major technological categories: PBF and DED. These two direct AM processes have become increasingly prominent in academic research and industrial applications, making them the primary focus of interest. In DED, material is supplied through a moving nozzle, while PBF adds thin layers of powder after each fusion step. Both methods involve melting the material with a heat source like a laser or electron beam [10,19]. In recent years, extensive research has been conducted to enhance the efficiency of AM processes. One of the most effective tools for improving AM performance is using artificial intelligence (AI). AI technologies, such as ML, automation, robotics, machine vision, data mining, extensive data analysis, and expert systems, have presented their efficacy in manufacturing [20]. ML is a powerful tool for improving the quality and efficiency of metal AM [21]. It can also play an important role in enhancing the quality of printed components, particularly when basic physical principles are not well known but data on process variables, alloy properties, and product characteristics are accessible [22]. Integrating ML with AM can detect defects early, reduce waste, optimize input and output characteristics, and improve speed and accuracy, ultimately enhancing the quality [23].

ML methods have gained considerable interest for their exceptional performance in various data-related tasks, including regression, classification, and clustering. These approaches can be classified into supervised, unsupervised, semi-supervised, and reinforcement learning based on the extent and nature of supervision needed during the training process [24]. Integrating these powerful ML techniques presents an exciting opportunity to revolutionize manufacturing processes, tackle challenges, and optimize resource utilization. By considering the parameters of the AM process and the material properties, part geometry, and microstructural characteristics as inputs for ML algorithms, it becomes possible to establish a relationship known as Process-Structure-Property (PSP). Various linkages and correlations may be observed among data, including optimizing processing parameters and property prediction, cost estimation, defect identification, in-situ monitoring, and controlling geometric deviation [25].

Consequently, this thesis will comprehensively analyze the applications of ML in two laser-based AM technologies, L-PBF and DED. The papers under discussion within the context of this review text provide an overarching view of ML applications in AM. However, it is worth noting that the number of papers focusing on ML general applications in AM [18,25,26] is notably higher than those that specifically address L-PBF [27–29] or DED [30–32], which tend to be less frequent in the literature. There two main reasons for the selective analysis approach in this chapter. Firstly, a deeper and more comprehensive understanding of the practical

applications of ML in L-PBF and DED is facilitated by focusing on them. The unique difficulties and challenges associated with L-PBF and DED, which may be overlooked in broader studies, can be explored by this approach. Secondly, generalization problems can be avoided by concentrating on these two processes. By emphasizing L-PBF and DED, more actionable insights can be provided into how ML can be effectively applied in these specialized areas. This approach enables real-world challenges to be addressed and innovative solutions to be offered.

Fig. 1, extracted from the Scopus database using the keywords listed in Table 1, shows a significant increase in the number of articles on integrating ML in AM. This surge can be attributed to the growing importance of the subject. The chart generally demonstrates the broad application of ML in AM.

Table 1. Keywords used to search and obtain data from the Scopus database

Application of ML in AM	Application of ML in L-PBF	Application of ML in DED
(TITLE-ABS-KEY (machine AND learning AND in AND additive AND manufacturing) AND (LIMIT-TO (SUBJAREA, "ENGI")) AND (LIMIT-TO (DOCTYPE, "ar") OR LIMIT-TO (DOCTYPE, "cp") OR LIMIT-TO (DOCTYPE, "re")) AND (LIMIT-TO (LANGUAGE, "English")))	(TITLE-ABS-KEY (machine AND learning AND in AND laser AND powder AND bed AND fusion) AND (LIMIT-TO (SUBJAREA, "ENGI")) AND (LIMIT-TO (DOCTYPE, "ar") OR LIMIT-TO (DOCTYPE, "cp") OR LIMIT-TO (DOCTYPE, "re")) AND (LIMIT-TO (LANGUAGE, "English")))	TITLE-ABS-KEY (machine AND learning AND in AND directed AND energy AND deposition) AND (LIMIT-TO (SUBJAREA, "ENGI")) AND (LIMIT-TO (DOCTYPE, "ar") OR LIMIT-TO (DOCTYPE, "cp") OR LIMIT-TO (DOCTYPE, "re")) AND (LIMIT-TO (LANGUAGE, "English"))).

Furthermore, it is worth noting that the number of articles studied for DED is significantly lower than L-PBF. Despite this, both processes are the focus of this thesis. This approach is motivated by the desire to provide a more detailed and specialized analysis of these AM techniques, recognizing their unique requirements and challenges.

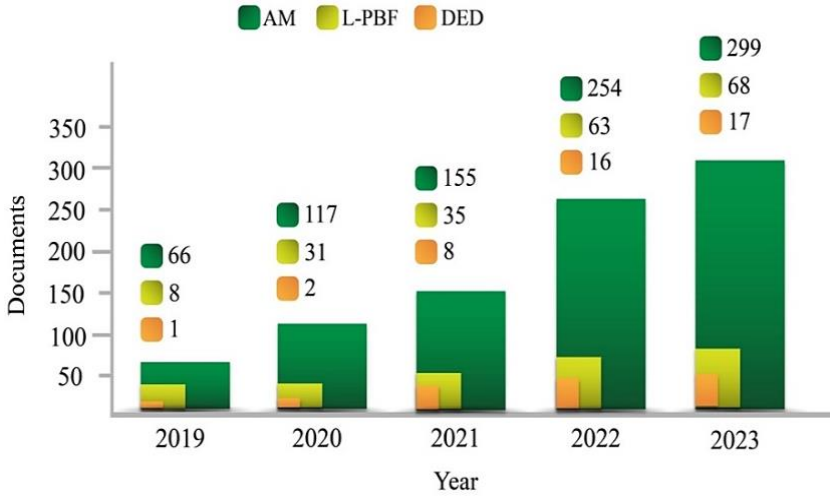

Fig. 1.The number of published papers on the application of ML in various AM methods as a function of publication year. The data was extracted according to the keywords tabulated in Table 1.

2.1. Additive Manufacturing

Metallic components can be produced via direct metal AM immediately after being designed in a single processing step [33]. During the AM process, complex shape components are built layer upon layer following a digital layout. This distinct characteristic directly produces complex shape components from the design, eliminating the need for costly tooling or shaping tools like punches, dies, or casting molds and diminishing the number of traditional processing stages [10]. Manufactured metallic parts are utilized in various industries, including healthcare, energy, automotive, marine, and consumer products [34]. Examples of these components include metal implants designed for specific patients [35], turbine blades with cooling channels [36], manifolds for engines and turbines, and lattice structures and truss networks optimized for a better strength-to-weight ratio [37].

According to ASTM F42, AM processes can be broadly categorized into seven classes: Vat photopolymerization (VP), Material Extrusion (ME), Material Jetting (MJ), Binder Jetting (BJ), PBF, DED, and Sheet Lamination (SL) [38]. PBF and DED methods differ based on the feedstock (powder or wire) and the heat source, which can be a laser, electron beam, plasma arc, or gas metal arc. Electron beam processes are conducted in a vacuum or low-pressure inert gas environment, allowing the use of reactive metals. In contrast, some heat sources require the parts to be shielded using an inert gas [19]. Certain AM processes, known as indirect metal AM processes, can consolidate metallic materials in the form of thin sheets and ribbons using ultrasonic methods without melting the feedstock material. Additionally, Alloy powders can be fused by jetting a binder onto a powder bed and then sintering it in a high-temperature furnace [10].

2.1.1. DED

DED is becoming increasingly popular since its mechanical properties are comparable to typical manufacturing techniques. DED is an AM method that uses concentrated thermal energy to liquefy and place materials, forming solid three-dimensional (3D) structures layer-on-layer [39]. This AM method is faster and more cost-effective than subtractive manufacturing and can produce intricate parts with minimal material waste. Furthermore, DED exhibits exceptional efficacy when utilized for repair and remanufacturing purposes [40]. DED can be classified into two categories based on the feedstock used: wire feed DED and powder feed DED, as depicted in Fig. 2. In the powder feed system, the material undergoes melting during the deposition process, but in the wire feed system, a laser or arc is used to fuse the wire on the substrate. The energy source is concentrated in a particular location, where it deposits the feedstock onto the previous layer (or the substrate for the first layer) simultaneously. This procedure involves creating a molten pool by melting both the raw material and the preceding layer. The resulting deposition layer is formed as the substance cools down [41].

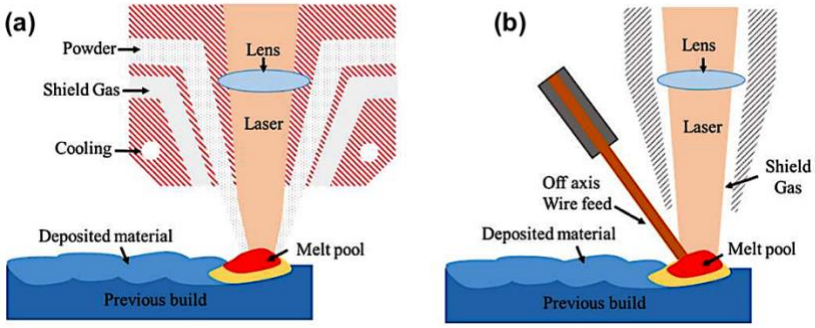

Fig. 2. Schematic illustration of DED systems[42]. (a) Powder feed DED system; (b) Wire feed DED system

In contrast to wire feed DED, powder feed DED provides better surface quality, although at a comparatively reduced production speed. Despite its considerable advantages over other metal AM technologies, DED still has limitations in achieving desirable surface finishes and minimizing porosity and cracks in the produced components [43]. Microstructural defects can arise from several reasons, including trapped gas, insufficient fusion, fast solidification, and inadequate powder melting[44]. A significant challenge in the DED process is the considerable variation in the quality of produced components. This variability is controlled by several aspects, such as process parameters, laser-material interactions, and defect creation. Although large-scale experimentation or simulation can enhance production quality, these approaches are considered time-consuming and expensive processes. In-situ monitoring is an alternative method for optimizing the quality of DED parts. However, this approach is highly challenging because of the enclosed chambers and the elevated temperatures of the melt pool, which can reach 2000-3000 °C [30]. Wire-based DED is a process similar to traditional welding that uses high power to create thick layers at high deposition rates, allowing for the economical production of large parts. However, parts produced using this technique usually require machining due to significant surface waviness caused by the formation of large molten pools [19].

2.1.2. PBF

PBF is widely recognized as the primary AM method due to its advanced ability to manufacture metallic and non-metallic components with remarkable precision. Moreover, PBF may produce homogenous alloy components with high strength and facilitate free-form manufacturing, therefore offering various advantages [45]. Compared to DED, which uses a laser, electron beam, or arc heat source is used to melt the feedstock, in PBF, thin layers of powder are added after melting the last one. However, PBF has some limitations in terms of bed or box size, making it impossible to produce large components [10,19,46]. L-PBF, as a subset of PBF, specifically employs laser technology for AM. The critical distinction between L-PBF and other AM techniques is the use of laser, which provides high precision and control during the process. This section investigates L-PBF and EB-PBF methods, as they have unique operational principles that significantly differentiate them. Solid components are formed from powdered material through heating, direct liquefaction, and subsequent solidification, particularly in L-PBF. Laser and electron beams are the primary heat sources to ensure high precision in producing these parts. The procedure proceeds by overlaying the preceding layer

with the subsequent layer of powder from a pre-deposited powder mixture using a re-coater blade or roller (Fig. 3)

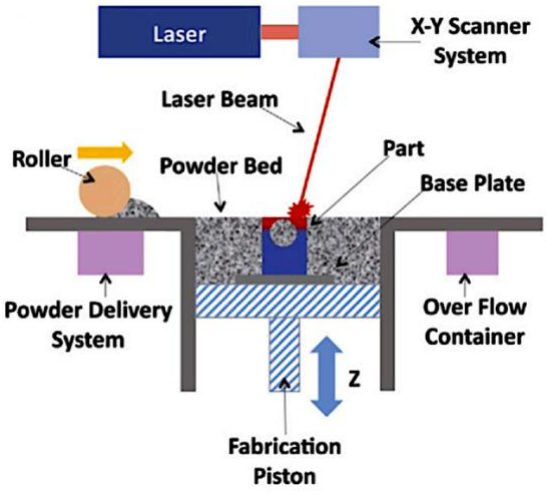

Fig. 3. Schematic of the L-PBF process [44]

The unmelted particles in the powder bed act as structural supports for the produced components. Following the melting and solidification of a layer of powder, the build platform descends, allowing a new layer to be spread and melted on top of the preceding one. Thermal rates in L-PBF can range from 10^3 to 10 (K/s) [47]. This method is very efficient for producing complex geometries using various materials while requiring support structures. Regarding large-scale production of gradient-structured metals and alloys, L-PBF is a highly effective technique for fabricating gradient structures characterized by intricate architectures. Nevertheless, there are still obstacles to overcome, such as a low level of densification in some conditions during the process and the inclination for gradient structures to exhibit considerably greater grain sizes, frequently surpassing 100 nm. To address these challenges, optimizing parameters such as power density, powder flow rate, scanning speed, and hatch spacing for each alloy is essential [48].

The main obstacle in employing metallic powders in L-PBF is identifying the appropriate process parameter map to manufacture components with exceptional microstructural and mechanical qualities. Therefore, some research has concentrated on optimizing LPBF process parameters. These investigations can be classified into three primary groups: laser-related, powder-related, and powder-bed-related characteristics [49].

2.1.2.1. Powder-related parameters

In AM, powder-related factors such as chemical composition, surface morphology, and particle size distribution are assumed to be relatively constant [50]. The chemical makeup of the powder is essential in determining the L-PBF process and its related parameters. The results suggest that minimal alterations in the chemical composition have little effect on the densification behavior. However, the powder's chemical makeup impacts its microstructure, subsequently affecting its mechanical characteristics. Kempen et al. [50] discovered that augmenting the

silicon (Si) concentration in the AlSi10Mg alloy leads to improved laser energy absorption in the powder bed, enhancing overall processability. It was shown that the shape of the starting powder significantly affects the ultimate quality and density of parts produced by LPBF processing. They found that powder morphology is a determining factor in the degree of compactness of powder particles when a new layer is deposited on top of an existing metal layer. In their study, the dimensions and morphology of the powder particles were also determined. As a result, it was reported that the dimensions and morphology of the powder particles are completely different based on the production method. Chang et al. [50] examined how particle size affects the microstructural characteristics, constitutional phases, and mechanical qualities of parts produced by LPBF processing. Their findings demonstrated that decreasing the size of powder particles enhances the uniformity of the microstructure of the resulting product. Erika Lannunziata Chang et al. [51] focused on investigating the impact of the powder atomization method on the densification, roughness, and mechanical characteristics of AISI 316L samples manufactured using the L-PBF technique. It was illustrated that gas-atomized samples generally exhibited higher density due to their decreased oxygen concentration and enhanced flowability.

2.1.2.2. Laser-related parameters

The dimensions of the laser system, including its type, spot size, and laser power, as well as scanning parameters such as scanning strategy, speed, and hatch spacing, greatly influence the properties of the manufactured component [50]. These parameters significantly impact the characteristics and excellence of components produced by L-PBF and are essential for defining the volumetric energy density. The term "volumetric energy density" denotes the extent to which a unit volume of powder absorbs energy during the melting process. Enhancing the laser volumetric energy density can optimize the density of manufactured components, even when subjected to different atmospheres like argon, nitrogen, or helium, as illustrated in Fig. 4. In the case of Al–12Si components, there exists a critical energy level of 30 J/mm³, below which the energy is inadequate to completely liquefy the powder, resulting in reduced density and heightened porosity [50]. Moreover, exceeding this critical volumetric energy density, 30 J/mm^3, may negatively impact the surface quality due to the development of balling [47].

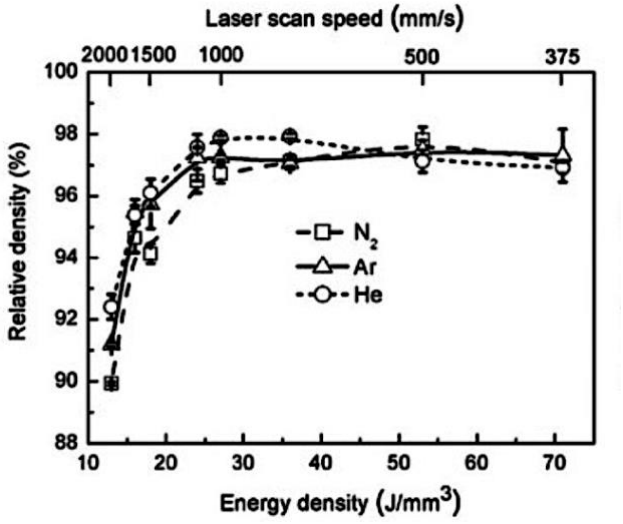

Fig. 4. Analysis of the relationship between relative density and incident laser energy for Al–12Si components treated using LPBF. The result evidences a positive correlation between laser energy density and relative density. At energy densities below 30 J/mm³, the energy is insufficient to completely melt the powder, leading to a reduced relative density. Once this threshold is surpassed, the relative density stabilizes at [47].

Residual stresses and deformation in LPBF-built parts, can be considered as the main challenges in this technology. During the L-PBF process, localized heat generates significant temperature gradients, resulting in stress inside the manufactured components. Plastic deformation happens when the thermomechanical stress exceeds the yield strength of the material. Repetitive thermal cycles from consecutive layers can lead to the buildup of stress and deformation, which may ultimately lead to failure and significant distortion of the LPBF components, including cracking and layer delamination. As a result of its impact on local heat distribution, the scanning technique significantly affects these deformations and residual stresses [47].

Using small-diameter beams and small metal powders, complex parts with fine and closely spaced features can be produced. These processes differ in their heat source power, scanning speed, deposition rate, surface roughness, and other essential features, as depicted in Fig. 5 [10].

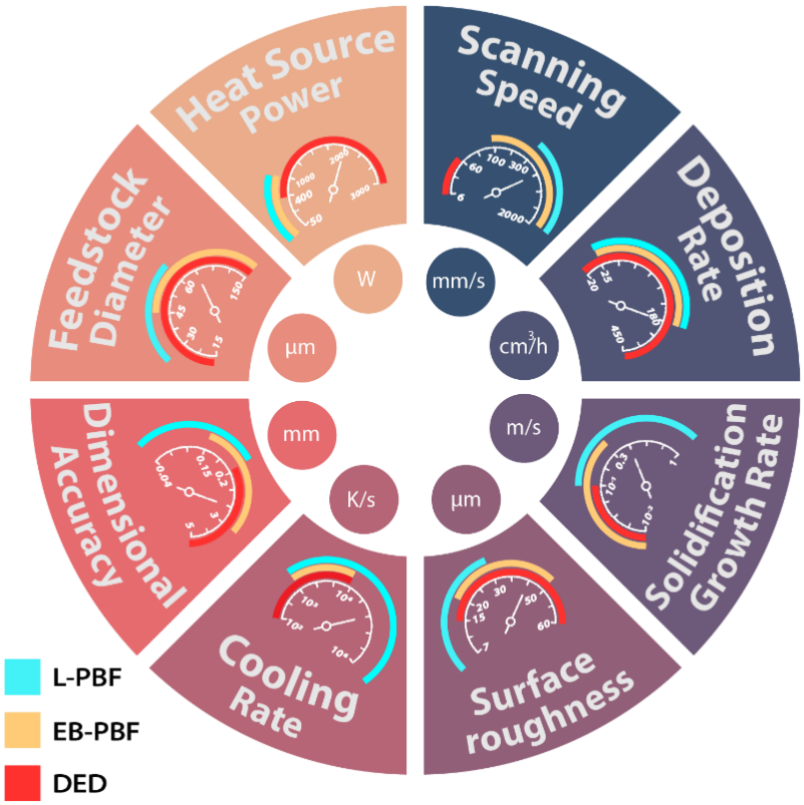

Fig. 5. Process parameters for various AM methods upon consulting Refs [10,19,34,52–57]. The surface roughness represents the average deviation of the surface from its mean height.

These parameter differences can cause a 10,000-fold variation in cooling rates and significant differences in temperature gradient and heat input among various AM methods. As a result, the microstructure and properties of components are affected by the cooling rate and heat input, which is why the parameters shown in Fig. 5 must be controlled with more effective approaches than in conventional processes to ensure the production of high-quality and dependable parts [45,58–61].

Achieving precise control over the microstructure, defects, and properties in AM processes is still a challenge due to the need for extensive experimentation to explore a wide range of process parameters. Printing conditions are often selected based on the machine manufacturer's recommendations or through trial and error [62]. Trial and error methods are not ideal for improving part quality in AM due to the expensive nature of the feedstock and machines [52], as well as the fast-evolving economic culture that leads to the creation of new products at a rapid rate. Instead, mechanistic models can predict various physical attributes of AM parts, such as temperature fields, solidification characteristics, microstructure, and defect formation. These models rely on a phenomenological understanding of the process variables and thermophysical properties of alloys [63].

2.1.3. Artificial Intelligence integrated with AM

The use of AI methods in digital manufacturing is becoming increasingly prevalent due to advancement in data acquisition technologies, robotic systems, and computer science [64].

These methods, including ML, automation, robotics, machine vision, data mining, big data analytics, and expert systems, have all demonstrated their effectiveness in enhancing control over systems and product quality [20]. ML can assist in various stages of the AM process by analyzing data on process variables, alloy properties, and product attributes. This analysis can help reduce defects, achieve superior microstructures and properties, and accelerate product qualification. Additionally, using ML and developing mechanistic models can create opportunities for producing novel alloys [52]. The combined use of mechanistic models and ML is crucial for various aspects of AM, including designing, planning, producing, characterizing, and evaluating the performance of printed parts (see Fig. 6).

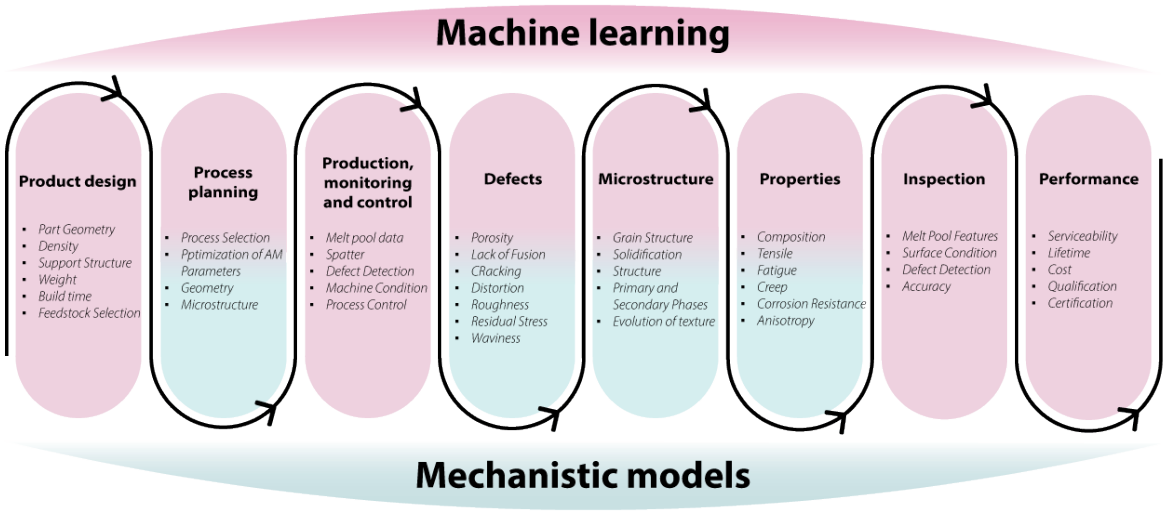

Fig. 6. Application of mechanistic models and ML in the various steps of metal AM. Both mechanistic models and ML offer a quantitative framework for understanding the characteristics of components. This figure illustrates the respective roles of ML and mechanistic models at different stages in manufacturing and analyzing elements.

The integration of ML with AM processes presents an opportunity to effectively address defects during the early stages and stop the production of defective components as soon as a defect is detected. ML can optimize input and output characteristics and predict the properties of a component, while also enhancing AM process speed, accuracy, and efficiency, ultimately influencing quality outcomes [23,65].

2.2. Machine Learning

ML methods have gained considerable interest due to their exceptional performance in various data-related tasks, including regression, classification, and clustering. As seen in Fig. 7, these approaches can be classified into supervised, unsupervised, semi-supervised, and reinforcement learning, based on the extent and nature of supervision required during the training process [24]. Supervised learning involves labeled data that is divided into training and testing sets. The primary objective is to develop models that establish links between predictors (features) and the response (target) within the dataset [66]. In contrast, unsupervised learning does not require labeled data or a training set to create the model. In the case of semi-supervised learning, a small portion of the dataset is labeled, enabling the system to learn from

these labeled samples and classify a larger volume of data. Reinforcement learning differs from other ML methodologies by using a reward-and-penalty framework for algorithm training [33].

Fig. 7. Three different approaches for the classification of ML.

ML models can also be classified as batch/offline learning or online learning. In the case of offline learning, the model cannot learn incrementally and must be trained using all available data, which demands substantial time and computing resources. Online learning enables the model to learn dynamically, and incrementally as new data is presented without the need to retrain the entire model. This methodology is particularly appropriate for working with large and continuously expanding datasets [24]. Likewise, ML approaches can be categorized as instance-based or model-based learning. Instance-based models use a similarity measure to identify new cases, while model-based learning involves constructing and using a model for predictions. In the field of AM, ML approaches are typically offline instance-based or model-

based, incorporating supervised or unsupervised learning models [24]. As depicted in Fig. 8, each method in ML uses multiple algorithms, which are elucidated in the accompanying table.

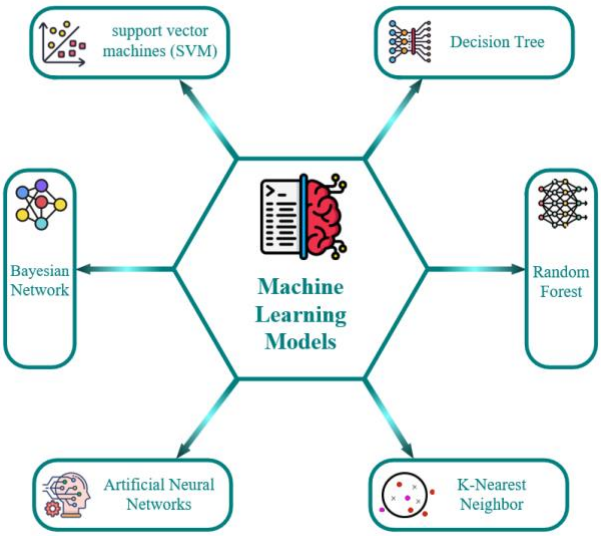

Model	Description
	Used for classification and regression, the model can split data into groups based on their locations in feature space; the features of the data fully determine their locations and there is no stochastic element involved.
	Progressively classifies a group of variables based on rules and displays them as an upside-down tree; the root of the tree often displays the most important variable, and the apex shows the least important variable
	Consists of multiple decision trees, each with a classification; the forest gets a classification from the attributes of the greatest number of trees; for regression, the model considers the average of the outputs of different trees
	Separates data into different classes based on the attributes or the class of the majority of the nearest neighbours; the number of nearest neighbours, k, is selected by trial and error
	Layers of hidden nodes connect input and output variables; an activation function is used to connect nodes with each other; errors in predictions are minimized by adjusting weights for each connection.
	A statistical model that represents the probabilistic relation between cause and effect; the conditional probabilities are computed using Bayes' theorem

Fig. 8. Some of the most essential ML algorithms with their description.

2.2.1. Supervised Learning

Supervised learning is the most frequently employed method among machine learning techniques [67]. In this method, a model can be developed by training the dataset to accurately classify labeled data within the test set [68]. However, acquiring labeled data for training supervised learning models can be challenging and costly, especially for large datasets. Additionally, the manual labeling process is susceptible to human bias, which can further degrade the accuracy of the model [24]. Supervised ML is divided into two main categories: classification and regression methods. Classification methods contain SVMs, DTs, Naïve Bayes, k-NNs, and ANNs. These methods rely on the "pattern recognition" principle to categorize data. Conversely, regression involves predicting continuous values by analyzing a dependent variable concerning one or multiple independent variables. This procedure provides

the optimal pattern that best fits the given data [69]. In supervised learning, the ML model adjusts the weights assigned to input variables iteratively until it achieves an optimal data fit. This process involves an algorithm that identifies patterns within a training dataset. As shown in Fig. 9, some specific considerations and preliminary measures must be undertaken to execute this task [67,70]:

1. Acquiring a dataset and data processing
2. Feature selection (target variable)
3. Splitting the dataset (training, cross-validation, testing)
4. Hyperparameter tuning and prediction

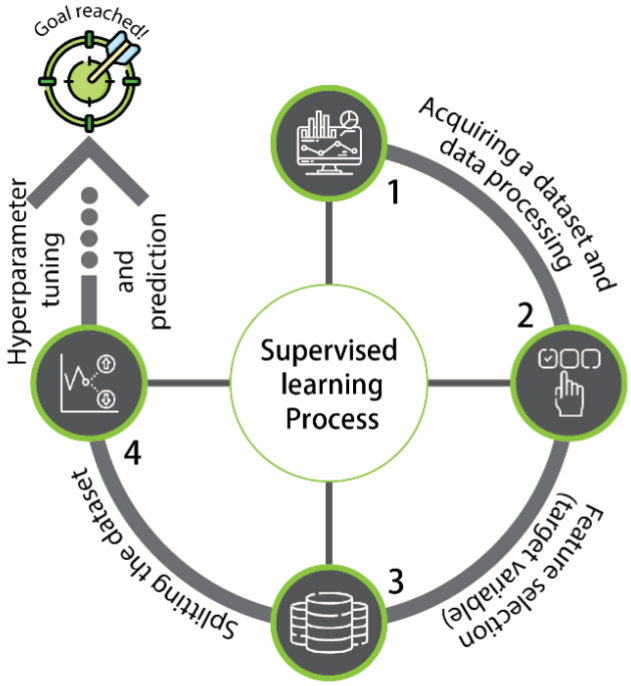

Fig. 9. The steps required for developing ML models based on supervised learning algorithms.

Supervised learning algorithms can address various numerical engineering problems. Each input data point is associated with a corresponding output variable Y, and the training dataset comprises multiple input-output pairs [71]:

$$\boldsymbol{Y} = \begin{bmatrix} \boldsymbol{y_1} \\ \boldsymbol{y_2} \\ \vdots \\ \boldsymbol{y_n} \end{bmatrix} \tag{1}$$

Meanwhile, various mathematical techniques can be employed to represent scalar values in the context of observations. These observations are typically organized in rows, with each column representing a specific feature. This arrangement of statements leads to the formation of a matrix structure [72]:

$$\boldsymbol{X} = \begin{bmatrix} \boldsymbol{x_{1,1}} & \boldsymbol{x_{1,2}} & \cdots & \boldsymbol{x_{1,n}} \\ \boldsymbol{x_{2,1}} & \boldsymbol{x_{2,2}} & \ldots & \boldsymbol{x_{2,n}} \\ \vdots & \vdots & \ddots & \vdots \\ \boldsymbol{x_{n,1}} & \boldsymbol{x_{n,2}} & \cdots & \boldsymbol{x_{n,n}} \end{bmatrix} \quad (2)$$

In this method, datasets can take various forms, including photos, audio samples, and text. The error between the predicted and actual output values is calculated using an objective function known as the cost function. To provide an unbiased assessment of the model's accuracy, a trial phase is conducted using a test set consisting of previously unseen additional information [71].

2.2.1.1. Regression Learning for AM Applications

Regression analysis is a valuable tool for predicting and optimizing various process parameters for AM applications. Several studies have explored the applications of this technology, providing valuable insights into how it can enhance manufacturing processes and product quality. For instance, Eshkabilov et al. [73] implemented an SVR algorithm to establish the relationship between process parameters and the relative density, hardness, yield strength, and tensile strength of samples produced by L-PBF. Similarly, a RFR model was developed by Peng et al. [74] to determine the correlation between the fatigue behavior of AlSi10Mg alloy and the defects of parts manufactured by L-PBF. In another work, Caiazzo et al. [75] applied an NN model to correlate laser power, scan speed, and powder feeding rate with geometrical parameters of the deposited track, highlighting the significant impact of regression analysis in optimizing AM processes.

2.2.1.2. Classification Learning for AM Applications

Classification analysis has also proven to be a valuable tool in various fields of AM for categorizing and optimizing diverse process parameters through different algorithms. Khanzadeh et al. [76] used multiple ML algorithms, including KNN, SVM, DT, and DA, to detect defects. Fig. 10 illustrates a procedure that uses images as input for defect detection in the L-PBF process of Ti-6Al-4V. For each thermal image labeled as porous or non-porous, geometric features are extracted and used to train the ML models.

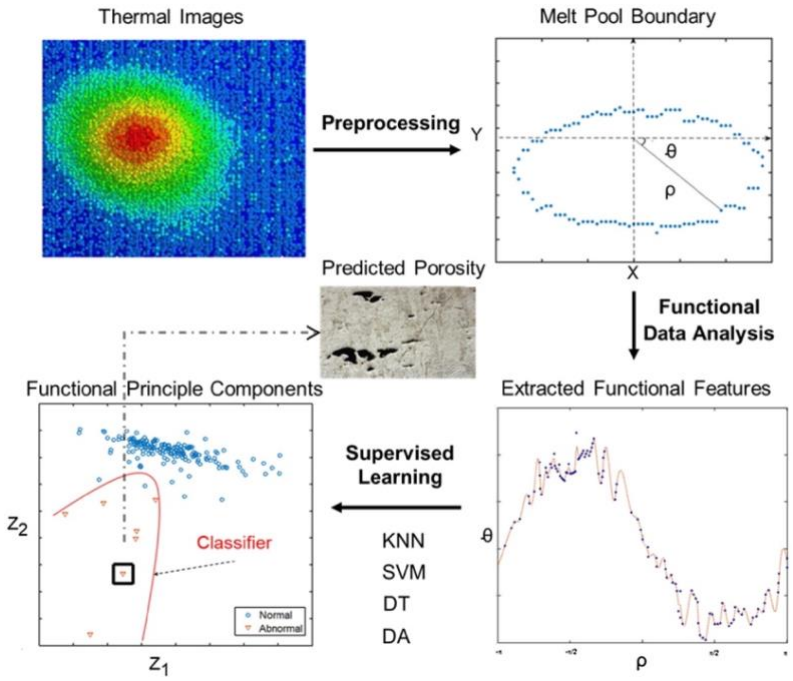

Fig. 10. Illustration of the process for predicting porosity through supervised ML [76].

SVM is another well-known ML tool that efficiently handles classification and regression tasks. This algorithm has garnered significant attention from researchers, especially in defect detection. The SVM algorithm relies on hinge loss for its operation. The exponential loss is associated with the classic boosting method, while the logistic loss function is linked to logistic regression. The logistic loss function is significant as it serves classification purposes and is prominent in ML problems [77,78]. The mathematical expression for logistic regression is articulated as follows:

$$\text{Log Loss} = \sum_{(x,y)\in D} -y\log(\acute{y}) - (1-y)\log(1-\acute{y}) \qquad (3)$$

In the context of logistic regression, the dataset $(x, y) \in D$ consists of a significant amount of data with various labels. In this classification task, the variable y denotes the chosen label applied to a particular instance. It is essential to acknowledge that logistic regression commonly deals with binary classification, wherein the dependent variable y assumes either 1 or 0 values. However, the variable (y') represents the estimated value, which falls within the continuous range of 0 to 1 [79].

In classification problems, NNs stand out as one of the most widely adopted algorithms. Traditional NNs are typically employed when dealing with inputs consisting of parameters and class labels. However, for tasks involving images, handwritten digits (see Fig. 11), and autoencoders, a specialized form of NN algorithm known as CNN is specifically designed to provide practical solutions [80]. This model initially dissects image characteristics such as curves, edges, and lines in the early layers. Subsequent layers then organize and synthesize these features, while the final layers are responsible for reconstructing the image from scratch

[80,81]. In another task, Yuan et al. [27] investigated the application of CNN to predict the continuity of L-PBF tracks. The ML model was fed with melt pool images captured at various printing positions. Variances in melt track width resulted from adjustments to L-PBF process parameters. The algorithm primary task for each track was to evaluate the mean and standard deviation of track width and achieve a 93% precision rate in classifying track continuity.

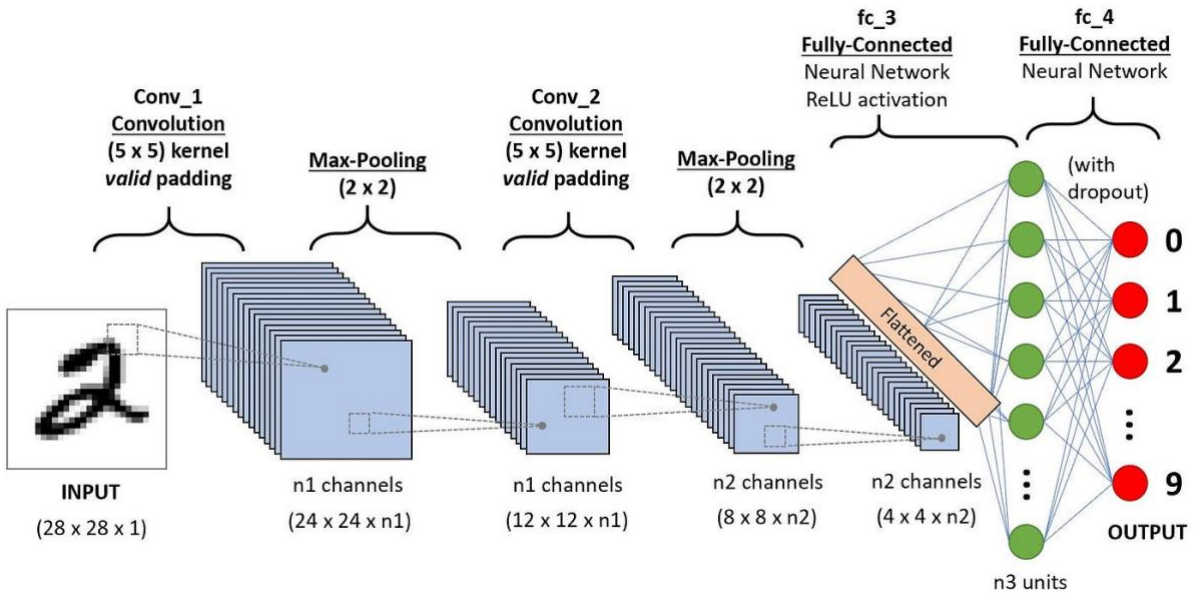

Fig. 11. Schematic of CNN algorithm for classifying handwriting digits [67,82].

2.2.2. Unsupervised Learning

Unsupervised learning is a ML method that aims to identify previously unknown patterns within a dataset without predefined targets or labels. Unlike supervised learning, which relies on labeled training data, unsupervised learning, also known as self-organization, can construct probability density models using input data with minimal human supervision [83]. Unsupervised learning is employed to explore algorithmic approaches that can effectively organize complicated inputs and detect elemental patterns with limited human guidance to create improved predictive systems [69]. For instance, UTL has been used as a promising approach for anomaly detection in industrial applications. It is a specific type of unsupervised ML that can train abnormal detectors adapted to changing operating situations [84]. Additionally, unsupervised learning models are typically less accurate than supervised learning models, and the user should still explain the results of the algorithm [24]. There are five main categories for unsupervised learning: outlier detection, data clustering, dimensionality reduction, hierarchical learning, and latent variable models [69]. The primary task in unsupervised learning involves analyzing data clusters formed based on their similarity. However, in AM, dataset sizes are often limited, restricting the application of the clustering analysis [25]. Wang et al. [26] used conventional optical images as input data for the autoencoder in an AM process. They implemented a clustering algorithm to identify the data group that yielded optimal results. The subsequent evaluation using a scoring system showed that the ML-based clustering method aligned effectively with conventional parameter optimization techniques, such as laser point distance, powder layer thickness, and laser

scanning speed. Furthermore, an unsupervised ML model inherently possesses the ability to differentiate extraneous inputs within models and develop strategies to ensure uniform material production under consistent conditions and quality benchmarks [67]. Likewise, unsupervised learning is useful for identifying cyber-physical attacks in AM processes [85].

2.2.2.1. K-means Clustering

The K-means clustering algorithm is a widely used unsupervised learning method for clustering challenges due to its simplicity and effectiveness. The algorithm involves setting up k centers that are assigned to a particular cluster [86]. While k-means operates as an unsupervised technique, selecting the number of clusters requires careful consideration to minimize the probability of generating inaccurate results. Furthermore, k-means encounter challenges when dealing with non-spherically dense data clusters [87]. Snell et al. [88] introduced a pore classification methodology that relied on k-means clustering for distinguishing gas pores, keyholes, and lack of fusion for L-PBF specimens. In that study, XCT was employed to gather 3D pore data from L-PBF Ti-6Al-4V specimens. The CT-obtained radiographs were used to reconstruct 3D volumes with specific voxel sizes. The datasets were processed, segmented, and quantified using image processing methods, where the length, sphericity, and aspect ratio were employed as parameters for clustering 2664 pores. Optical Microscopy was applied to gather 2D pore data from 81 L-PBF Inconel 718 specimens through micrographs, utilizing the roundness and length measurements from a total of 21,955 pores as inputs for k-means clustering. Optical microscopy is a quick and cost-effective method for collecting data across numerous samples, making it an ideal choice for optimizing metal AM parameters. The results, partially illustrated in Fig. 12, indicate that the clustering of 3D pore data is more effective than the traditional limits-based approaches in classifying the pore types [88].

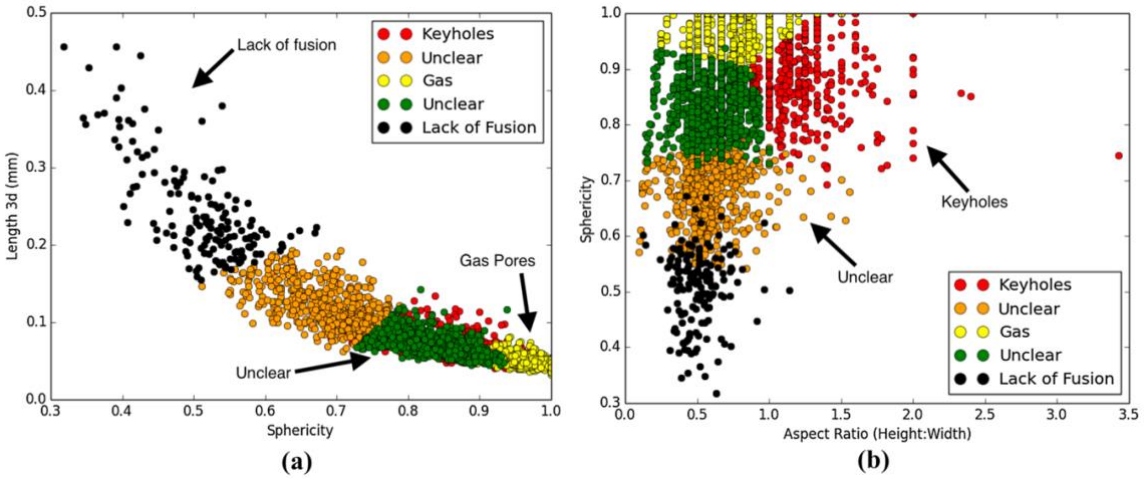

Fig. 12. Pore classification based on k-means clustering for L-PBF Ti-6Al-4V specimens. (a) pore length and sphericity. (b) Sphericity and vertical aspect ratio [88].

2.2.3. Semi-Supervised Learning

Semi-supervised models are used to overcome the limitations of both supervised and unsupervised ML models [89]. Semi-supervised learning is an ML approach that combines labeled and unlabeled data to train a model. By integrating the advantages of both methodologies, semi-supervised models can achieve higher levels of accuracy and

interpretability compared to supervised and unsupervised learning methods. Semi-supervised models can also be used to learn from unlabeled data, which is valuable when labeled data is scarce [90].

Labeled data from supervised learning methods can be used to initialize a model for unlabeled inputs, which may or may not have been previously labeled. Semi-supervised learning methods can be divided into two categories: transactive graph-based methods and inductive methods. Inductive methods use three subcategories to define how they use unlabeled data: Wrapper methods, unsupervised processing methods, and semi-supervised methods. Wrapper methods, such as self-training, co-training, and boosting, use unlabeled data to improve the performance of a supervised learning model. Unsupervised processing methods, such as feature extraction, cluster-then-label, and pre-training, use unlabeled data to extract features or learn a representation of the data that can be used to improve the performance of a supervised learning model. Semi-supervised methods, such as maximum-margin, perturbation-based, manifolds, and generative models, use unlabeled data to learn a model that is resistant to noise and outliers [91].

Although semi-supervised ML models have great practical value, they have been used less frequently in the AM field than in other fields. Okaro et al. [90] developed a Gaussian Process model to automatically detect defects in AM products. They used a large photodiode dataset to extract key features and set up a monitoring system that included both in-situ and ex-situ labeling methods. The ex-situ data was labeled using ultimate tensile strength tests. A receiver operating characteristic (ROC) curve was calculated as the classification algorithm provides the probability of each data point association with a specific class. The analysis entailed evaluating the effectiveness of the classification algorithm by varying the 'threshold probability.' The semi-supervised model developed in the study was found to capture the benchmark results more closely than the supervised approach, as shown in Fig. 13.

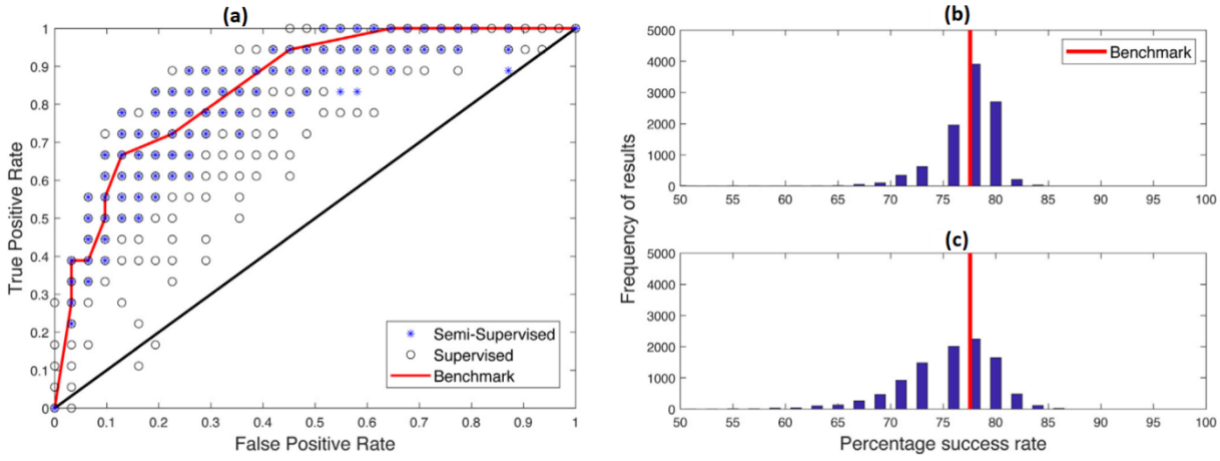

Fig. 13. The ROC curve of the ML models, along with the histogram of algorithm success rates for the (b) semi-supervised and (c) supervised [90].

2.2.4. Reinforcement Learning

Reinforcement learning is defined as "the process of acquiring a mapping from a given situation to corresponding actions to maximize a scalar reward or reinforcement signal" [92]. When the primary goal is to generate a prediction-based system, reinforcement learning is the best approach compared to other ML methods. The most crucial characteristic of this approach is its ability to acquire ways to lead to desired results using encouragement. The rewards motivate the learning process and influence the behavior of the algorithm [93,94]. This approach is occasionally referred to as the "environment-centric approach", which is an effective technique for enhancing automation and refining the efficiency of complex systems [95].

Wasmer et al. [96] established a quality monitoring system for L-PBF by incorporating reinforcement learning with acoustic data acquired from acoustic emission during printing. Their evaluation of classification accuracy for AISI 316L samples indicated the potential of their reinforcement learning-based approach for in-situ, real-time quality monitoring within L-PBF. In another study, Knaak et al. [97] introduced the application of reinforcement learning for predicting surface roughness in the L-PBF process, illustrated in Fig. 14. They implemented an advanced optical imaging system with an extended dynamic range combined with convolutional neural networks. The main benefit of this approach is its capacity to be incorporated into a control system for real-time surface optimization [97].

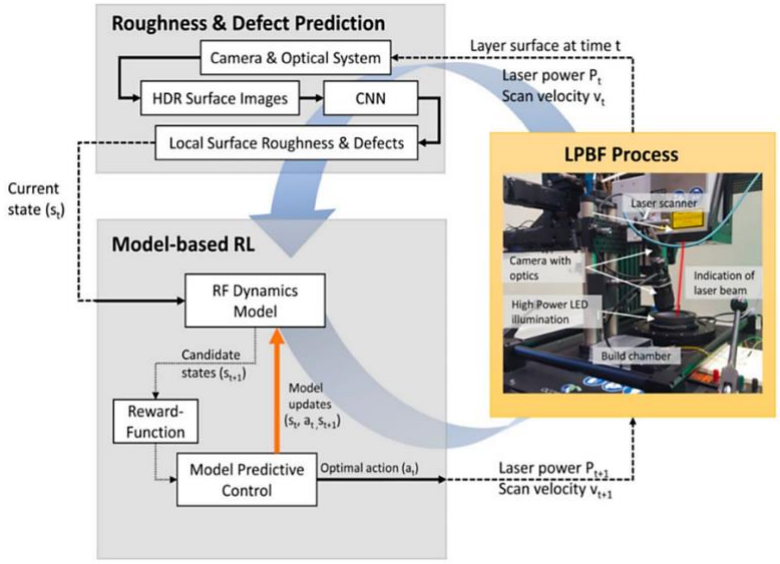

Fig. 14. Layer-wise Monitoring and Optimization Framework for L-PBF Processes Based on Reinforcement Learning Models[97].

2.3. Application of Machine Learning in Additive Manufacturing

The interplay between process-structure-property relationships has been thoroughly examined and documented in multiple review articles [25,50,98,99]. The processing phase in the commonly used process-structure-property relationships has two distinct components: "processing parameters" and "processing resultant data". This division aims to differentiate between data existing before the manufacturing process and data created during the process [100]. These data types are employed for ML purposes in various AM aspects, including

processing parameters optimization and property prediction, cost estimation, geometric deviation control, defect detection, and in-situ monitoring [25]. In the subsequent sections, each of these applications and their associated relationships will be explored.

Table 2 lists recent literature on metal AM that applies data-driven approaches, categorized based on the data acquisition method. This classification allows readers to become familiar with potential data sources, their applicability, and the features that can be detected or predicted by applying them. It can be seen in the table that the in-situ monitoring techniques, such as optical, thermal, X-ray imaging, and acoustic methods, are the most utilized data acquisition techniques. The techniques mentioned are used to observe general anomalies during the process [101] or specific phenomena like the detection of plume and spatter phenomena [102] and keyhole porosity [103,104]. This finding highlights the need for standardized protocols and robust quality assurance systems, including a closed-loop control system that comprehensively monitors and dynamically executes real-time modifications to the end product. This approach has the potential to broaden the application domain for AM methods. For this purpose, researchers have utilized statistical techniques to examine different forms of in-situ data acquisition to identify process signatures and process windows. The analyzed data has been utilized to develop ML models to predict or identify the desired features.

Table 2. Literature on metal AM works applying data-driven approaches

Data acquisition method	AM technology	Data source	Alloy	Application	References
In-situ monitoring	L-PBF	High-speed thermal imaging	17-4 PH stainless steel [101], 304L stainless steel [105]	Anomaly quality prediction [101], detection of micropores [105]	–
		High-speed optical imaging	316L stainless steel	Prediction of plume and spatter phenomena [102], identification of local defects related to overheating [106]	–
		Synchrotron X-ray imaging	Ti6Al4V [103,104], AlSi10Mg, Inconel 625, CP1, 316L stainless steel, Aluminium [104]	Keyhole porosity detection [103,104]	–
		Optical tomography image	AlSi10Mg	Detection of local hot spots	[107]
		Thermographic imaging	H13 tool steel	Detection of geometrical shape, delamination, and splatter	[108]
		Acoustic signal	Ti6Al4V, CM247- LC [109], 304L Stainless steel [110]	Prediction of porosity and surface imperfections [109], single track defects [110]	–
		High-resolution sensor imagery	GP-1 stainless steel	Detection of discontinuities, such as incomplete fusion, porosity, cracks, or inclusions	[111]

Data acquisition method	AM technology	Data source	Alloy	Application	References
		Optical imaging	17–4 PH stainless steel [86,112], Ti6Al4V [86,113–116], 316L stainless steel [27,86,117], bronze alloy [86]	Defect prediction [112], prediction of porosity [114,116], powder bed anomalies [113], detection of single track width and continuity [27,117], identification of edge smoothness [115], process anomaly detection [86]	–
		Photodiode	Inconel 718 [118,119], AlSi10Mg [105]	Porosity detection [119], Fault detection, quality classification [118], detection of overhang defects [105]	–
	L-DED	Pyrometry	Ti6Al4V	layer-wise quality prediction [120], Porosity [121],	–
		Synchrotron X-ray imaging	Inconel 718	Prediction of track height, roughness, and melt pool geometry	[104]
		Acoustic signal	A mixture of Ti6Al4V with H13 tool steel	Detection of porosity and crack	[122]
		Melt pool thermal image	Ti6Al4V [76,121,123,124] [125], Sponge Ti powder [126], 316L stainless steel [127]	Porosity prediction [76,121,123,124,126], dilution estimation [127], surface distortion prediction [125]	–
		Point cloud processing	316L stainless steel	Identification of surface defects	[128]
Post-process characterization	L-PBF	High-speed camera	316L stainless steel	Determination of build quality	[129]
		Archimedes test	17-4 PH stainless steel [130], AlSi10Mg [131]	Prediction of porosity	[130,131]
		XCT experiment, 2D micrograph	Ti6Al4V [88,132], Inconel 718, Ti5553, Haynes 282 [88]	Identification of different pores [88,132]	
		Archimedes test, and surface roughness	Stainless steel 316L-Cu	Predicting part density and surface roughness in multi-material region	[16]
		Optical micrograph, first-principles calculations, and compression tests	TiZrNbTa RHEA	Prediction of defects during in-situ alloying	[132]
		Optical micrograph	316 L stainless steel, AlSi10Mg, Fe60Co15Ni15Cr10 MEA	Prediction of porosity	[133]

Data acquisition method	AM technology	Data source	Alloy	Application	References
	L-DED	Optical micrograph	Al-5083 [134], 316L stainless steel [135], ER70S-6 mild steel [136], 1.5130 [137], Ti-10Fe [132]	Macro and micropores analysis [134], track depositing height [135], track geometry prediction [136], prediction of welding distortion [137], build height and grain size [132]	–
		Fatigue and XCT experiments	Ti6Al4V	Fatigue life prediction	[138]

2.3.1. Processing Parameters Optimization and Property Prediction

Ensuring part quality with specific processing parameters can be costly and time-consuming for designers. More specifically, the biggest challenge in the L-PBF process is the determination of the optimal process parameters that will results in a high-density and well-processes component. While experiments and simulations are helpful, they may not always be practical in cases with various input parameters. However, ML models efficiently establish the link between the process parameters and part quality, reducing costs and speeding up the optimization process [139]. Process parameter optimization is usually carried out when either innovative materials or a new approach needs to be processed by AM methods [140]. Process parameters can also be set as input features in ML methods to optimize the geometric variations for L-PBF components [21]. Several instances exist in the literature [141–145] where researchers have utilized various ML models and algorithms for optimizing process parameters. Among the ML models, ANNs have demonstrated superior efficacy for process parameter optimization [146]. Reddy et al. [97] developed an ANN model to predict the volume fraction of α phase for various Ti alloys produced via the DED method followed by different heat treatments. The ANN model used in this study had two hidden layers, each consisting of six neurons representing Al, V, Fe, O, N, and heat treatment temperature for the input layer, and two neurons representing α and β phase volume fractions for the output layer. The model was trained over 18,000 iterations with hyperparameters set at a learning rate of 0.7. The comparison between experimental and model prediction results can be observed in Fig. 15.

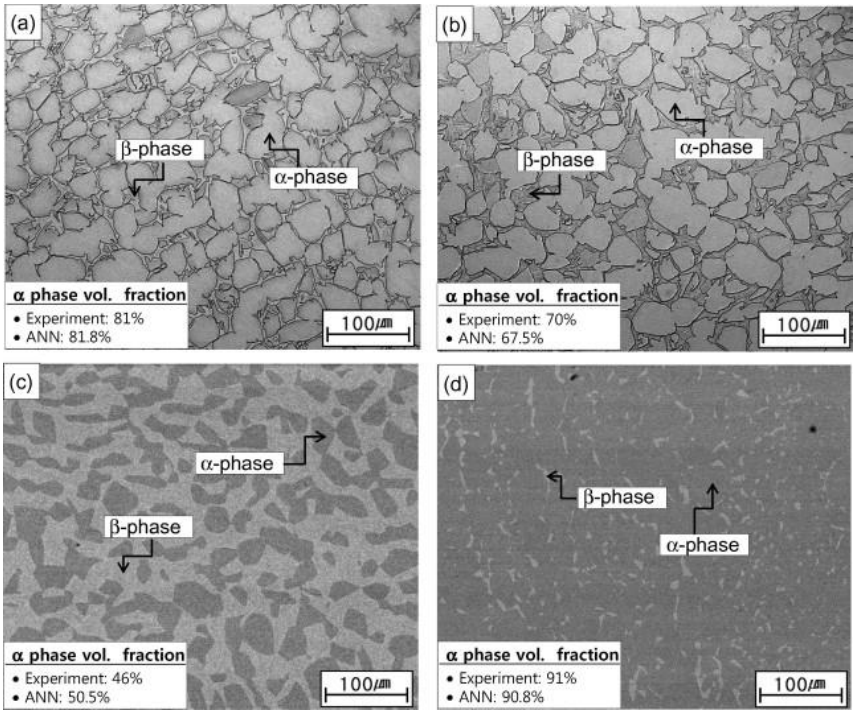

Fig. 15. Comparison between experimental data and ANN predictions for the quenching process of a Ti–6.3Al–4.1V–0.21Fe–0.17–0.005N alloy at four different temperatures: (a) 700 °C, (b) 815 °C, (c) 900 °C, and (d) for a Ti–6.85Al–1.6V–0.13Fe–0.17–0.001N alloy quenching[147].

Silbernagel et al. [148] used ML techniques to optimize process parameters for L-PBF of pure copper using optical imagery. Data in the form of images was gathered and subsequently fine-tuned through ML methodologies. In this case, as shown in Fig. 16, the results indicate that the most favourable track outcomes were achieved across all layer thickness variations using a point distance of 50 µm and laser scan speeds of 250 mm/s or higher.

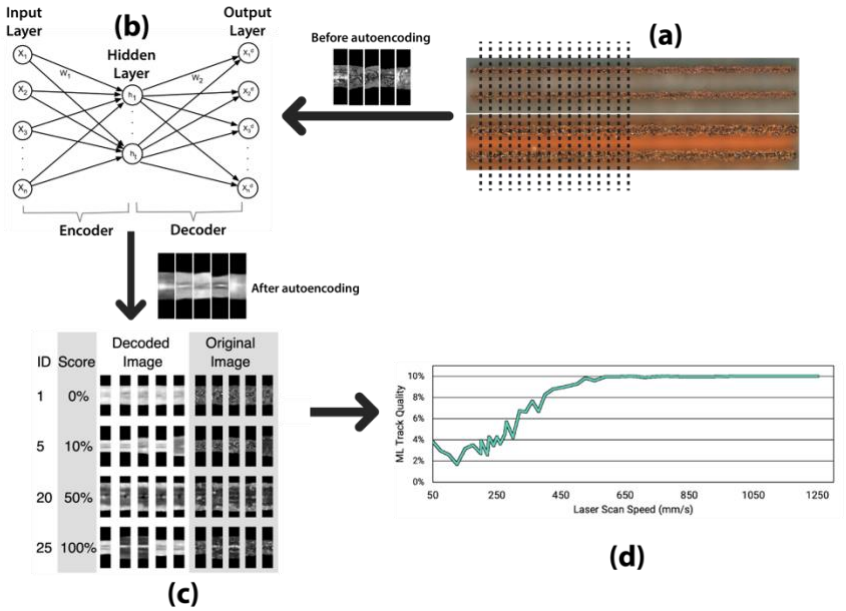

Fig. 16. The procedure of ML methodology adopted by Silbernagel et al. [148]. (a) Pairs of 18 mm long full scan track images of thin walls [148]. (b) Using the CNN algorithm with an AE [149] for decreasing the high-

dimensional image data into a simplified reconstructed output, (c) selection of the top 20 images from clusters which were evaluated and scored between 0 (clusters which showed signs of balling or an unstable melt pool) and 100 (clusters where the images demonstrated high-quality weld tracks), and (d) ML track quality for different laser scan speeds [148].

ML methods have also been used to predict the mechanical behaviour of AM products, including tensile properties [150–153], fatigue behaviour [154–157], and microhardness [158–161]. In a research by Maleki et al. [150], the process parameters were optimized, and the mechanical properties of Ti6Al4V were improved using a Neural Network model (see Fig. 17). The research indicated that scanning speed, laser power, and hatch spacing have the most notable effect on the tensile strength, as shown in Fig. 18.

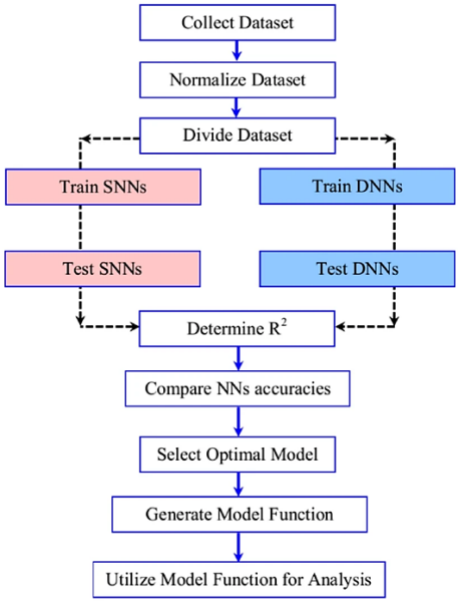

Fig. 17. The flowchart of the procedure of the research done by Maleki et al[150].

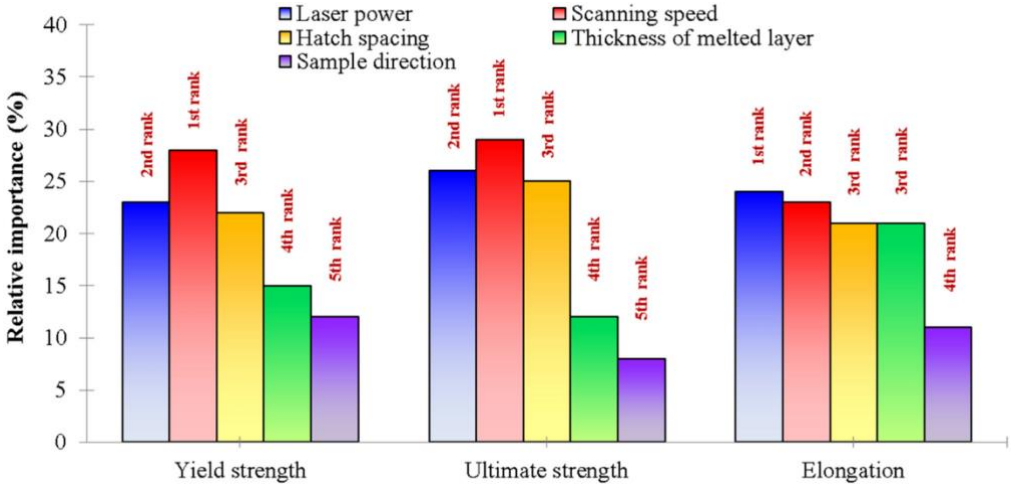

Fig. 18. Effects of the various tensile process parameters on the properties of L-PBF fabricated Ti-6Al-4V [150].

Moon et al. employed a drop-out neural network (DONN) [156] to predict the fatigue behavior of Ti–6Al–4V L-PBF-produced samples. The model features consisted of stress, surface

roughness (R_a, R_t, R_{iso}, $\bar{r}$), pore density, diameter, compactness, sphericity, and projected YZ area for 41, 35, and 76 data points, with the predicted target being log cycles to failure. Due to the limited amount of data, the leave-one-out cross-validation method was employed. One data point was reserved for testing, while the remaining data was used for training. This process was iterated through for all the data. Predictions and the experimental values can be observed in pair plots depicted in Fig. 19, where M and AB refer to two samples with different surface features.

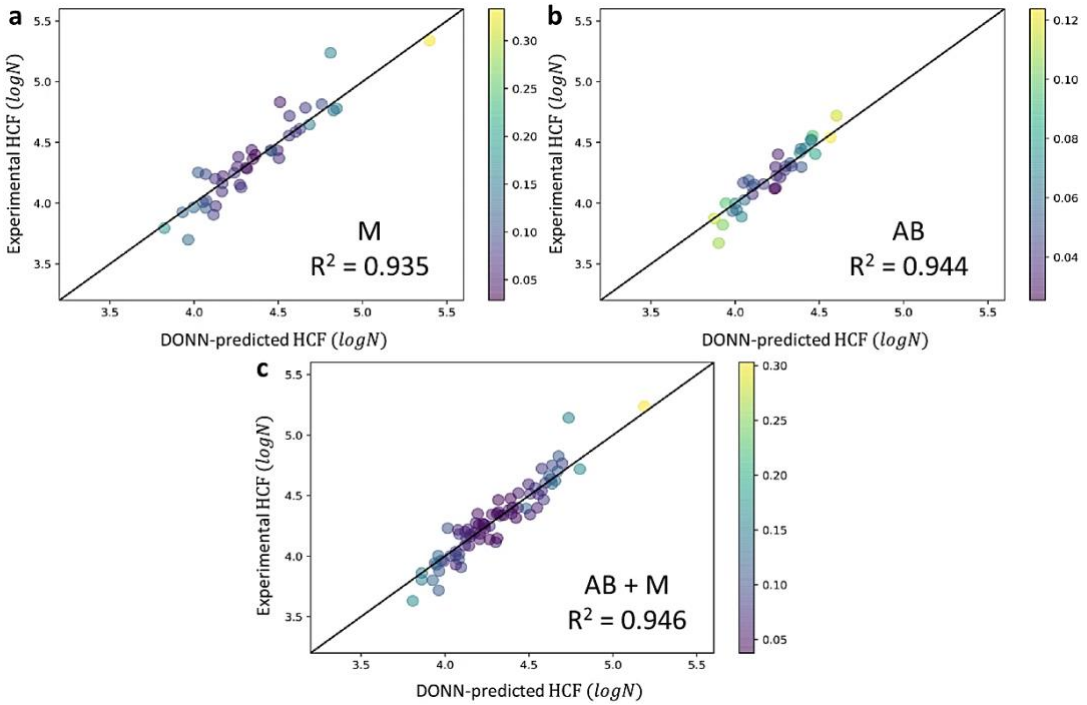

Fig. 19 Comparing DONN predictions with experimental high-cycle fatigue (HCF) in logN for (a) AB, (b) M, and (c) combined AB+M samples. The uncertainties are displayed in different colours [156].

The fatigue behavior of metallic materials is mainly influenced by their surface characteristics, such as roughness, porosity, and defects, thus necessitating their consideration in metal AM products for cyclic loading applications. Therefore, the surface quality of the metal AM components needs to be enhanced so the products are widely adopted in delicate applications like medical components. Zhang et al. [162] presented an ANN algorithm to model and interpolate the complex, nonlinear relationship between different parameters and the targeted surface roughness and porosity of L-PBF Ti-6Al-4V samples. The training dataset, which consists of 35 samples, was obtained from DEM simulations (refer to Fig. 20). This approach enabled the creation of a process map, which helped to determine the optimal process parameters to achieve the desired surface roughness with a prediction accuracy of over 97%. Consequently, this method led to time savings during the printing process and reductions in the overall manufacturing cost. Additionally, Kumar et al. [163] worked on predicting the surface roughness of components produced by DED using KNN modeling. The predictive model demonstrated a prediction error of 2.8% for powder-based DED and 2.3% for wire-based DED.

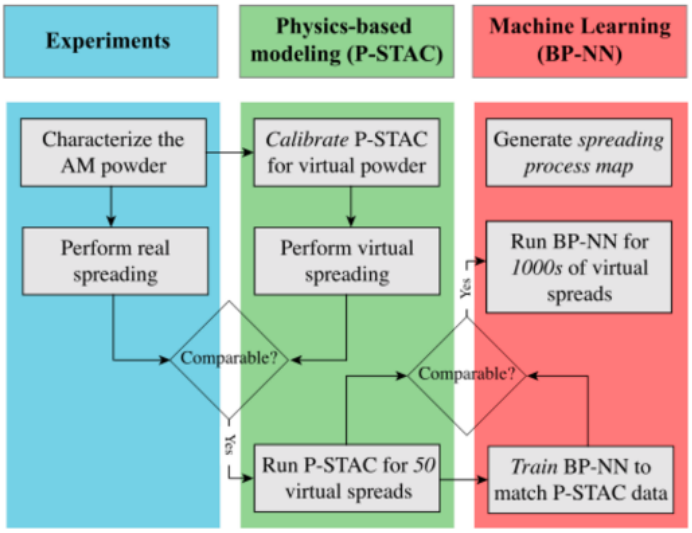

Fig. 20. The collaborative integration of experimental work, physics-based DEM simulations, and ML techniques [162].

Aside from the surface features, microstructure has also been of interest to the researchers. Cao et al. [164] used the Generative Adversarial Network (GAN) model to quantitatively predict alpha phase morphology in additively manufactured Ti-6Al-4V specimens. Due to its efficient handling of image datasets, the GAN model is a promising option for exploring the relationships between microstructure and manufacturing processes. Fig. 21 shows that the GAN model is trained to analyze and learn the complex details of the needle's physical structure, including its shape and size. Once the model has gathered sufficient data, it can reconstruct the predicted microstructure morphology in a visually understandable form, as depicted in Fig. 21.

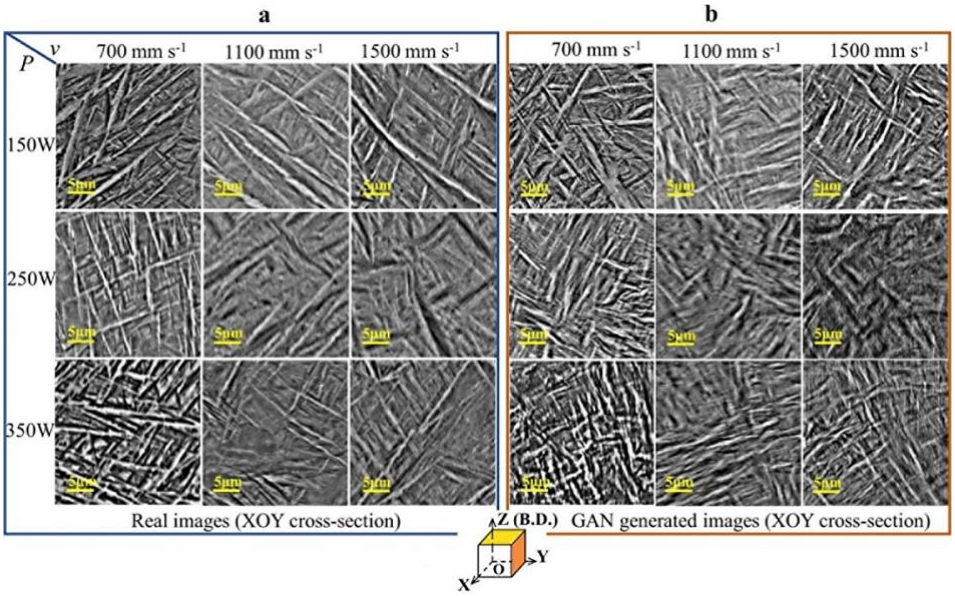

Fig. 21. XOY cross-sections of L-PBF fabricated Ti-6Al-4V; (a) real micrographs and (b) micrographs produced by GAN [164].

Yao et al. [115] conducted a study using an ML-based processing parameter optimization approach to identify the proper sets of processing parameters, resulting in a superior synergy of strength and ductility in L-PBF. As shown in Fig. 22, the formation and morphology of α' phases and the resultant properties (Fig. 22c) were investigated by considering the influence of L-PBF process parameters and heat treatment influence (Fig. 22a) as the ML model features. Moreover, the researchers used the partial dependence plots generated by the ML models (see Fig. 22b) to determine that the maximum ductility may be achieved at P/V=0.1 (J/mm), and the hatching distance was determined through experimentations.

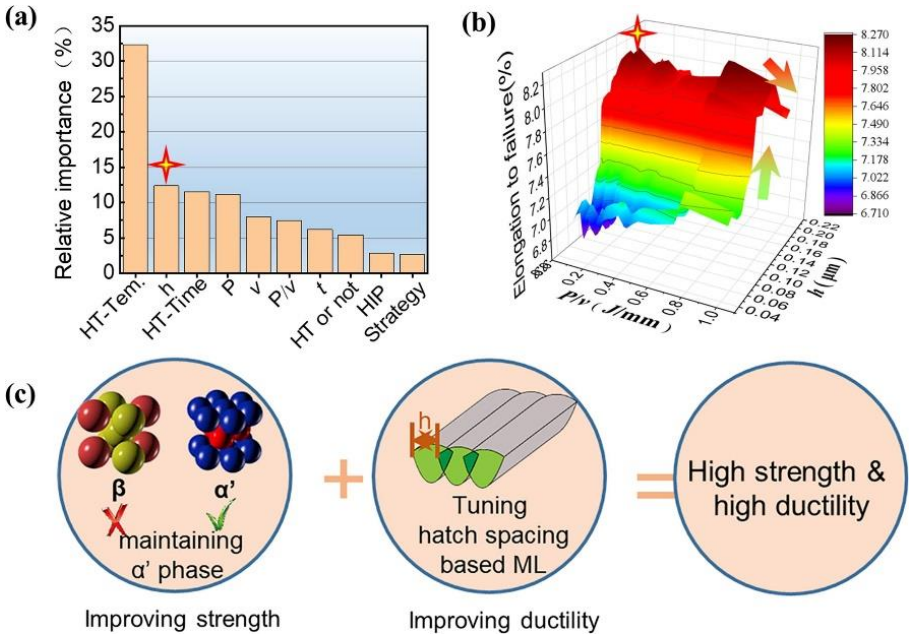

Fig. 22. (a) The relative importance of different features that affect ductility in L-PBF-produced Ti64 alloys, as calculated using ML. (b) The 3D contour map, and (c) a schematic illustrating the design concept for simultaneously enhancing both strength and ductility in the studied sample [115].

2.3.2. Geometric Deviation Control

Frequently encountered issues with AM components include low geometric precision and suboptimal surface quality [165]. These challenges hinder the widespread adoption of AM in different industries, such as the aerospace and medical sectors [166]. To address this issue, ML models can identify geometric imperfections, quantify the degree of deviation, and suggest solutions to improve these issues. For example, Francis et al. [125] developed a framework that compensates for geometric errors in the L-PBF process using a CNN model. The ML model, after being trained, could predict distortions by considering thermal data and a set of process variables. This ultimately generated an error detection and correction outcome within the CAD model. According to reports, this method improved the geometric precision of objects produced with the adjusted CAD model. In this case study, the authors utilized the CAMP-BD approach, which is a combination of a CNN and ANN, designed to predict results by analyzing extensive datasets. As shown in Fig. 23, the input information comprises the tensor structure of the thermal history and the processing/designing parameters. At the same time, the deep learning model predicts which set of data corresponds to the output data, specifically distortion.

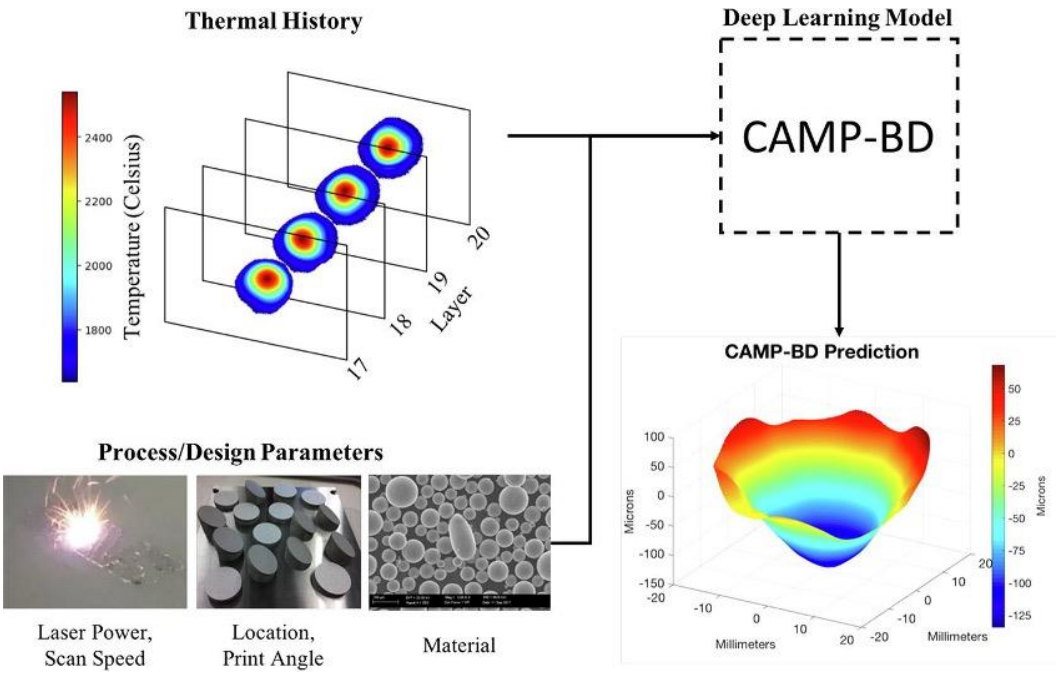

Fig. 23. Illustration of the procedure of geometric error compensation proposed for Ti-6Al-4V in L-PBF using CAMP-BD [125].

Zhu et al. [167] used the CNN method in the L-PBF Process to predict geometric deviation in AM parts. They employed Ansys Additive as an AM simulation software to generate the deviation data. Three processing parameters, part size, and a multi-channel model were used to predict deviation profiles on a 2D layer with a deviation field consisting of three channels as input. The convolution and pooling operations were performed at two stages, forming the suggested network. To overcome the problem of the limited dataset, they used Statistical Shape Analysis to increase the data and generate new samples.

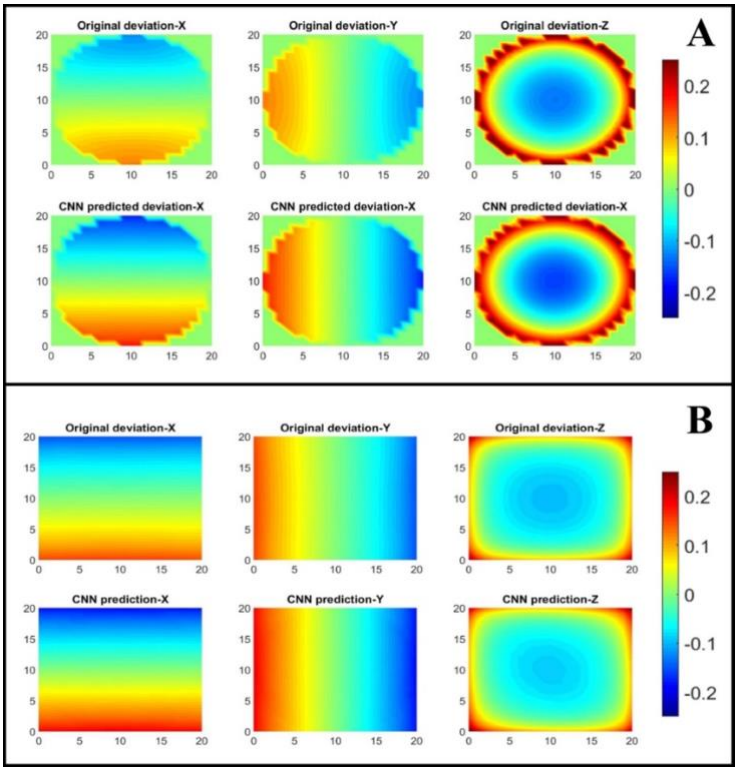

Fig. 24. Comparative analysis of the original deviation profile and the CNN prediction for (A) cylindrical shape and (B) square shape [167].

2.3.3. Defect Detection and In-situ Monitoring

The accuracy of human visual inspection is subject to errors and irregularities; nonetheless, the accurate detection of errors is highly prioritised in the AM process. Regarding defect detection issues, a crucial first step towards achieving in-process quality assurance is establishing a correlation between process conditions and defects [72,168]. Table 2 lists some case studies that focus on the application of ML in AM for defect detection. For instance, Gobert et al. [169] captured layer-wise images of the AM process during L-PBF. The images illustrated in Fig. 25 were subsequently utilized as input data for computed tomography scans to identify defects. The input data consisted of layer-wise images captured under varying lighting conditions. The main objective of the ML algorithm was to accurately classify whether each layer displayed any anomalies or not.

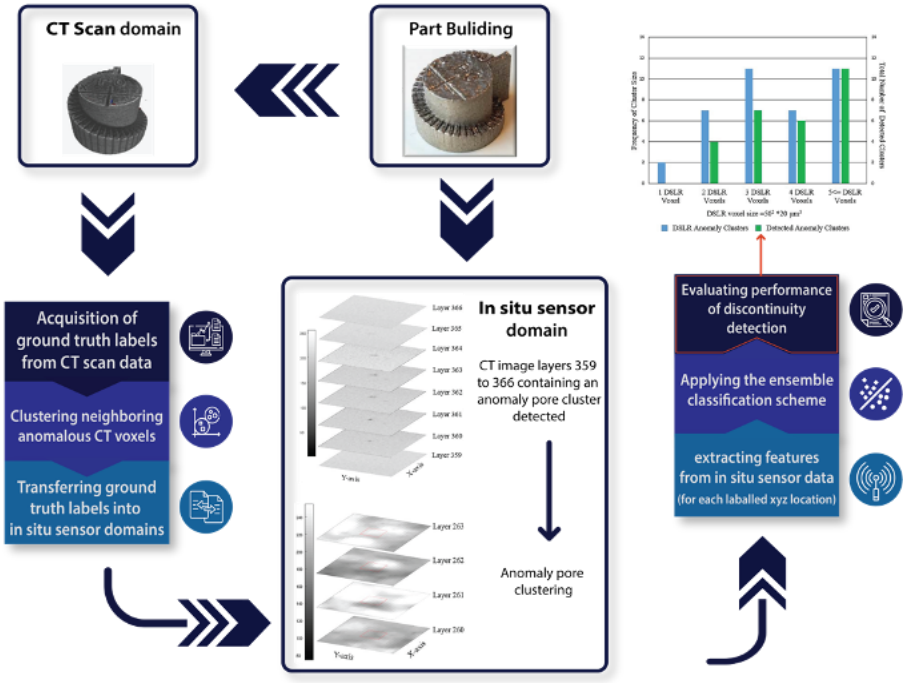

Fig. 25. Schematic of the procedure proposed by Gobert et al. [169]. The left side of the illustration depicts anomaly extraction from CT scans, while In-situ sensor imagery is shown at the center. Feature extraction, supervised ML, and performance assessment are also depicted on the right.

In a previous study, Ye et al. [170] presented a layer-wise monitoring framework for quality control of AM using in-situ point cloud fusion (Fig. 26). Their approach maximized the advantages of 3D scanning for direct monitoring, resulting in a more accurate assessment of morphological changes. The results showed an improved ability to identify small changes that can impact the overall quality of the component.

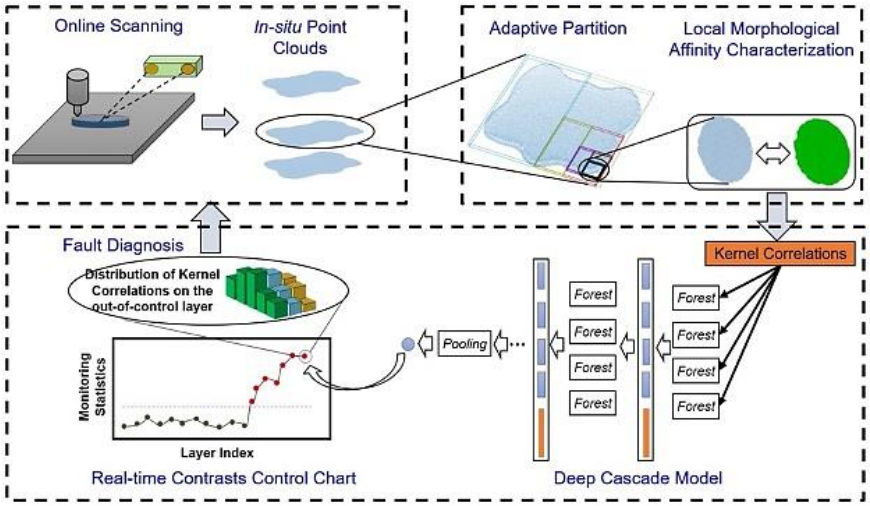

Fig. 26. The schematic of the framework of the selected methodology in the study by Ye et al. [170].

Early detection of defect formation can be facilitated by integrating in-situ monitoring with unsupervised learning techniques. Scime et al. [86] applied unsupervised learning techniques for anomaly detection within the powder layer of the L-PBF process. As illustrated in Fig. 27,

they used images of powder beds as input for their ML model, intending to classify various anomalies that could lead to irregularities in powder spreading. Filters generate different responses depending on the distribution of images. Pixel responses are recorded as vectors and clustered using the k-means algorithm. Each cluster is defined by an average response vector known as "visual words". Filter response vectors are compared to the closest visual word in the dictionary. The fingerprint of each training image patch is recorded in a tabular format. Results from the three patch-type analyses, along with CAD data, are integrated using context-driven heuristics to classify anomalies for individual pixels in the powder bed image.

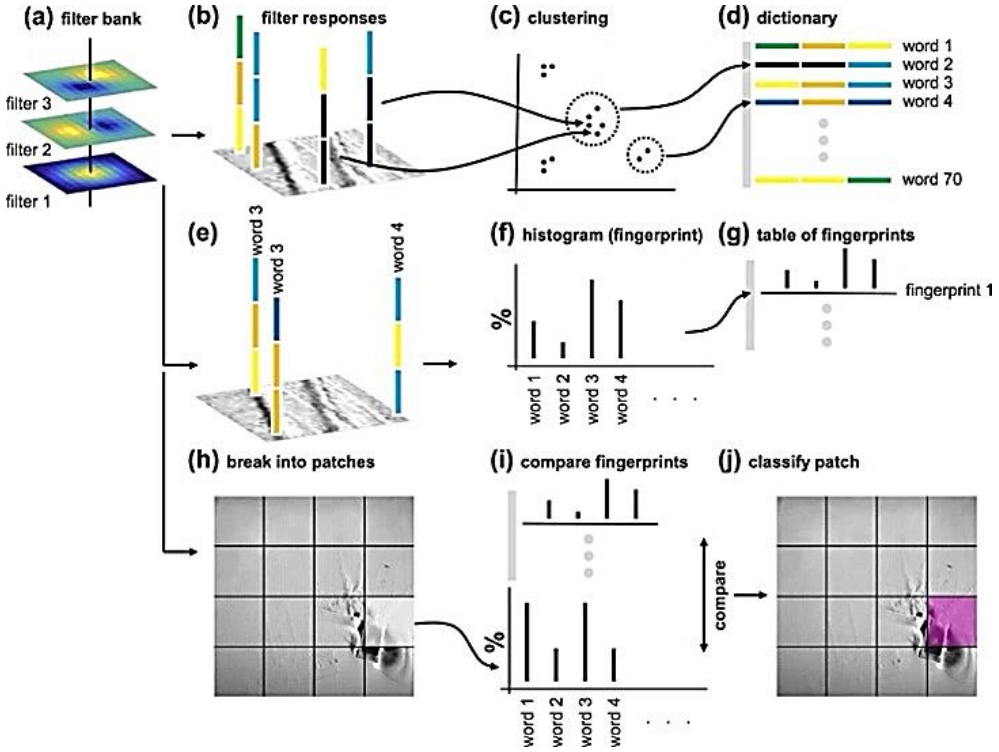

Fig. 27. Schematic of ML procedure applied in the case study proposed by Scime et al. [86] for in-situ monitoring and analysis of powder bed images.

Surface anomaly identification has gained significant interest in minimizing the need for expensive post-processing work due to the uneven and rough surface finish characteristic of DED-printed components. Kaji et al. [171] employed DBSCAN (Density-based spatial clustering of applications with noise) and RAND-LA net to detect surface anomalies in a powder feed DED system, achieving a prediction accuracy of 93%. A laser line scanner was used to acquire 2D surface profiles from the DED-built part surface to create a 3D point cloud. The validation results, shown in Fig. 28, indicate the model struggles to recognize concave surfaces. This is because these surfaces are global features, that are difficult to detect using the DBSCAN clustering algorithm and the RandLA-Net model.

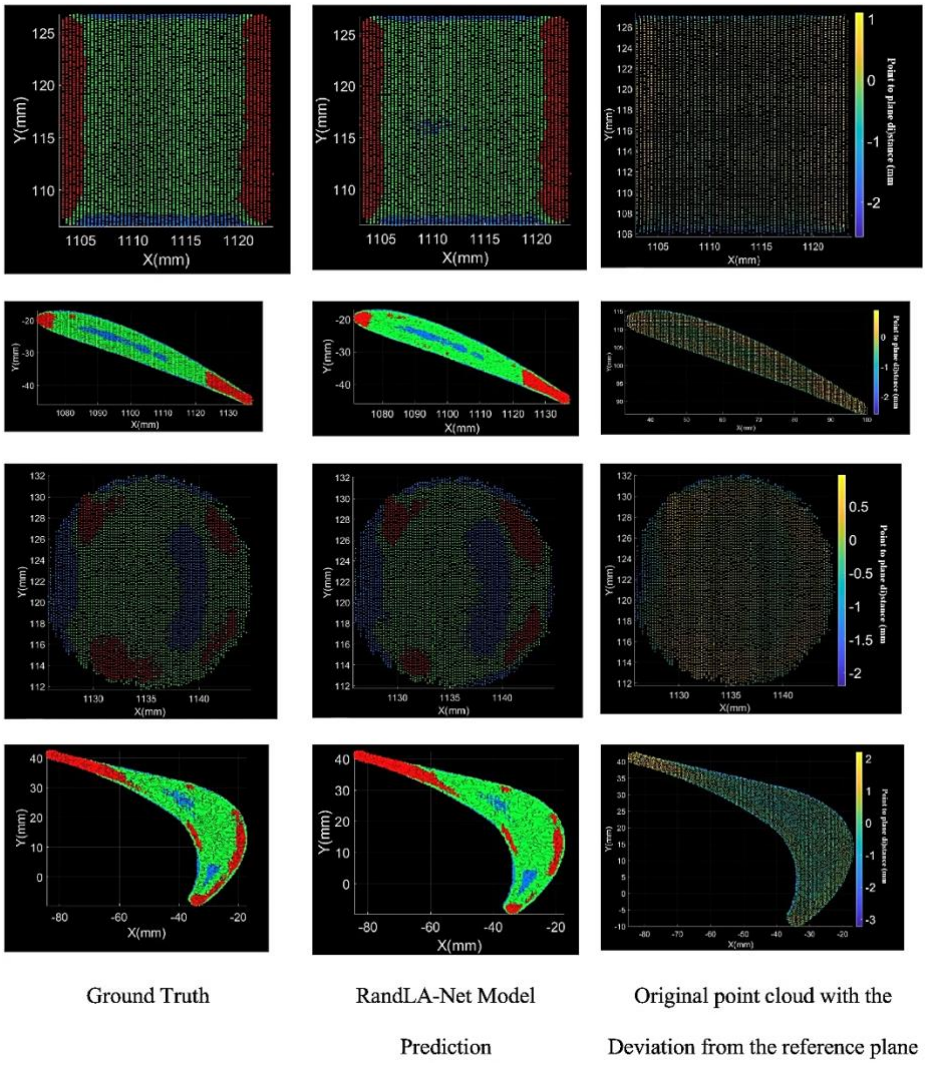

Fig. 28 Comparison of RandLA-Net prediction with Ground Truth (GT). The colors depict different surface types: red for convex, blue for concave, and green for normal surfaces [171].

Gaikwad et al. [172] used the L-PBF process to create a ML model that examines the quality of a single track printed with Stainless Steel 316L powder. The Sequential Decision Analysis Neural Network (SeDANN) algorithm was used for this purpose. The input data was gathered by pyrometer and high-speed video camera. The model analyzed the effects of printing parameters, such as laser power and velocity, on the quality of the single track. The study found that the SeDANN algorithm had higher accuracy than other ML models in detecting balling, lack of fusion, conduction, and keyhole during the process monitoring.

Du Plessis [173], examined the effect of process parameters on the formation of defects in L-PBF Ti6Al4V. The results showed that while higher scanning speeds offered a safer processing window for avoiding pore formation, the possibility of keyhole formation increased with increasing laser power. Understanding the interactions between lasers and materials as well as the dynamics of melt pools, is crucial in reducing the formation of defects such as keyhole pores. Laser absorption as a result of keyhole formation was investigated by Jiang et al. [174] using a deep learning method, while Synchrotron X-ray imaging was used to generate input data for the ML models. The authors reported a mean absolute error of less than 3.3% [174].

Similarly, Gorgannejad et al. [175] used X-ray imaging to train data fusion ML models for predicting the localized evolution behavior of keyhole pores. The authors also utilized thermally induced optical emission measured using both off-axis and coaxial photodiode sensors, as well as acoustic emission. According to heavily featured models, it was observed that the prediction results depended largely on the acoustic monitoring signal, with a secondary contribution from the optical emission sensors.

3. Materials and methods

3.1. Sample Modeling

First, the CAD files were created to do sample modeling, and the production process was carried out by the specific machine. The operations commenced with the creation of the CAD files, wherein 64 cubes and CD files were modeled for each component. Fig. 29 displays the exact measurements of the samples.

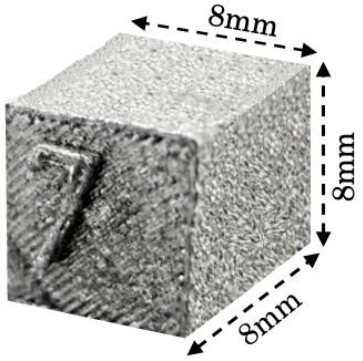

Fig. 29. Nominal dimension of the cubic samples

At this step, the software Materialise Magics was used to input the pre-selected process parameters for each component. It is crucial to acknowledge that each component was allocated a specific laser speed, laser power, and hatch distance, leading to unique features for each component once it was printed.

3.1.1. Design of experiment

The Design of Experiment (DoE) includes all different process parameter settings used in this project. Before starting the L-PBF process, there are several parameters that can be modified. These parameters are the necessary machine settings needed to manufacture a component using powders. To simplify matters, these process parameters are divided into four groups: laser-related, scan-related, powder-related, and temperature-related parameters. The laser-related characteristics encompass laser power, wavelength, spot size, pulse duration, and pulse frequency. Scan-related characteristics encompass the velocity at which scanning occurs (scan Speed), hatching distance, and the specific pattern used for scanning. The factors connected to powder include particle size and distribution, particle shape, powder bed density, layer thickness, and material qualities. The temperature-related characteristics include the temperature of the powder bed, the temperature of the powder feeder, and the uniformity of temperature [176].

The selection of appropriate process parameters is crucial for improving product quality. The interaction between these parameters is important to highlight because changing one parameter can sometimes produce the same result as changing another. In general, it is necessary to maintain a balance between all criteria. To optimize production rate and enhance quality of the production, which are the is the main goals of this thesis research, it is essential to choose the optimal process parameters. While all process parameters affect the efficiency of the process, Only the most influential individuals were considered to obtain the desired results. After careful

consideration, 64 experimental data points were selected for a wide range of three process parameters, including laser power (P), laser speed (v), and laser hatch distance (h) which are reported in Table 3. The process parameter selection was made based on our experience with the machine and a preliminary analysis that has not been reported. In the next step, the EP Hatch Prima software was used to define these process parameters, generating 64 different CAM and CLI files. As reported in Table 3, the laser power varied between 100 and 340 W, while the scan speed and hatch distance ranged from 400 to 1000 mm/s and from 0.1 to 0.2 mm, respectively. The wide variety of parameters led to a major variation in an applicable term named volumetric energy density (VED), which quantifies the amount of input energy per unit volume of the powder bed. The concept of VED was first established in references [177,178] to Attain substantial significance by comparing the different sets of parameters. VED, mentioned in Eq. 1, in this thesis, is used to evaluate the relative density of materials processed with L-PBF [179].

$$\text{VED} = \frac{P}{V \times h \times l} \qquad \text{Eq. 1}$$

Where:

$$\text{VED} = \text{Volumetric energy density } [\frac{J}{mm^3}]$$

$$\text{P} = \text{Laser power } [\frac{J}{s}]$$

$$\text{v} = \text{Scanning speed } [\frac{mm}{s}]$$

$$\text{h} = \text{Hatching distance [mm]}$$

$$\text{l} = \text{Layer thickness [mm]}$$

Subsequently, the predefined files served as the input for the PrintSharp 250 machine. Fig. 30 illustrates the design of 64 components, with their respective CAM files being visible.

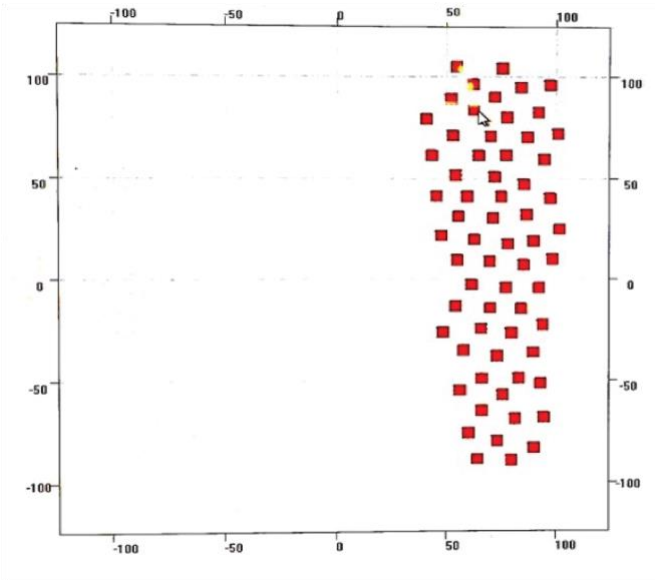

Fig. 30. Illustration of the CAM model which depicts the positioning of the 64 components on the platform used in L-PBF process.

Table 3. Process parameters for each sample used in this thesis.

s. ID	Power[W]	Scan speed[mm/s]	Hatch Distance[mm]	VED[J/mm^3]	s. ID	Power[W]	Scan speed[mm/s]	Hatch Distance[mm]	VED[J/mm^3]
1	190	400	0.1	158	**33**	190	400	0.12	132
2	190	600	0.1	106	**34**	190	600	0.12	88
3	190	800	0.1	79	**35**	190	800	0.12	66
4	190	1000	0.1	63	**36**	190	1000	0.12	53
5	200	400	0.1	167	**37**	200	400	0.12	139
6	200	600	0.1	111	**38**	200	600	0.12	93
7	200	800	0.1	83	**39**	200	800	0.12	69
8	200	1000	0.1	67	**40**	200	1000	0.12	56
9	270	400	0.1	225	**41**	270	400	0.12	188
10	270	600	0.1	150	**42**	270	600	0.12	125
11	270	800	0.1	113	**43**	270	800	0.12	94
12	270	1000	0.1	90	**44**	270	1000	0.12	75
13	340	400	0.1	283	**45**	340	400	0.12	236
14	340	600	0.1	189	**46**	340	600	0.12	157
15	340	800	0.1	142	**47**	340	800	0.12	118
16	340	1000	0.1	113	**48**	340	1000	0.12	94
17	190	400	0.11	144	**49**	190	400	0.13	122
18	190	600	0.11	96	**50**	190	600	0.13	81
19	190	800	0.11	72	**51**	190	800	0.13	61
20	190	1000	0.11	58	**52**	190	1000	0.13	49
21	200	400	0.11	152	**53**	200	400	0.13	128
22	200	600	0.11	101	**54**	200	600	0.13	85
23	200	800	0.11	76	**55**	200	800	0.13	64
24	200	1000	0.11	205	**56**	200	1000	0.13	51
25	270	400	0.11	136	**57**	270	400	0.13	173
26	270	600	0.11	102	**58**	270	600	0.13	115
27	270	800	0.11	82	**59**	270	800	0.13	87
28	270	1000	0.11	258	**60**	270	1000	0.13	69

s. ID	Power[W]	Scan speed[mm/s]	Hatch Distance[mm]	VED[J/mm^3]
29	340	400	0.11	172
30	340	600	0.11	129
31	340	800	0.11	103
32	340	1000	0.11	158

s. ID	Power[W]	Scan speed[mm/s]	Hatch Distance[mm]	VED[J/mm^3]
61	340	400	0.13	218
62	340	600	0.13	145
63	340	800	0.13	109
64	340	1000	0.13	87

Following manufacturing the 64 cubic samples to provide a more comprehensive investigation on VED, process parameters, and porosity formation, seven extra components were collected from other studies [17] to investigate the correlation between porosity and mechanical properties, see Table 4.

Table 4. The process parameters of the seven extra samples collected from other studies [17]

s. ID	Power[W]	Scan speed[mm/s]	Hatch Distance[mm]	VED[J/mm^3]
1	100	1000	0.1	33
2	200	1000	0.2	33
3	100	800	0.1	42
4	150	1000	0.12	42
5	200	800	0.2	42
6	270	1000	0.2	45
7	190	1000	0.13	49

3.2. Samples Manufacturing

The samples were produced using the PrintSharp 250 (Fig. 31), a PBF machine designed for medium-volume applications. It is specifically intended for the industrial manufacture of complex components and offers great flexibility when it comes to managing parts. The technical features of the machine are documented in Table 5.

Fig. 31. Prima Additive Print Sharp 250

Table 5. The technical parameters of the PrintSharp 250

Category	Specification
Dimensions (LxWxH)	3500 (L)- 1100 (W)- 2450 (H) mm
Weight	2000 kg
Power Supply	380 V/50 Hz/8kW
Type of laser	Yb (Ytterbium) Fiber Glass
Laser Power	200 W/ 500 W (Optional)
Laser Focus Diameter	70 – 100 µm
Beam Wavelength	1060 – 1080 nm
Building Volume	250 x 250 x 300 mm
Beam Deflection Speed	8 m/s
Positioning Speed	10 m/s
Build rate	12 – 30 cm^3/h
Layer Thickness	0.02 – 0.1 mm
Layer Width	0.1 mm (single line width)
Recoater Specs	Travel: 650 mm
Building Platform z-axis	Travel: 300 mm/Speed max : 6 mm/s/Res: 0.01 mm
Heating Platform	Up to 200°C
Monitoring of O_2 Level	Below 100 ppm
Permissible Room Temperature	15 – 30°C
Gas (Consumption – running/filling)	7 l/min (running)
System Fill Consumption	20 l/min (up to filling)
Cam Software	Materialise Magics
Control & Other Software	Eplus control software (EPC)
Industrial Interfaces	Ethernet

The materials used were gas-atomized AISI316L stainless steel powder, supplied by Oerlikon, and gas-atomized copper powder from Sandvik Osprey Ltd. The copper and stainless steel powders were mixed for 16 hours in a low-energy ball mill without the presence of milling balls. The ultimate powder mixture consisted of 2.5 weight percent copper. The chemical composition and morphology of the initial powder mixture are presented in Fig. 32. displays the morphology and related Energy Dispersive X-ray Spectroscopy (EDS) elemental maps of the initial powder mixture. The powder distribution analysis reveals that the average particle diameter of the blended AISI316 and Cu is 27 µm, with specific values of 13 µm for d10, 23 µm for d50, and 40 µm for d90. Similarly, the average particle diameter of Cu is 6.3 µm, with specific values of 3.1 µm for d10, 5.3 µm for d50, and 13.1 µm for d90. Table 6.displays the chemical composition of the Cu-containing AISI316L stainless steel powder utilized in this study, as determined by EDS.

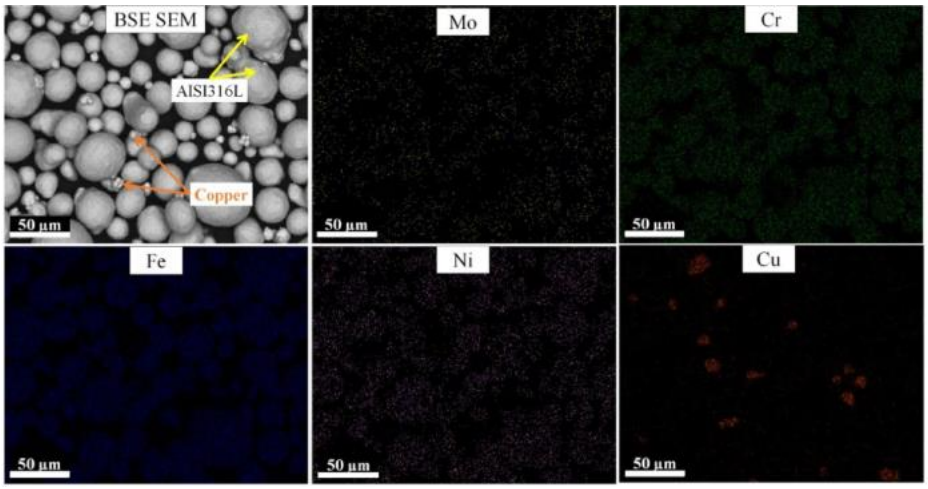

Fig. 32. Schematic of a scanning electron microscope (SEM) image of a mixture of powders accompanied by elemental maps obtained using energy-dispersive X-ray spectroscopy (EDS)[180].

Before starting the production process, the build chamber was thoroughly emptied to a residual oxygen level of less than 0.1%. High-purity Argon was used to preserve an inert atmosphere within the construction chamber and minimize the likelihood of oxidation. A scanning approach was employed using a bidirectional stripe scanning pattern with a 67° rotation between each succeeding layer. The layer thickness of all samples was set to 30µm in this project [180].

Table 6. The chemical composition of the combined AISI316L-Cu powder was determined both nominally and by analysis[180].

Elements	Cr	Ni	Mo	C	Mn	Cu	P
Nominal (wt%)	17-19	13-15	2.25-3	0.03	2.0	2.5	25
Analysed (wt%)	17.02	13.5	2.04	0.02	2.11	2.92	22

In Fig. 33, the highlighted section illustrates the laser in operation during the LPBF process. The laser accurately melts a small layer of metal powder to create the desired shape. The process of melting is fundamental to LPBF, as it enables the fabrication of complex and highly

accurate metal parts through the sequential deposition of layers. Fig. 33 illustrates the manufactured samples on the building platform after the completion of the building process. After completing the production process, all parts stuck to the building platform were removed from the workspace and meticulously cleaned. Finally, the samples were cut from the platform employing a Wire Electrical Discharge Machine (W-EDM). It is worth noting that the samples were labeled during the production with a numerical value (sample ID in Table 3) to signify their distinct process parameters. The x-axis corresponds to the recoater orientation, while the z-direction aligns with the building direction.

(a) (b)

Fig. 33. (a) Schematic of the platform during job running, (b) the result after completion of production.

3.3. Sample characterization

First, the W-EDM was used to separate the parts from the platform. Then, the density of the components was determined using an Archimedes balance. After conducting density measurements and analysis, specific components were chosen for tomography and metallography analysis. Finally, the microstructure of these samples was analyzed using an optical microscope for metallography data and the VGStudio software for XCT data.

3.3.1. Cutting Machine

The G.cut WEDM machine was utilized to cut the samples at this particular stage. This machine is shown in Fig. 34. Section 1 corresponds to the software interface of the cutting machine, where the settings for wire movement, the auto process, and the start and stop buttons for cutting are managed. Section 2 displays the X, Y, and Z coordinate directions, which assist in ensuring the cutting is performed in the correct direction. Section 3 is the main part of the machine, where the workpiece is placed, and the cutting operation is carried out. To start the process, the platform must be attached to the W-EDM using clamps. Next, using the specific software in the computer connected to the machine, a surface touch was established between the wire and the platform to create the reference point for both the x and y coordinates. After

adjusting the exact location for the wire starting point, the appropriate dimensions and correct orientation were loaded into the machine to commence the cutting operation. Finally, the printed components were separated and prepared for further procedures.

Fig. 34. Key components of the WEDM machine: Section 1 (software controls), Section 2 (coordinate display), and Section 3 (cutting area).

The wire-cutting machine uses an electrically charged slender wire to cut the samples with the highest accuracy. This method operates by generating electrical discharges between the wire and the workpiece, gradually removing material along the cutting direction. The sparks, as shown in Fig. 35 are produced rapidly and efficiently, resulting in the removal of small quantities of metal and the desired shape of the workpiece. Throughout the cutting procedure, a constant flow of deionized water is employed to cool both the wire and the workpiece, thereby preventing excessive heat and removing the eroded particles. In this process, water is also used as a dielectric, which is essential for the occurrence of the electrical discharge process. The words "time on" and "time off" pertain to the length of the electrical pulses (on-time) and the gaps between them (off-time), respectively. The parameter "t_{on}" regulates the energy and length of each spark, which directly impacts the cutting speed and surface quality. On the other hand, "t_{off}" enables a brief cooling period, minimizing the potential for thermal damage and enhancing the accuracy of the cutting process. These parameters are essential for maximizing the cutting efficiency and ensuring the high quality of the end product [181].

Fig. 35. Illustration of electrical sparks and the movement of water during the wire-cutting procedure.

3.3.2. Archimedes density

The Archimedes approach is employed to determine the relative densities of components produced by SLM [182]. This method involves weighing a single sample in two distinct fluids. Typically, the fluid used for reference is air. The second fluid consists of distilled water, acetone, or ethanol. While distilled water is frequently utilized [183], it may only sometimes be appropriate due to the potential formation of air bubbles on the sample surface. This phenomenon occurs significantly in lattice structure components when air bubbles prevent the complete penetration of water into the interior of the mesh due to the high surface tension of the water[184].

According to the ASTM F3637-23 [185], the Archimedes density measuring method was done for each sample to calculate its geometrical and Archimedes density. Firstly, the measurement chamber is prepared, and the beaker is filled with distilled water, with a density of 0.997 $\frac{g}{cm^3}$. Subsequently, the device is accurately calibrated, to measure the dry weight (w_{dry}) of the sample, as depicted in Fig. 36 (part 1). Once the dry weight of the sample is determined, it is shown on the digital monitor, as illustrated in Fig. 36, part 3. Upon finishing this procedure, the device is reset to a value of zero, and the sample is placed on the filter, as depicted in Fig. 36 part 2, to be fully immersed in distilled water. All the bubbles that had been formed were eliminated, and the sample was completely submerged in the water. The weight at this point was documented as $w_{immersion}$. Subsequently, the sample was extracted from the water, placed on the wet wipes, and promptly reweighed, as shown in Fig. 36 (part 1) to measure the amount of water that had been absorbed during immersion. This phase resulted in obtaining the wet weight, indicated as w_{wet}. Furthermore, the theoretical density of the powder was set to be 7.985 $\frac{g}{cm^3}$ using the relative technique. This method considers that the powder consists of 2.5% copper and 97.5% AISI316. Subsequently, the total porosity percentage and relative Archimedes density percentage for all samples were computed utilizing the given formulas:

$$\rho_{Archimedes} = \rho_{liquid} * \frac{w_{dry}}{w_{dry} - w_{immersion}} \quad \text{Eq. 2}$$

$$\rho_{Geometrical} = \rho_{liquid} * \frac{w_{dry}}{w_{wet} - w_{immersion}} \quad \text{Eq. 3}$$

$$\text{Total porosity percntage} = \frac{\rho_{teorethical} - \rho_{bulk}}{\rho_{teorethical}} * 100\% \quad \text{Eq. 4}$$

$$\text{Relative Archimedes Density percntage} = \frac{\rho_{Archimedes}}{\rho_{teorethical}} * 100\% \quad \text{Eq. 5}$$

Where:

$\rho_{Archimedes}$ = Archimedes density (apparent density) $[\frac{g}{cm^3}]$

$\rho_{Geometrical}$ = Geometrical density (bulk density) $[\frac{g}{cm^3}]$

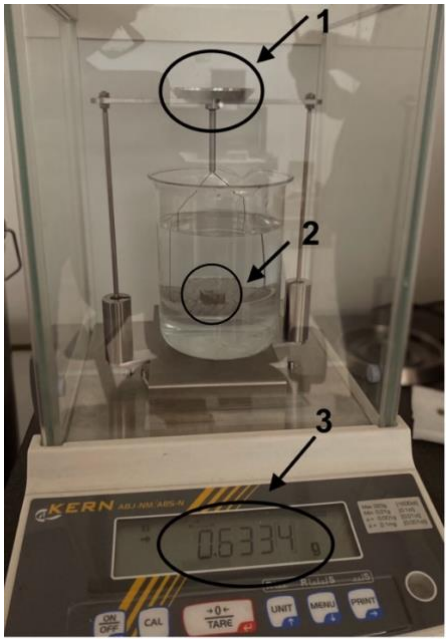

Fig. 36. The illustration of the measurement setup for Archimedes density is 1) a position for measuring the dry and wet weight, 2) place for measuring the immersion weight, and 3) a digital display for showing the weight values.

3.3.3. X-ray computed tomography

XCT employs algorithms to construct 3-D representations by combining many X-ray images taken around a rotational axis [160]. In recent years, three primary XCT techniques have been developed, each enhancing the speed of data collection. The initial XCT method acquires density data along each beam of X-rays that is linearly displaced in the opposite direction of an X-ray detector. A small increment rotates the scanner, and this process is repeated until a full 360° of data is acquired. In the second technique, a two-dimensional array of X-rays is used that covers the entire object width, along with a one-dimensional array of detectors positioned at the edges of the X-ray beam. The third approach employs a two-dimensional detector with a complete three-dimensional X-ray beam cone. The x-ray source and detector of

the beam scanner move in a straight line to scan a slice of the xy plane. The source and detector have slight movements in the z-axis for the measured item, and this process is repeated. The fan beam scanner exposes an entire slice of the object simultaneously, whereas the cone beam scanner exposes the entire thing. To capture the entirety of the item, each scanning method has a full rotation of 360°[187]. Fig. 37. shows each XCT approach. XCT evaluations focus on image quality, notably resolution and contrast. The maximum magnification of XCT images decreases with object size due to X-ray penetration, reducing resolution. Reducing magnification increases scan voxels and reduces image clarity. Low X-ray penetration makes measuring high-density materials difficult, limiting object size. This is because reliable contrast requires more prolonged exposures. Instead of scanning the whole object, XCT scanners measure a particular section or use a reference coupon with similar features. This improves image quality. This technique may increase scan quality but not capture the object of interest, which may skew the results.

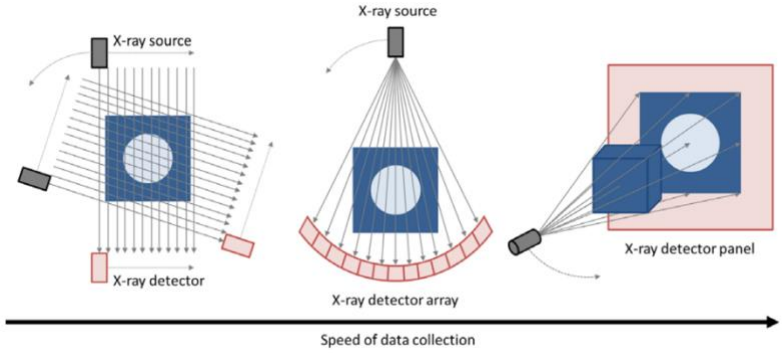

Fig. 37. Three different beam XCT schematics. The fan beam image shows a curved detector, whereas the cone beam image shows a flat panel detector. All of these schematics can be employed in each case[6].

Eleven samples were chosen for XCT analysis based on the Archimedes density measurement method data. These samples were analyzed by tomographic method to measure their porosity percentage and density, which would be compared with alternative methodologies. In addition, we obtained comprehensive data on porosity distribution, the geometries of porosities, their diameters, and other relevant features, which will be further elaborated in the results and discussion section. The samples were initially positioned on the holder in this procedure, as depicted in Fig. 38(a). In section (b) of Fig. 38, a copper filter was positioned in front of the X-ray gun. The sample position was verified and corrected using the software in the computer connected to the machine, as shown in Fig. 39, to guarantee that the sample stayed within the X-ray imaging frame. Once the correct placement is confirmed, the tomography process begins. Before introducing a new sample for tomography, it is imperative to eliminate any remaining residue by uniformly resetting the detector using X-ray beams.

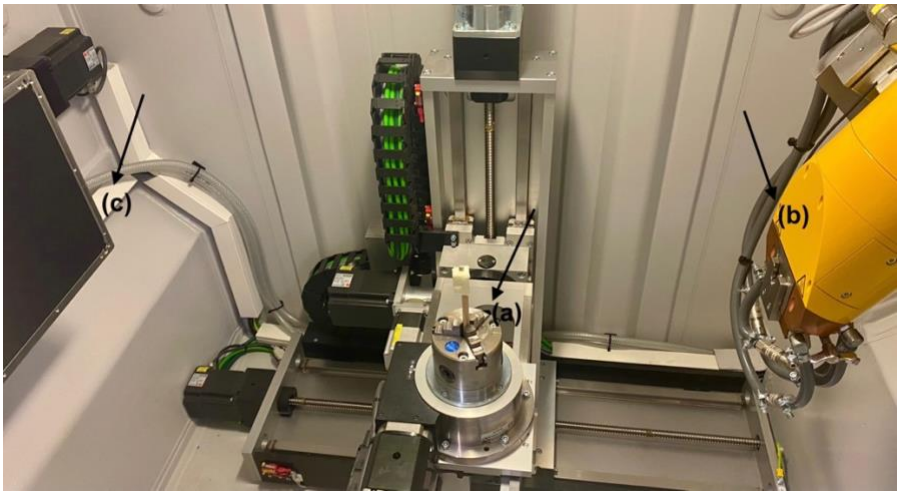

Fig. 38. A general representation of the interior XCT setup(a) sample holder for tomography.(b) X-ray beam gun. (c) Detector configuration for accurate tomography detection and imaging.

Fig. 39. The software interface checks and alters the sample's position during tomography analysis to keep it in the X-ray imaging frame.

3.3.4. Metallography

Following the completion of the tomography analysis of the eleven samples, metallographic analysis was conducted on these samples. Given the small size of the samples, it was necessary to mount them to assist in the subsequent grinding and polishing procedures. For the initial mounting stage, acrylic resin KMU and methyl methacrylate hardener were employed, as depicted in Fig. 40(a). The samples were placed in the mount frame in the specified orientation. A mixture consisting of a 2:1 ratio of resin to hardener was made by thoroughly mixing for a duration of one minute. Subsequently, the mixture was put into the mounting mold. After 15 minutes, the mounted samples were extracted from the mold, as depicted in Fig. 40(b). At this point, the samples were prepared for the processes of grinding and polishing.

(a) (b)

Fig. 40. (a)The acrylic resin and methyl methacrylate hardener were used for mounting the samples before the grinding and polishing process. (b) Mounted samples were removed from the mold, ready for the grinding and polishing process.

The process of grinding and polishing was conducted using a Presi machine, as seen in Fig. 41(a). First, abrasive papers with grit sizes of P480, P600, P800, P1200, and P2400 were chosen based on the material of the sample as shown in Fig. 41 (b). The grinding process commenced using the most abrasive paper, and the selected paper was dampened before being placed on the machine. Then, with a rotational speed of 150 rpm, the machine was turned on to polish the samples. At this step, to prevent scratches caused by residual particles, water is continually spread all over the abrasive paper. Following each grinding repetition, the sample was analyzed under a microscope to verify the visibility of the grinding lines. After identifying the distinct lines, the sample was rotated by 90 degrees, and a more refined abrasive paper was employed to eliminate the existing lines and generate fresh ones. This process was repeated until the final grinding stage using the P2400 paper was finished.

(a) (b)

Fig. 41. (a) The Presi machine was used for the grinding and polishing of the samples. (b) The selection of abrasive papers (P480, P600, P800, P1200, and P2400) used for grinding the samples.

After the grinding stage, the samples were polished to eliminate the scratches caused by the previous procedures. Polishing pads with grit sizes of 1 and 3 µm were used, as depicted in Fig. 42 The 1 µm pink pad was positioned on the device, and diamond suspension, together with a lubricant, as depicted in Fig. 43 (a), was utilized to attain a polished surface. Subsequently, the surface was further refined using the 3µm blue polishing pad and a 0.3 µm aluminum oxide solution, as shown in Fig. 43 (b).

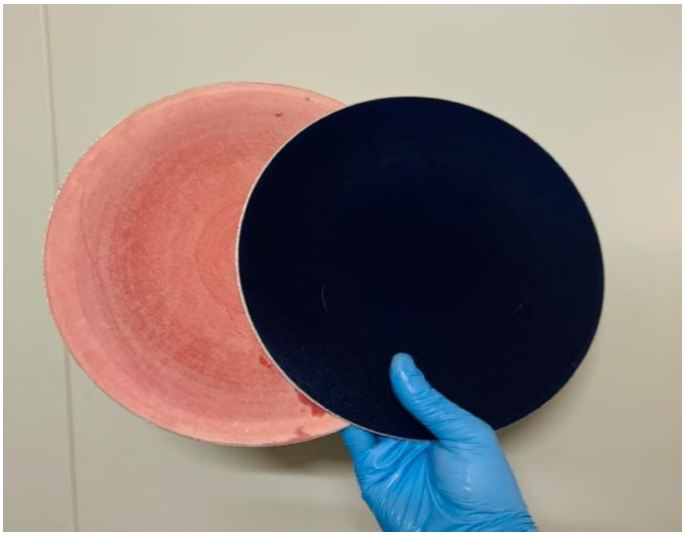

Fig. 42. Polishing pads with 1-micron(pink) and 3-micron(blue) grit sizes were used for polishing the samples.

(a) (b)

Fig. 43. (a) Diamond suspension and lubricant used during the polishing process by the 1-micron pink pad. (b) 0.3-micron aluminium oxide solution used during the polishing process with the 3-micron blue pad.

After finishing this stage, it was anticipated that the sample surfaces would exhibit a high degree of smoothness and reflectivity, such as a mirror, as depicted in Fig. 44. At this point, the samples were prepared for the subsequent phase, where the microstructure was investigated using an optical microscope.

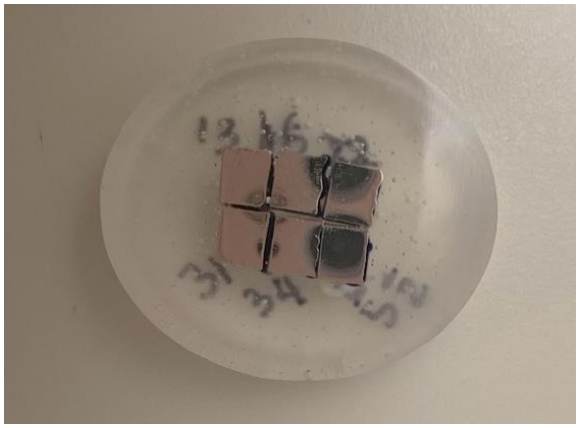

Fig. 44. The final appearance of the samples after grinding and polishing, with a smooth, mirror-like surface, ready for microstructural examination under an optical microscope.

3.3.5. Optical Microscope

The surface of the samples was analyzed using an optical microscope after being polished. In this investigation, a "LEICA" optical microscope (Fig. 45(a)) was utilized that offered magnification options ranging from 5x to 100x. Imaging was conducted using a calibrated black-and-white filter. In addition, the microscope is equipped with software that provides sophisticated image processing capabilities. The samples were placed on a specialized plane with the surface to be examined facing downward (Fig. 45 (b)). The surface analysis was performed using an optical microscope set at a magnification of 5x and 10x. Each surface was divided into nine different areas, creating a matrix. Nine different images were taken for each sample. The average porosity percentage of all nine images was determined to calculate the porosity percentage of a specific sample. The microscope's focus was accurately calibrated for each photograph to guarantee optimal sharpness of the surface pores. The photos depict black dots on the background, which symbolize the porosities found within the specific section.

(a)

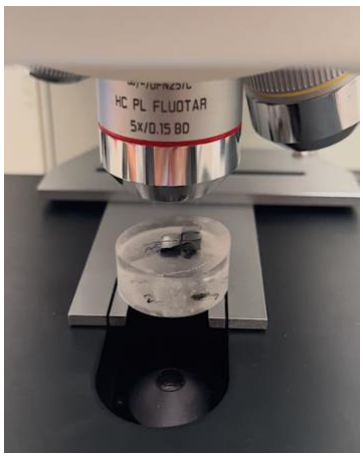

(b)

Fig. 45. Schematic of the optical microscope used for capturing high-resolution images of metallographically prepared and numbered samples. (b)The sample is placed in a down position for analysis using an optical microscope.

3.3.6. Image Analysis

Following the acquisition of the photos, they engaged in post-processing with the software known as ImageJ. ImageJ is a Java-based software that was developed by the National Institutes of Health in the United States for the purpose of processing and analyzing images. The porosity percentage of the samples was examined using the ImageJ software, as demonstrated in

Table 7 as an example of one of the samples with a porosity percentage of 2.329%. Since for porosity analysis, ImageJ requires an image that contains 8 bits, the first step consisted of converting the image into an 8-bit format, which ultimately led to the creation of a grayscale representation in which the color of each pixel is determined by the intensity of the greyscale. The software made it easier to quantify the proportion of pores on the surfaces as well as the diameters of the pores. By adjusting the threshold to prevent any distortions that were caused by polishing and any scratches that were still present, it became possible to precisely measure the percentage of darkened regions that corresponded to the pores in the samples (Fig. 46).

Table 7. Analysis of sample porosity using ImageJ software, demonstrating the quantification process of porosity within the sample.

	Area	Mean	StdDev	Mode	Min	Max	Median	%Area	MinThr	MaxThr
1	16708.651	255	0	255	255	255	255	2.329	255	255

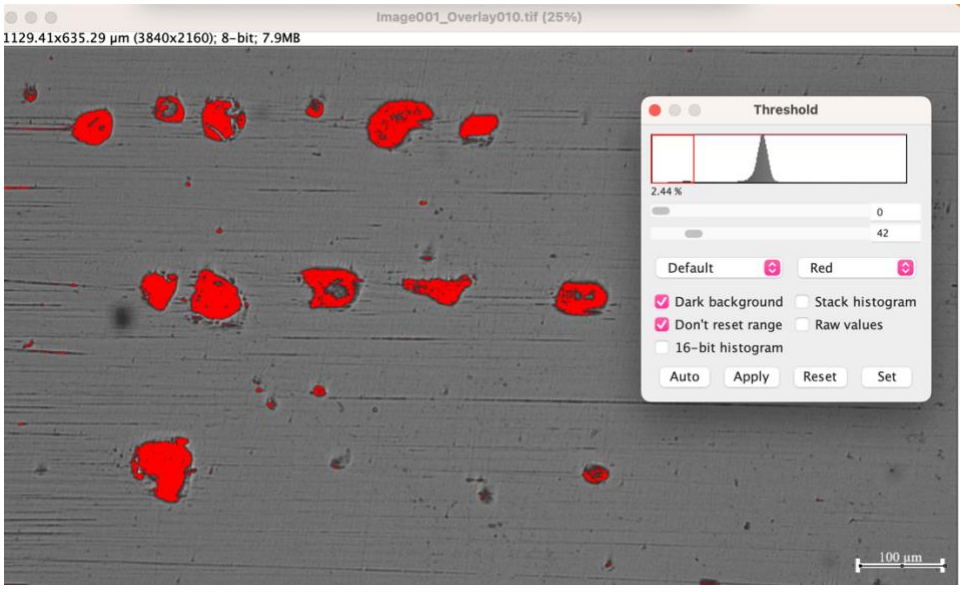

Fig. 46. Representation of the grayscale image was processed in ImageJ using thresholding to measure the pores (shown in red), while excluding any polishing errors and scratches.

3.4. Evaluation of ML algorithms

Applying a regression model typically requires multiple metrics for a comprehensive evaluation [187]. The accuracy of the chosen models is assessed using three statistical metrics: the coefficient of determination (R^2), the mean absolute error (MAE), mean square error (MSE).

The MAE represents the average absolute deviation for each statistic which is an indication of prediction accuracy[188]. MAE provides a more accurate representation of the actual amount of the prediction error, in contrast to other error metrics, by properly addressing the issue of error cancellation[189]. It should be noted that the MAE value is expressed in the same units as the original target variable. This feature facilitates comparisons among multiple machine learning models, specifically for the target data, rather than across different prediction tasks[187].

The Mean Square Error (MSE) denotes the sample standard deviation of the discrepancies between predicted and actual values, used as a metric that calculates the ratio between the squared differences of predicted and actual values, and the total number of data points. It is worth noting that the MSE is more sensitive to outliers compared to the MAE [189,190].

The coefficient of determination, often denoted as R^2, measures the strength of the relationship between two variables. It assesses the accuracy of the regression equation in fitting the observed data and capturing the variability in the dependent variable. Specifically, R^2 quantifies the level of the variation in the target variable that can be assigned to the changes in independent input variables in a regression model. Essentially, it signifies the degree of correlation between the input and target variables[72]. It is essential to note that assessing prediction accuracy by using only R^2, especially in non-linear regression, is inadequate. Therefore, in this study, R^2 is not the exclusive statistic for assessing model performance. Additionally, R^2 has certain limitations. Although, the increase of independent variables results in a rise in R^2, especially in large datasets, a very high value of R^2 may indicate an overfitted model, while an accurate model may have a reduced R^2. Negative R^2 values also indicate that predictions are worse than the mean target value[187]. MAE, MSE, and R^2 can be calculated by equations below.

$$\mathrm{MAE} = \frac{1}{n}\sum_{i=1}^{n}|y_i - \hat{y}_i| \qquad \text{Eq. 6}$$

$$MSE = \frac{1}{n}\sum_{i=1}^{n}(y_i - \hat{y}_i)^2 \qquad \text{Eq. 7}$$

$$\mathbf{R^2} = \frac{\sum_{i=1}^{n}(\hat{\boldsymbol{y}}_i - \overline{\boldsymbol{y}})^2}{\sum_{i=1}^{n}(\boldsymbol{y}_i - \overline{\boldsymbol{y}})^2} \qquad \text{Eq. 8}$$

Where y_i, $\hat{y}_i$, $\bar{y}$ represent actual, predicted, and mean values, respectively, and n is total number of data points. The high R^2 value and the low MAE and MSE values suggest that the analysis and statistical model are accurately representative[191].

To address the above-mentioned limitations and have a comprehensive analysis of algorithms accuracy, the Index of Merit (IM) is introduced in this study. As shown in equation (9) IM integrates the three statistical measures (MAE, MSE, and R^2) into a single metric that provides a more holistic view of model accuracy. A value closer to zero indicates optimal predictive performance, whereas values further from zero suggest decreasing accuracy [192,193].

$$\text{IM} = \sqrt{(MAE)^2 + MSE + (1 - R^2)^2} \qquad \text{Eq. 9}$$

4. Result and Discussion

4.1. Overview

This section highlights the results gained from the measurement methods outlined in the previous chapter. Fig. 47 presents a comprehensive illustration of the complete workflow, illustrating the utilization of ML models to analyze the data and optimize the process parameters by finding an accurate relationship between them and defect content.

Fig. 47also depicts the overall organization of the tasks performed in this part of the thesis, while the first three sections are related to the methodology procedure, which was explained in the previous chapter. These sections are essential as they provide the basis for the work done in this chapter. The following sections of the figure describe the procedures for data processing, model testing, and conducting a comprehensive analysis of the optimized parameters. The main data that has been analyzed in this thesis includes measured relative density percentages obtained through three distinct methodologies (Archimedes density measurement, image analysis, and XCT), specific process parameters and the calculated VED for each component. In the next step, the data was split into training and test sets, a standard procedure in ML processes for assessing model performance. In Fig. 47, the letter "i" denotes that the data partitioning into training and test sets iterated in several phases, employing different ratios, starting from 40 (train)/60 (test). Following the splitting of the data, a correlation heatmap was plotted to analyze the impact of each hyperparameter on model performance. Rather than exploring an excessively wide range of hyperparameters, which can be computationally expensive, shorter ranges were initially defined for almost all hyperparameters of each model. Three evaluated parameters exhibited the most significant influence and were selected for a detailed analysis. To do so, the impacts of these critical parameters were assessed using a large dataset by R^2 value. The optimal hyperparameter settings leading to the highest R^2 value were chosen for the subsequent analysis phase. Following identifying the optimal values of the first and second parameters, the influence of the third parameter was investigated. This analysis utilized 2D plots to assess errors through multiple metrics. The error plots facilitated the identification of the optimal range for the third parameter, which was chosen based on the maximum R^2 value achieved. After finishing the parameter tuning, the focus of the analysis turned to the prediction phase. During this phase, two-dimensional graphs were used to compare the predicted values with the actual values. Additionally, this process was repeated until the training size reached 90%, wherein the effect of training data size on model performance was examined by systematically increasing the training set size in 10% increments, from 40% to 90%. This approach investigates the sensitivity of each model to varying train-test data splits. Upon reaching the 90% training size threshold, the workflow advanced to the final stage, during which the optimal model and its associated hyperparameters were chosen. This chapter subsequently discusses a variety of ML models in detail. Upon reaching the specified training size, the outcomes of these models, including their optimal parameters and performance, are documented.

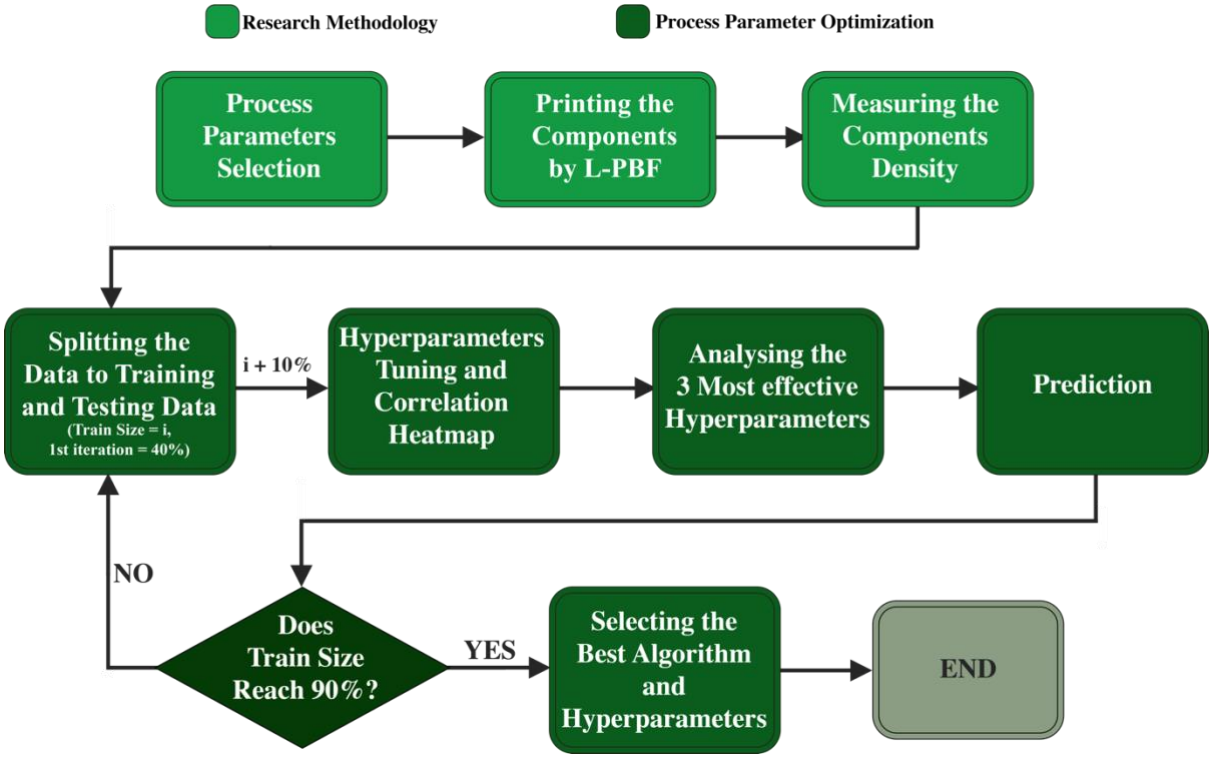

Fig. 47. An overview of the workflow is provided in this chapter, demonstrating the use of ML models to analyze data and optimize process parameters by finding a relationship between them and defect content. The initial three sections pertain to the approach, whereas the subsequent sections outline the process parameter optimization.

4.2. Data pre-processing

All data acquired from the three density measurement methods has been compiled in this section. Table 8 presents the relative Archimedes density percentages measured for each of the 64 samples. Furthermore, for a specific subset of chosen samples, the densities were assessed using two alternative methods, as detailed in Table 9. Upon gathering data from the three methodologies, the averages were computed to facilitate the implementation of different ML models (SVR, GPR, GBR, k-NN, DT, RF, BR) on the average density. The primary objective is to enhance the process parameters according to these models. The average values of 13 pieces were initially computed, and subsequently, these averages were extrapolated to the remaining pieces. This methodology provides a thorough analysis while considering the data constraints of specific techniques. As it was mentioned, to analyze the effect of training size on prediction accuracy, the data was divided into training and test sets.The process of applying multiple ML models was started with a training size of 40%. In each iteration, the training size increased by 10% to reach 90%. The analyses and conclusions are presented based on these chosen ratios. This precise data splitting and model setup procedure ensures that the performance of each algorithm is both powerful and reliable, resulting in important insights into optimizing process parameters. The findings of these analyses, including optimal arrangements for training and testing data, are detailed, providing the precise selection of the most appropriate ML models for the dataset.

Table 8. Relative Archimedes density percentages measured for all 64 samples

Sample ID	Relative Archimedes Density[%]	Sample ID	Relative Archimedes Density [%]
1	96.89	**33**	96.11
2	98.27	**34**	98.80
3	98.46	**35**	99.93
4	99.69	**36**	99.15
5	99.03	**37**	96.33
6	97.68	**38**	98.30
7	98.90	**39**	99.56
8	98.24	**40**	98.87
9	97.87	**41**	97.94
10	97.38	**42**	98.25
11	98.69	**43**	97.81
12	98.79	**44**	97.64
13	96.40	**45**	96.38
14	97.74	**46**	97.05
15	98.03	**47**	98.51
16	97.27	**48**	97.60
17	96.36	**49**	95.89
18	96.44	**50**	97.42
19	98.57	**51**	98.52
20	98.48	**52**	99.09
21	96.47	**53**	97.88
22	97.74	**54**	98.31
23	98.10	**55**	99.53
24	99.48	**56**	98.55
25	96.16	**57**	96.99
26	98.58	**58**	98.19
27	97.77	**59**	98.51
28	98.80	**60**	98.89
29	96.86	**61**	95.95
30	97.90	**62**	97.92
31	99.33	**63**	97.66
32	98.08	**64**	97.28

The results from the metallography and tomography techniques, as illustrated in Table 9, were determined by images obtained by optical microscopy and Tomography analysis. The optical microscope images were subsequently analyzed using ImageJ software. The porosity percentages were determined via image analysis of the tomographic data. This detailed analysis confirmed a thorough examination of the samples' surface and volumetric characteristics, providing significant insights into the materials' internal structure. Advanced imaging techniques and software facilitated a more precise assessment of porosity, thereby improving the overall accuracy of the data and its significance to the study.

Table 9. Porosity percentages for selected samples using two additional methods (metallography and XCT).

Sample ID	Porosity content by XCT [%]	Porosity content by image analysis [%]	Porosity content by Archimedes Density analysis[%]
5	0.99	-	0.97
7	1.09	-	1.10

Sample ID	Porosity content by XCT [%]	Porosity content by image analysis [%]	Porosity content by Archimedes Density analysis[%]
9	4.72	-	2.13
13	4.55	1.99	3.60
16	2.52	7.58	2.73
18	3.11	2.82	3.56
21	3.26	2.41	3.53
22	0.90	1.37	2.26
23	1.26	1.38	1.90
31	2.24	2.11	0.67
34	1.11	1.24	1.20
39	1.43	-	0.44
52	0.96	0.94	0.91

A selection of samples from Table 9 was made for additional analysis to investigate the correlation between tomography and metallography data and to decrease errors in density measurements. The density percentage for each sample was determined using two distinct methodologies. In Sample 16, the notable difference between tomography and metallography results can be attributed to the fact that metallography mainly investigates the surface. Fig. 49(b) illustrates that this sample exhibits significant porosity at the surface, whereas the bulk displays reduced porosity, highlighting the differences between these measurement techniques. The 3D tomography images depicted in Fig. 49(a) illustrate the distribution, morphology, and dimensions of the pores. In denser samples, such as Sample 52, the results from both methods converge more closely due to the reduced porosity, resulting in a minimal disparity between the methods.

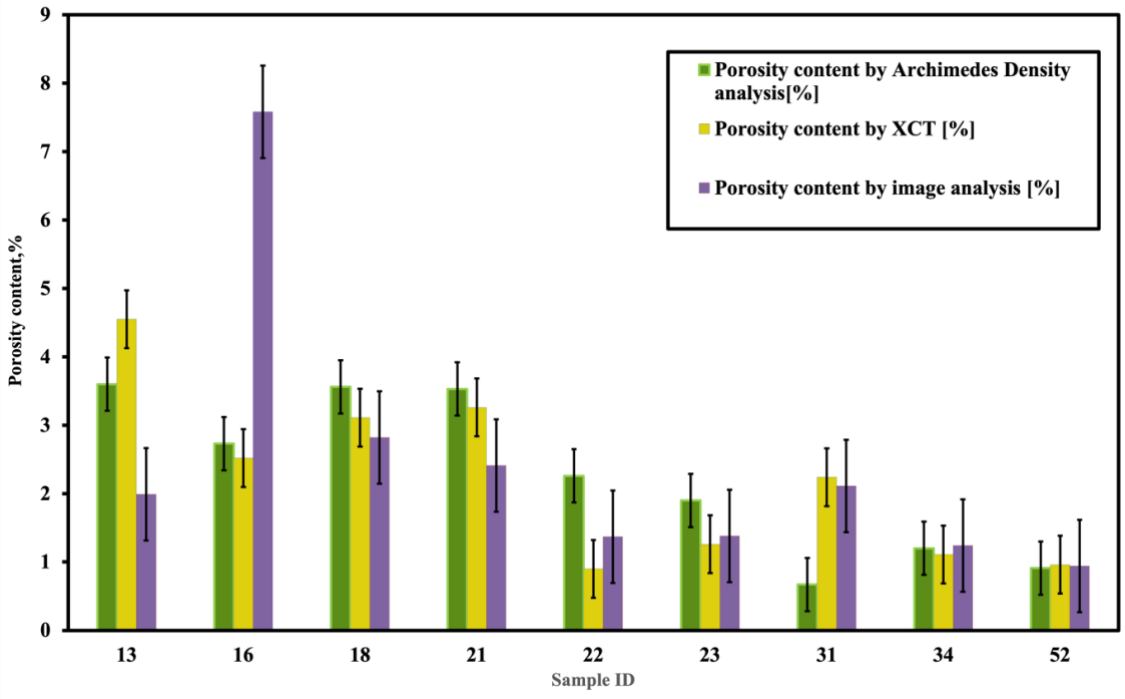

Fig. 48. Porosity percentage chart displaying the results after applying standard error to the data in Table 9

Furthermore, after applying the standard deviation to all data in Table 9, the porosity percentage chart is illustrated in Fig. 49. The analysis concentrated exclusively on the Archimedes method applied to all 64 samples. The purpose of this analysis was to determine the closeness of the data using the Archimedes method to achieve a precise comprehension of its accuracy.

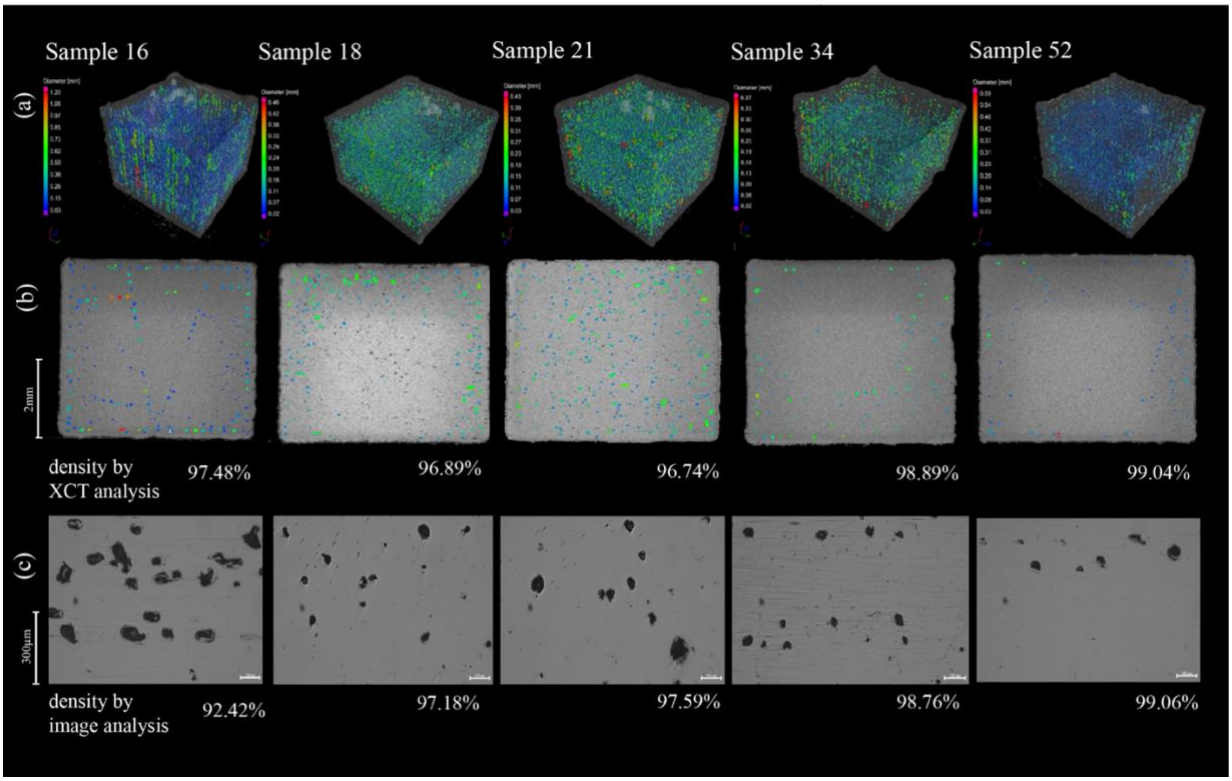

Fig. 49. Representation of a thorough analysis of the samples employing various density measurement techniques. (a) presents the 3D tomography, providing a comprehensive visualization of the sample structure, with each sample measuring 8 × 8 × 8 mm. (b) emphasizes the frontal perspective of the samples, displaying particular internal characteristics via tomography imaging. (c) presents metallographic images acquired through OM, comprehensively analyzing the sample's structure. Furthermore, the density values of the samples, obtained through XCT and image analysis techniques, are presented for comparison.

Fig. 50 illustrates the impact of process parameters on the relative density of parts as it varies with the volumetric energy density (VED). The laser power is shown by the size of the points, while the hatch distance and scan speed are indicated by the color in Fig. 50a and Fig. 50b, respectively. The Volumetric Energy Density (VED) varies from 33 to 283 (J/mm³), leading to component densities ranging from 90.9% to 99.9%. Sample 38 exhibited the highest density, measuring 99.9%, along with a corresponding Volumetric Energy Density (VED) of 66 J/mm³. Inadequate laser energy at lower VED values results in partial fusion, which reduces the components density. Nevertheless, if the Volumetric Energy Density (VED) exceeds 50 J/mm³, the L-PBF process produces components with a high level of density, as confirmed by optical micrographs as shown in Fig. 50. As VED grows, a decrease in density occurs because of keyhole formation, which highlights the significance of vaporization effects within high range of VED. Therefore, both extremely low and extremely high values of VED are

inappropriate generally for creating a totally dense component. Therefore, As the VED changes, different types of porosities can be observed.

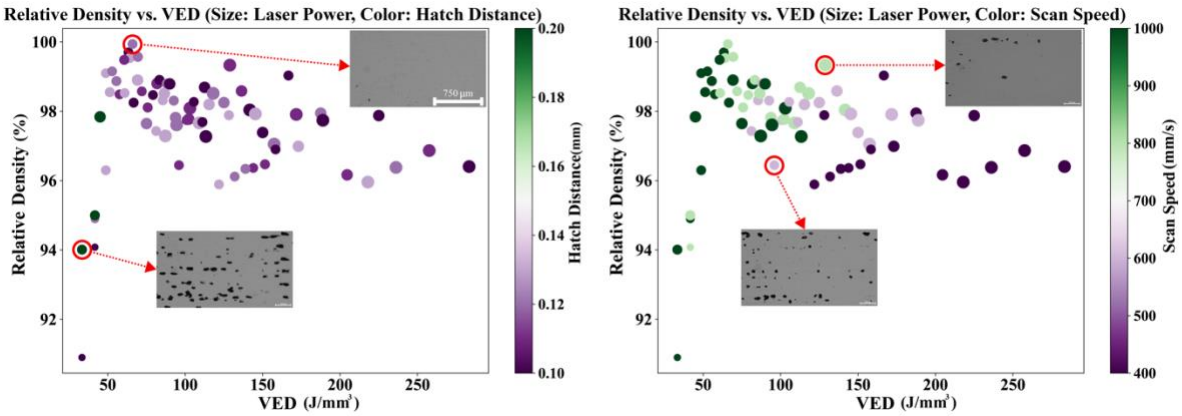

Fig. 50. Illustration of the relationship between the calculated Volumetric Energy Density (VED) and the relative Archimedes density. The size of the points represents laser power, while color indicates (a) scan speed and (b) hatch distance.

4.3. Hyperparameter Tuning

Various ML models were utilized on the data, assessing their impact to identify the most accurate and optimal model for process parameter optimization. Supervised learning is a prominent ML approach that employs labeled data segmented into training and testing sets, primarily to develope models that identify relationships between predictors (features) and the response (target) within the dataset. A systematic approach was employed for hyperparameter tuning to enhance the performance of the ML models. Rather than exploring an excessively wide range of hyperparameters, which can be computationally expensive, shorter ranges were initially defined for almost all hyperparameters of each model. This approach allowed the key hyperparameters with the most significant impact on model accuracy, as indicated by the coefficient of determination (R^2), to be identified. However, it should be noted that if inappropriate ranges for hyperparameters are defined, inaccurate correlation heatmaps may result, potentially leading to the selection of wrong hyperparameter values. This highlights the importance of carefully selecting parameter ranges to ensure reliable tuning outcomes.

A correlation heatmap was generated to visualize the relationship between each hyperparameter and the R^2 score. Fig. 51, displays the heatmap showing the relationship between each hyperparameter and the R^2 score, visually representing the correlations between the algorithms and the predictive accuracy. This analysis identified the top three most influential hyperparameters. Subsequently, the hyperparameters were evaluated more comprehensively using more comprehensive ranges and smaller step sizes. In the next step, a 3D plot was used to examine the effect of the two most impactful hyperparameters on prediction accuracy, those which are highlighted with red rectangles in Fig. 51, allowing for the identification of their optimal values, as shown in Fig. 52.

4.3.1. Heat map correlation plot

To find the effect of each hyperparameter for each algorithm, a heat map correlation plot was created, as illustrated in Fig. 51. To find the optimal value for each hyperparameter, heat maps were utilized to show the effect of each parameter on the R^2 score. The most effective hyperparameters were highlighted by red and blue rectangles, indicating the parameters with the maximum impact. As mentioned before, the hyperparameters highlighted by red rectangles were selected to use in the 3D plot, while the third hyperparameters, highlighted by blue rectangles analyzed by a 2D plot. The aim of selecting these three hyperparameters for further analysis is to find the optimal value which corresponds to the lowest error in each model. For example, in the case of the RFR model, parameters such as min_samples_leaf, min_weight_fraction_leaf, and n_estimators as suggested by correlation heatmap were analysed. After identifying the two most influential hyperparameters (min_samples_leaf and min_weight_fraction_leaf), a 3D plot was generated to visualize how their interaction affected the R^2 score. The optimal values for these parameters were then fixed, and the third hyperparameter (n_estimators) was fine-tuned to further enhance the model performance. It is worth noting that Fig. 51, Fig. 52, and Fig. 53 are related to the analysis of the models using a training size of 80%.

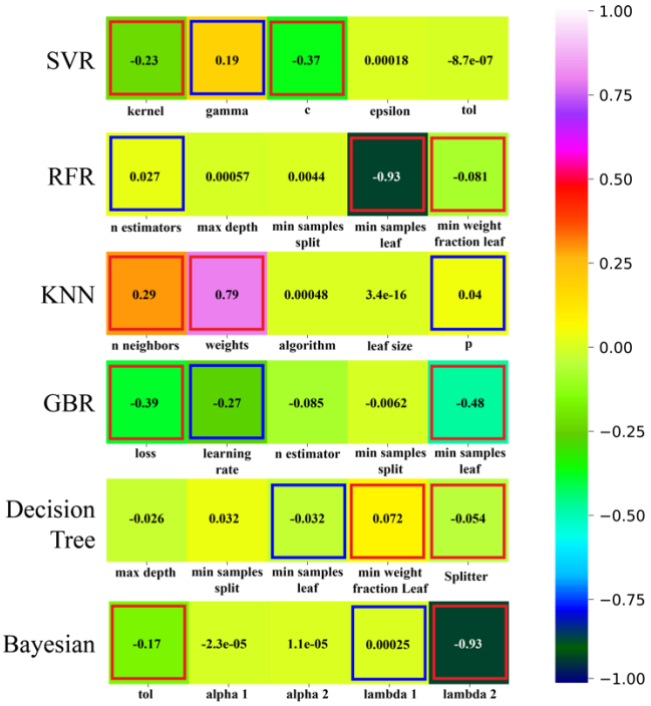

Fig. 51. Correlation heatmap of hyperparameters and R^2 for all algorithms (Training Size 80%)

4.3.2. First and second hyperparameter analysis - 3D plot surface

After identifying the three most effective hyperparameters, a 3D plot is created using the first and second hyperparameters (highlighting with red rectangles in Fig. 51) chosen in the previous step. This process aims to find the optimized hyperparameter values leading to the maximum R^2, indicating the minimal error, for each model, see Fig. 52. Following this step, only one hyperparameter remains unassigned a value. In the subsequent phase, a 2D plot is employed to

ascertain the optimal value for the third hyperparameter by analyzing the minimal errors which will be explained in the next section.

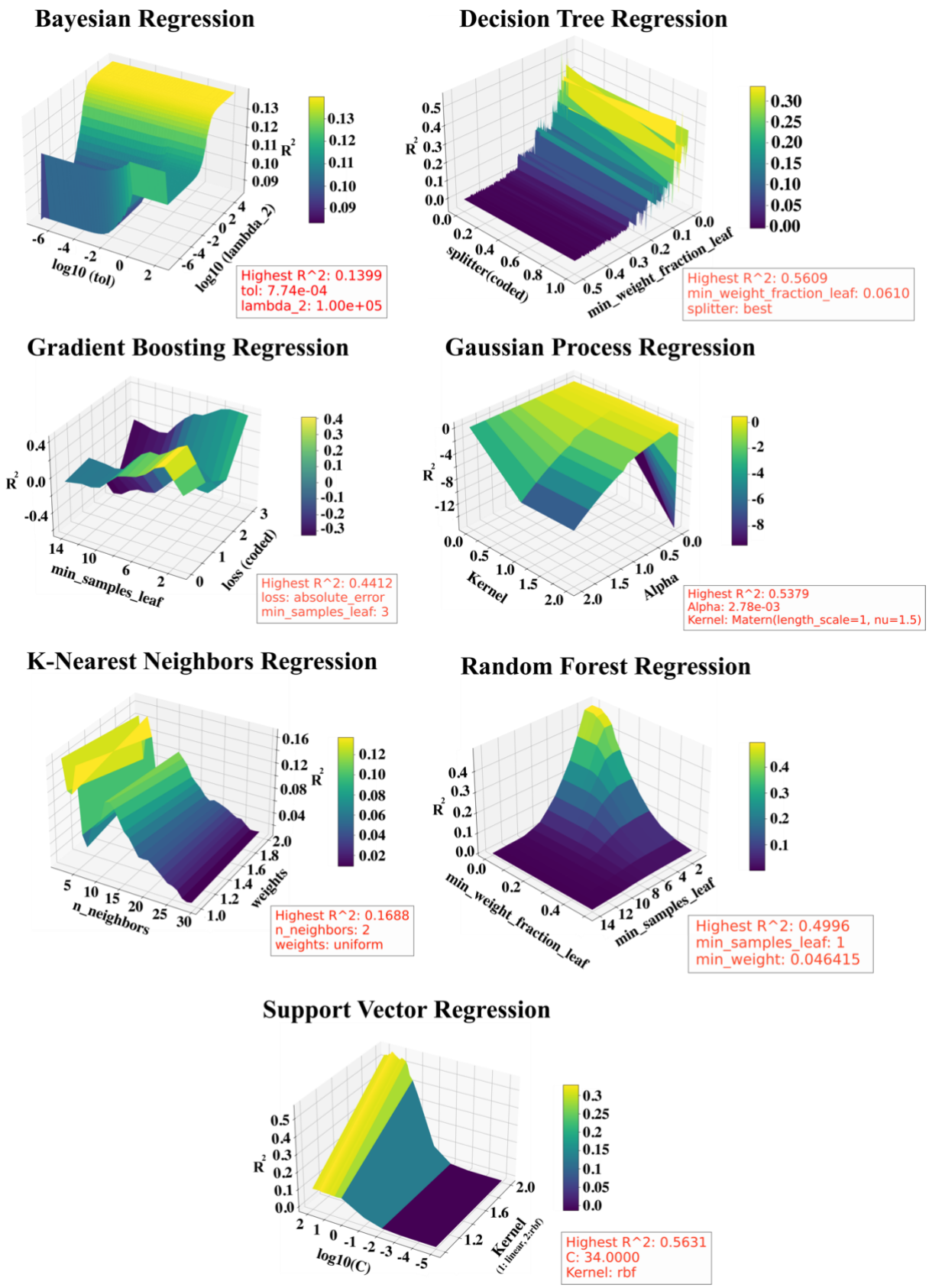

Fig. 52. 3D plots illustrating the optimal hyperparameter values for achieving the maximum R^2 score (minimum error) for various ML models .

4.3.3. Third hyperparameter analysis - 2D plot

In this step, to identify the optimal value for the third hyperparameter a 2D plot was used for each algorithm in all training sizes as depicted in Fig. 53. The optimized value for the third hyperparameter is determined by the criterion that an elevated R^2 and lowered MSE and MAE signify superior model performance with minimized error. This step represents the last stage of hyperparameter selection, wherein values for all hyperparameters have been established for each model. The next step is to investigate the error rates of the various models.

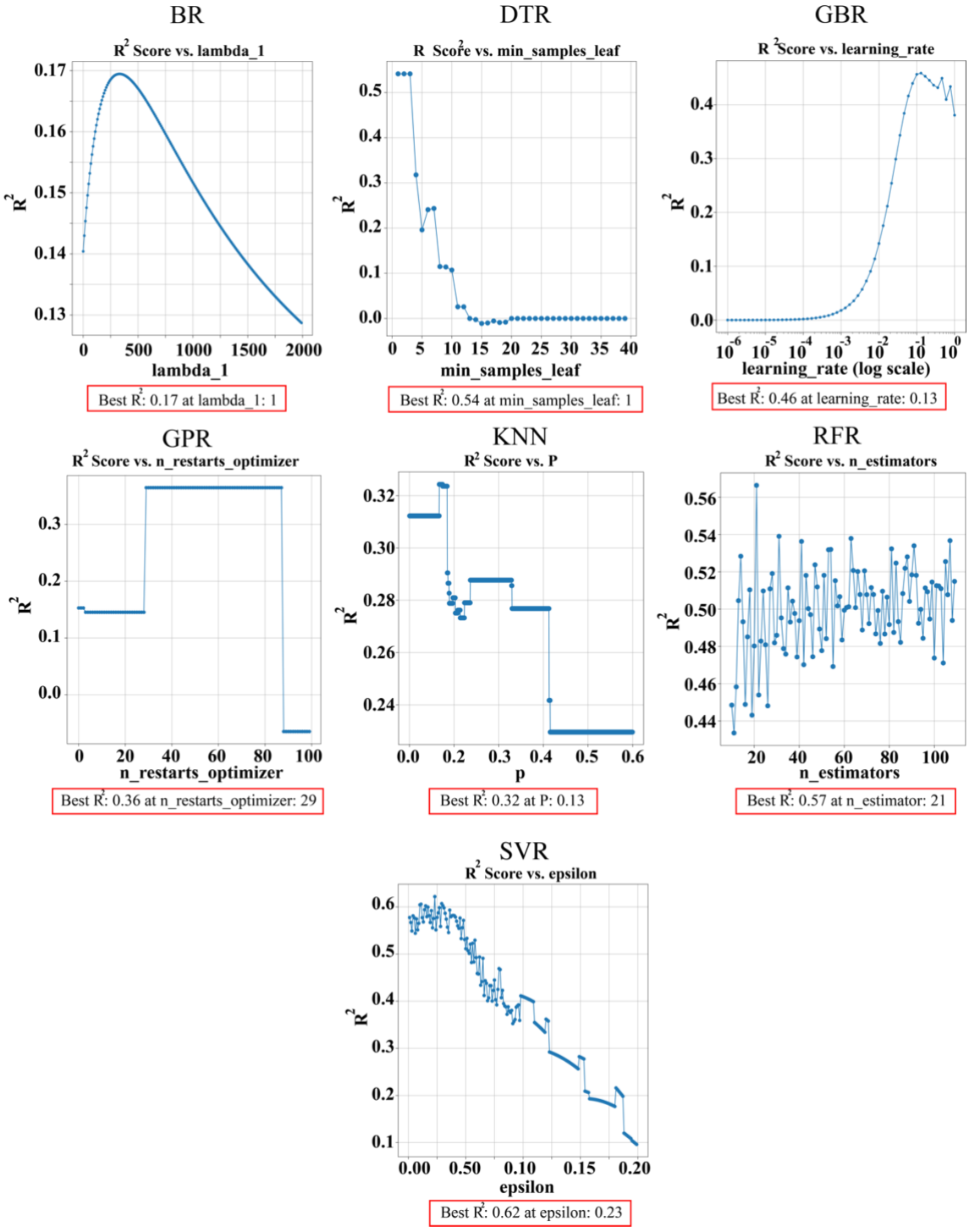

Fig. 53. 2D plots showing the optimal value selection for the third hyperparameter based on three error metrics including R^2, MSE, and MAE for various ML models

In the SVR model, although the gamma parameter showed a stronger correlation in the heatmap plot (Fig. 51) compared to epsilon, it only has two possible values. As a result, a 2D plot analyzing this hyperparameter would not provide sufficient insight. Consequently, as is shown in Fig. 53, the epsilon parameter was selected for analysis in the 2D plot due to its more comprehensive range of values. However, both gamma values were tested during the tuning process to ensure a thorough evaluation.

This tuning process significantly improved the prediction accuracy in all models, ensuring that the selected hyperparameters yielded optimal results. The final hyperparameter values were then used in subsequent model evaluations, including comparisons of predicted versus actual values for model validation.

4.3.4. Train size effect analysis

After completing the hyperparameter tuning process and selecting the optimized hyperparameters, we used these values in the ML algorithms to predict the target variable (the relative density of the testing data) for which the actual values were already known. The efficiency of each model was subsequently assessed by quantifying the differences between the predicted and actual values. The impact of different train sizes on model performance, assessed through R2, MAE, and MSE, is an essential part of model evaluation and optimization. Fig. 54 depicts the impact of various train sizes (40%, 50%, 60%, 70%, 80%, 90%) on the aforementioned error metrics across several algorithms: BR, DTR, GBR, GPR, K-Nearest Neighbors (KNN), SVR, and RFR. The general trend observed in Fig. 54a indicates that as the training size percentage increases, the Mean Squared Error (MSE) generally tends to rise in most algorithms, which inversely affects prediction accuracy. This increase in MSE is more noticeable in the BR. For instance, at the training size of 40%, the BR demonstrates a mean squared error (MSE) of 1.987, which increased to 7.043 by raising the training size to 90%. The significant rise in MSE highlights the model's sensitivity to decreased testing size, leading to lower prediction efficiency. However, some algorithms, such as SVR, demonstrate the inverse trend, where an increase in training size decreases the MSE, indicating enhanced predictive accuracy with larger datasets.

The effect of train size on Mean Absolute Error (MAE), as shown in Fig. 54b, follows a similar pattern to that of MSE. The lowest MAE values are typically observed at the 60% training size, while larger training sizes of 90% result in higher MAE values. For example, in the GBR model, the MAE at 60% train size is 0.713, but this value rises to 0.896 at 90%. While this suggests that a 60% train size may yield optimal results for minimizing MAE, it is important to note that other error metrics, such as MSE and R^2, must also be considered to identify the most appropriate train size for overall model performance.

Fig. 54c shows that the coefficient of determination (R^2) increases as the training size rises, indicating improved predictive accuracy. The most significant improvements in R^2 occur when the training size reaches 80% and 90%. For instance, in the GPR model, the R^2 value starts at 0.252 with a 40% training size but more than triples to 0.856 when the training size reaches 90%. Similarly, the SVR model significantly improves, with the R^2 increasing from 0.344 at a 40% train size to 0.842 and 0.871 at 80% and 90%, respectively. However, this trend is not

consistent across all algorithms. In the BR, an opposite pattern is observed, where increasing the training size leads to a decrease in R^2, highlighting the distinct behavior of each algorithm. Although using 90% of the data for training usually results in the highest R^2 score across various algorithms, using only 10% of the data for testing leads to an increase in MAE and MSE. This shows that considering only R^2 is not enough to evaluate the prediction accuracy of each model, and other error metrics should also be considered.

The results indicate that a training size of 80% achieves an optimal balance between three different error metrics, depending on the algorithm applied. Among the analyzed algorithms, SVR provides the highest accuracy in almost all training sizes, while the BR displays the lowest prediction efficiency throughout the evaluation. These findings highlight the necessity of choosing a proper training size and optimal hyperparameters to optimize accuracy and error metrics for each algorithm.

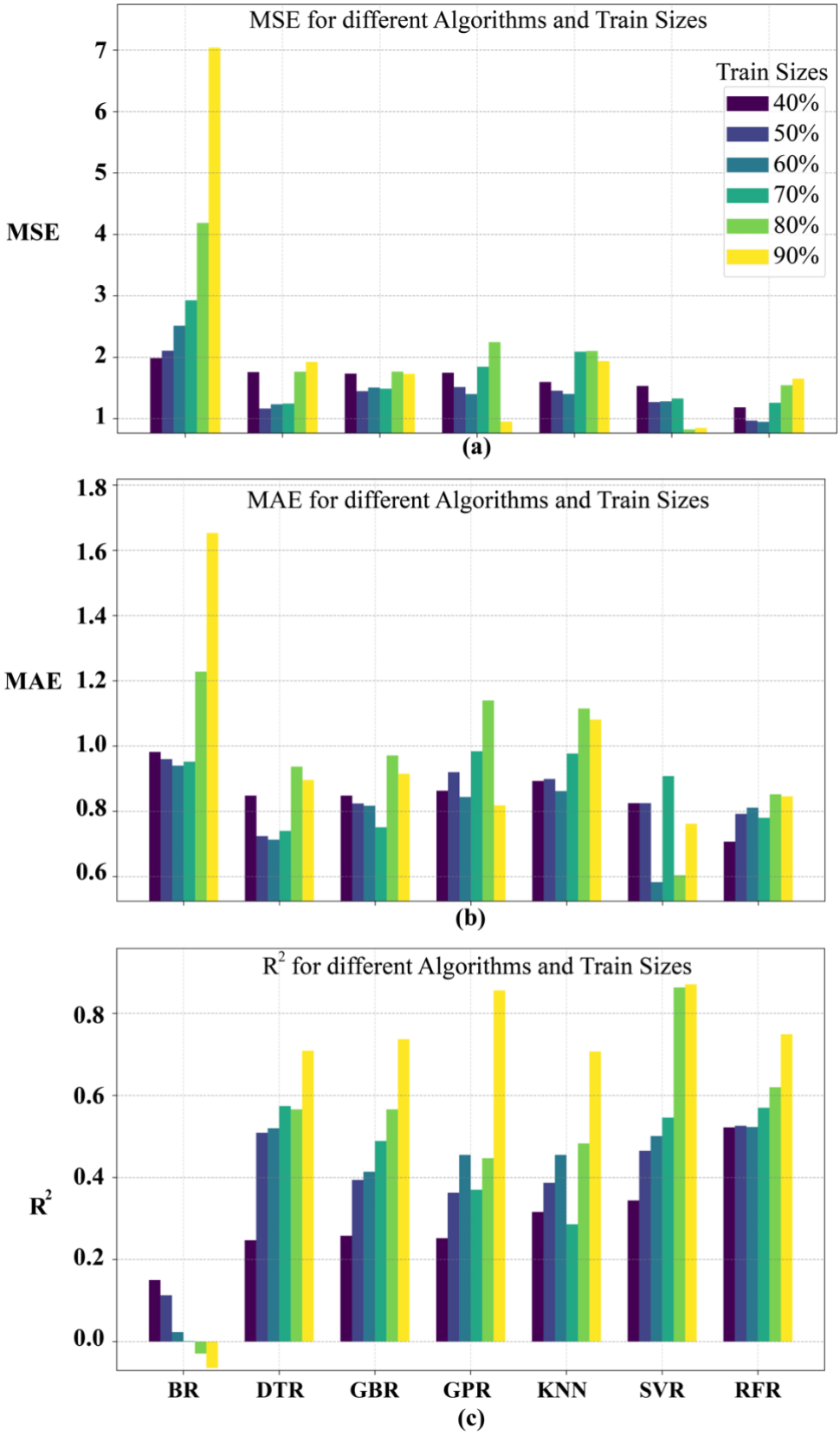

Fig. 54. R^2, MAE, and MSE values for different values and train sizes of each ML algorithms

4.3.5. Predicted vs. Actual Density Comparison

This section evaluates the predictive accuracy of various algorithms by comparing the predicted and actual relative densities on the vertical and horizontal axes, respectively. Fig. 55 illustrates the comparison of the actual and predicted relative densities in AISI 316L-2.5% Cu components manufactured by L-PBF for all methods at 80% training size. The proximity of the points to the red dashed line, representing perfect predictions, indicates the accuracy of each model. The shaded gray area shows ±1% tolerance range, indicating an acceptable range for prediction deviations. Most models are less accurate in components with lower relative densities, except for SVR and GPR, which consistently maintain high precision across the entire range. For components with higher relative density, prediction accuracy improves in all models, as shown by the closer alignment of points with the red line.

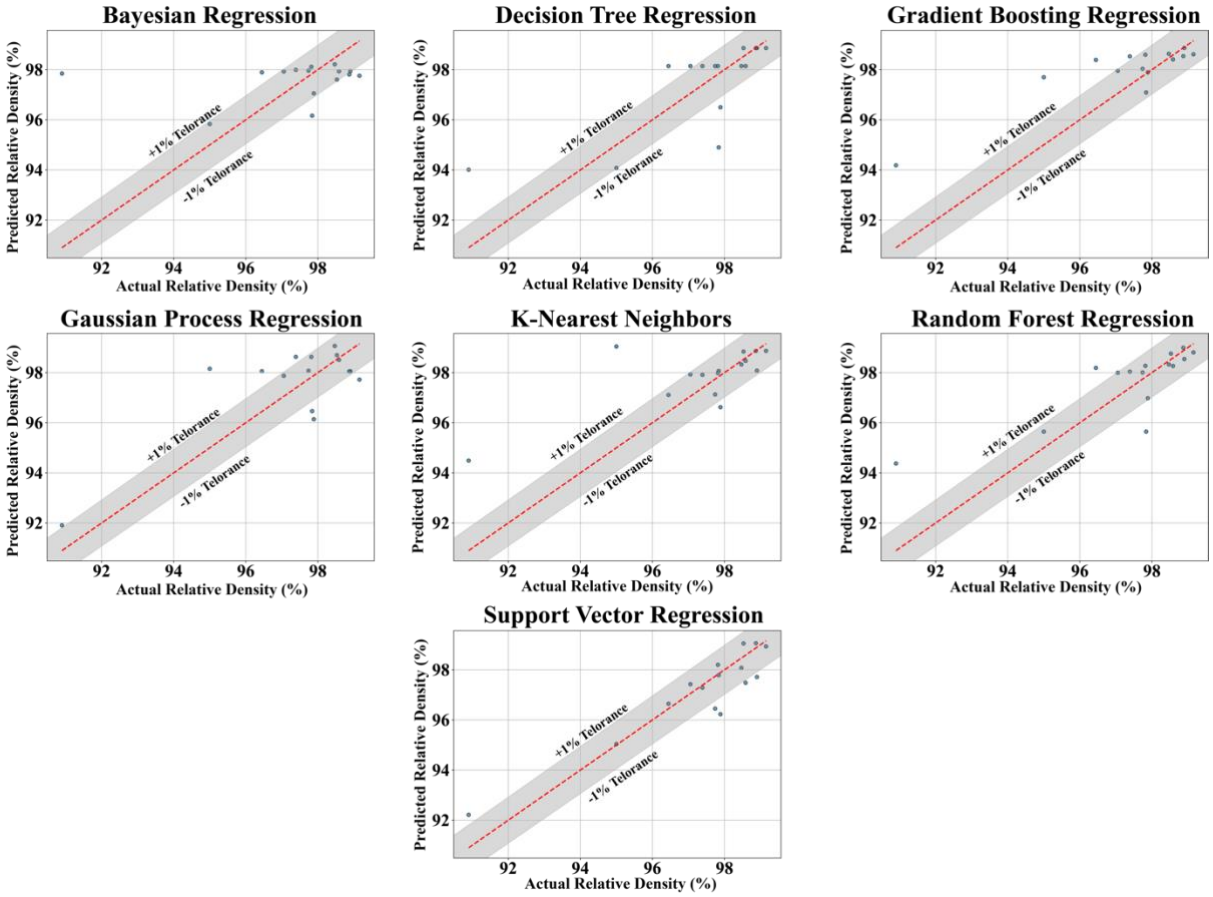

Fig. 55. Predicted density versus actual density plots with regression applied for each ML model, illustrating the performance of the selected hyperparameters.

4.4. Final Model Selection and verification

Following the assessment of the models, the best ML algorithm for density prediction was identified. Fig. 56 compares the actual and predicted relative densities attained by the best machine-learning model using testing data. The SVR algorithm with the optimized hyperparameters (kernel = rbf, C = 215.44, Max_iter = 990, tol = 0.0278, epsilon = 0.1) was applied to predict relative densities at 15 testing points. Among the models, SVR excelled,

attaining the lowest MAE of 0.601, MSE of 0.640, and highest R^2 of 0.842 at the training size of 80%. As shown in Fig. 56, the predictions closely match the actual values. Additionally, Fig. 56 highlights the optimal values of the target variable (relative density), the corresponding VED, and the same trend shown in Fig. 50 for manufacturing under optimal conditions. additionally, the optimized process parameters for the target density can be predicted using the most accurate model, reducing powder usage for printing and saving time and cost. Supplementary advantages encompass enhanced efficiency and diminished material waste in production, thereby fostering more sustainable and economically viable manufacturing.

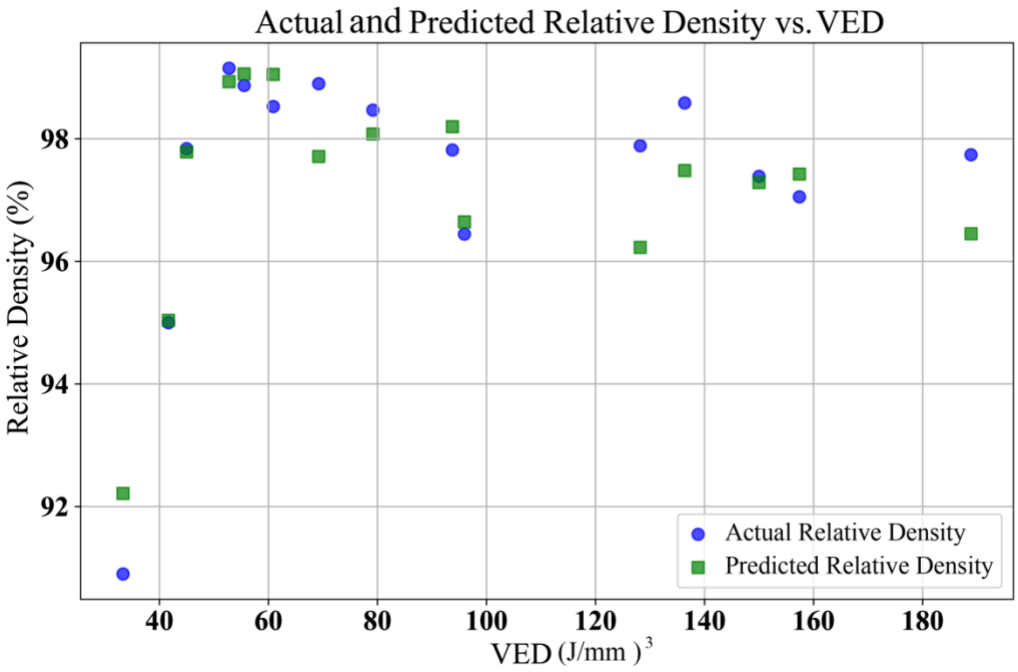

Fig. 56. Comparison of actual and predicted relative Archimedes density as a function of calculated VED using SVR with optimized hyperparameters at the training size of 80%

4.5. Optimized Process Parameters Map

Fig. 57 illustrates the predicted relative density for four different scan speeds: 400, 600, 800, and 1000 mm/s based on the best predictor model, SVR at the training size of 80% with specific optimized hyperparameters. These values are within the specified range of hatch distance (0.1 to 0.2 mm) and power (100 to 400 W). Generally, as the scan speed increases, the contour plots in Fig. 57 indicate a continuous rise in predicted relative density, as shown by the expansion of yellow and green regions. This trend highlights the influence of scan speed on the relative density, where higher scanning speeds caused enhanced relative density under the given conditions.

At a scanning speed of 400 mm/s, the minimum relative densities are observed in the power range of 300 to 400 W, independent of the hatch distance. Conversely, the highest relative densities at this scan speed are obtained when the power ranges from 100 to 200 W, with the hatch distance between 0.13 and 0.15 mm. This suggests that optimal relative density at the

scan speed of 400 mm/s can be achieved within these specific process parameters at lower power levels combined with moderate hatch distances.

At a scanning speed of 600 mm/s, the predicted relative density improved across the entire hatch distance and power range compared to the previous scan speed. However, the maximum predicted relative density is still lower at scanning speeds of 800 and 1000 mm/s. The lowest relative density is observed when the power exceeds 300 W, particularly at hatch distances less than 0.12 mm. On the other hand, when the power is less than 300 W, the highest relative densities are achieved in two specific hatch distance ranges, 0.10 to 0.11 m, and 0.15 to 0.18 mm.

The maximum predicted relative density at a scan speed of 800 mm/s increased by 0.8% compared to the previous scan speed of 600 mm/s, and by 1.1% compared to the speed of 400 mm/s, reaching a peak of 99.5%. The highest relative densities were achieved in the hatch distance range of 0.12 to 0.18 mm. However, at high P values, particularly around 400 W, the highest percentage of porosity would be possible, especially in small hatch distance ranges.

At the scanning speed of 1000 mm/s, the maximum relative density decreased by 0.5%. The predicted relative density value reached its lowest value at the hatch distance range of less than 0.12 mm. For hatch distances greater than 0.12 mm, the power should be set between 100 and 250 W to achieve high relative density, particularly at a hatch distance of 0.14 mm.

Based on Fig. 57, it can be concluded that while high relative density values are achievable in all four plots, a scanning speed of 800 mm/s can be considered the optimal value. At this scanning speed, porosities can be further minimized using a power setting of approximately 250 W and a hatch distance of 0.13 mm.

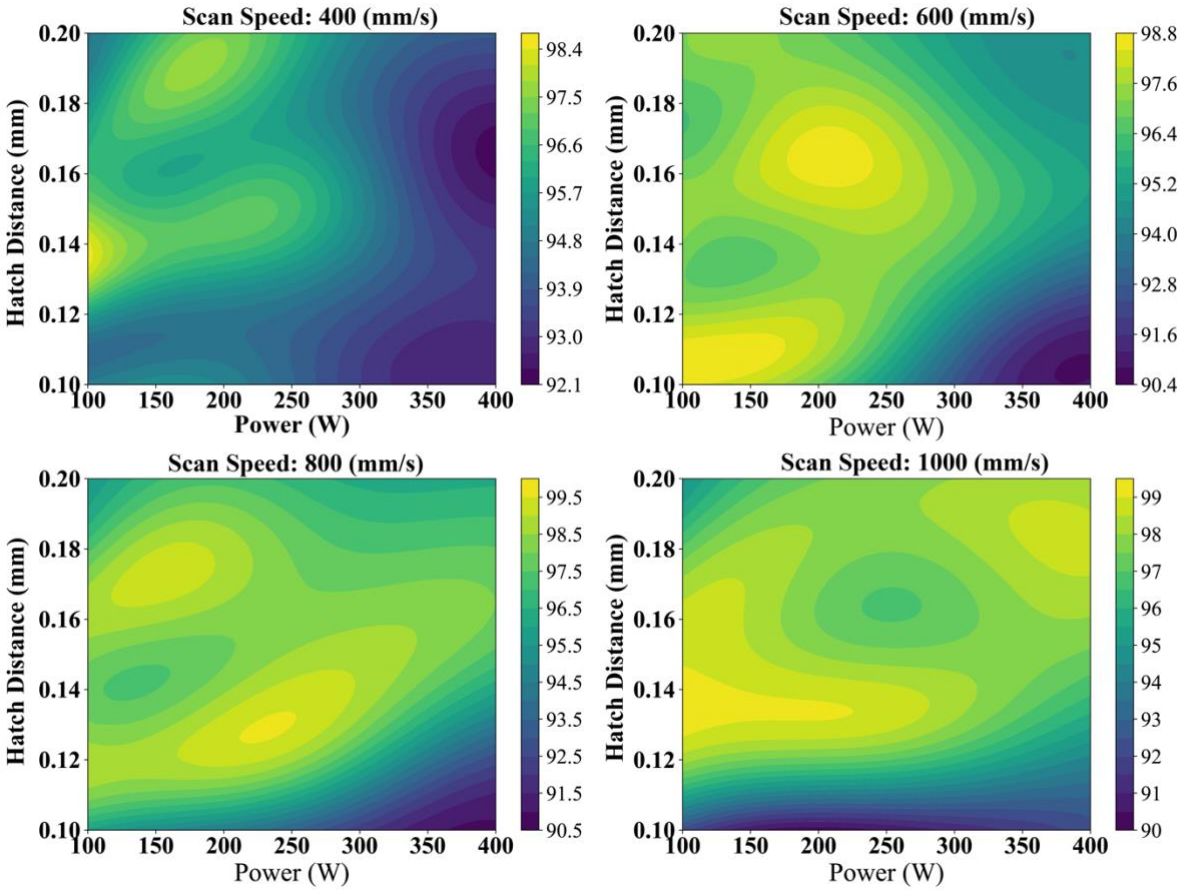

Fig. 57. Illustration of predicted relative density (%) for different scan speeds (400, 600, 800, and 1000 mm/s) by varying power (100-400 W) and hatch distance (0.1-0.2 mm) ranges, using the SVR algorithm at the training size of 80% after hyperparameter tuning

5. Conclusion and Future Perspective

In the future, 3D printing is expected to become more diverse and application-focused in terms of materials, departing from traditional perspectives. This shift is driven by increased willingness and the availability of a broader range of materials. Industries, such as aerospace and automotive, are increasingly turning to 3D printing to develop materials that meet their specific needs. Designers can now choose materials specifically tailored to their applications to evaluate printability, complexity, time, cost, raw materials, model size, and geometry for prototypes or manufacturing. To address this, GA and genetics-based ML methods optimize these multi-indicators and minimize complexity. GA is preferred due to its ability to handle extensive data in binary string format [190].

As discussed in this review, addressing the challenges of applying ML algorithms in AM involves overcoming limitations related to specific machines, materials, and process parameters. A crucial research gap is the need to generalize these ML models to broader contexts, necessitating further investigation. Additionally, even though the data used in these algorithms is often voluminous, it may prove insufficient. Various sensors on AM machines can be combined to improve defect detection and accuracy for monitoring goals, yet this introduces new challenges. Handling diverse and high-volume sensor data requires the development of novel ML algorithms. Consequently, the following research directions are proposed to enhance the use of ML techniques for real-time monitoring and control of AM processes.

5.1. Sensor Development

To ensure timely corrective actions are taken in AM, it is essential to have a prompt response when employing the ML model for real-time control [22]. As a solution, it has been proposed to create an intelligent sensor that can leverage "Big Data" analytics and facilitate AM integration into the Industry 4.0 framework [191]. Moreover, computational tools and algorithms are essential for operating newly developing sensing platforms. These tools enable the platforms to perform better than earlier sensor technologies in terms of cost, resolution, size, and sensitivity, among other factors [191]. Furthermore, it is important to emphasize that the benefits are reciprocal (Fig. 58); using ML algorithms can enable an iterative design process that rectifies inconsistencies in prototype sensors as they transfer to large-scale manufacture [192], further paving toward acquiring high-quality data.

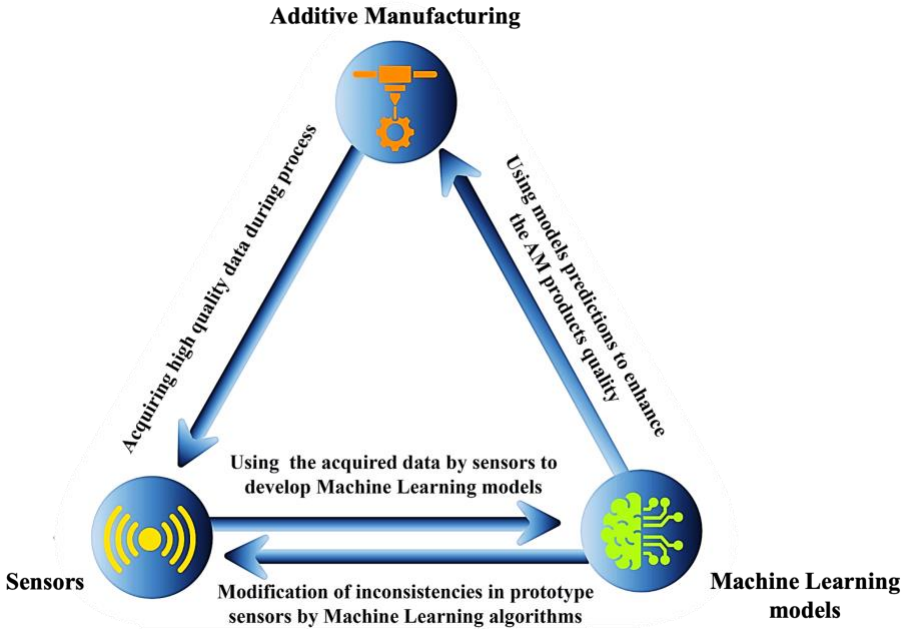

Fig. 58. The mutual benefits sensors and ML models may offer to enhance the quality of metal AM.

5.2. Volume, Velocity, and Variety of Data

Although ML methods have undergone significant development over the years, their application to online monitoring is a relatively new area that requires further exploration. Given the rapid pace of the AM process, the data collected exhibits characteristics typical of "Big Data" in terms of volume, velocity, and variety [193]. The research articles reviewed in this study indicate that supervised ML methods are the most employed approach for real-time monitoring and control of L-PBF. Consequently, it is anticipated that labeling and training such a substantial volume of data can be both cumbersome and labor-intensive [140]. To mitigate the time required for data training, an alternative approach involves the utilization of different ML methodologies, such as unsupervised and active learning techniques, which are likely to gain more traction. This approach could lead to shorter training periods and allow faster response times [193].

Another promising avenue for research lies in the domain of UQ, a crucial element for ensuring the reliability of robust designs. The assessment of uncertainty in the AM sector has been thoroughly examined by Wang et al. [194]. In the context of regression tasks, ML models such as GPR not only furnish the predicted mean value of output at a given input but also supply a standard deviation, which indicates the associated uncertainty at that particular input point. Furthermore, in classification tasks, ML models also offer a measure of confidence in their classification decisions.

5.3. Conclusion

Optimization of the critical process parameters of the L-PBF process using ML approaches to improve component density and quality and enhancing the building rate were two main goals of this thesis. An optimal process parameter ranges for improving process performance were identified through a comprehensive analysis of the effects of laser power, scan speed, and hatch distance on relative density. The results from the ML models, combined with experimental

data, provide valuable insights into how variations in process parameters affect the densification of LPBF components. This research validates the effectiveness of ML in enhancing AM processes and highlights the significance of data-driven methodologies in advancing the field.

In the second chapter, state of the art, an in-depth overview of the current research on ML in laser-based AM processes such as L-PBF and DED was provided. It examines the key issues, focusing on application case studies, methodologies, and model development. Furthermore, the application of ML in these fields was studied in several phases, including processing parameters optimization and property prediction, geometric deviation control, defect detection, and in-situ monitoring. Conducting a thorough review of the current literature on the applications of ML in L-PBF and DED reveals that researchers are exploring innovative approaches, including data-driven techniques, to address time and cost-related issues.

The third Chapter, Materials and Methods, explained the methodology employed throughout the study, highlighting the selection of process parameters, the manufacturing process, different methods for measuring sample densities, and the subsequent ML optimization. It outlines each step taken to ensure accurate and reliable results, focusing on optimizing process parameters to improve the quality of LPBF components.

In the fourth chapter, titled Results and Discussion, components density, porosity percentage of each sample, and the ML methodology used to optimize the LPBF process parameters were described. The dataset, consisting of density measurements, was split into various training and testing sets. Seven ML algorithms including BR, DTR, GBR, GPR, KNN, RFR, and SVR were evaluated for their predictive accuracy. Given the importance of hyperparameters in optimizing model performance, each algorithm underwent extensive hyperparameter tuning using Grid Search. A correlation heatmap was generated to evaluate the relationship between hyperparameters and prediction accuracy, identifying the three most influential hyperparameters for further analysis. Finally based on the prediction of the best ML algorithm, The SVR algorithm with the optimized hyperparameters (kernel = rbf, C = 215.44, Max_iter = 990, tol = 0.0278, epsilon = 0.1), the optimized process parameter for L-PBF process was defined.

According to the research conducted on the process parameter optimization in L-PBF using ML, the following outcomes can be drawn:

1. Trial and error is not an ideal approach for improving the quality of parts in AM due to the high cost associated with feedstock and machines as well as the rapidly changing economic landscape characterized by the quick creation of new products. On the other hand, producing high-quality goods from 3D designs created in virtual environments requires a new predictive paradigm, further necessitating the application of data-driven methods.

2. ML models can predict the product component density, microstructural properties, and mechanical behavior of manufactured parts with minimal error. Moreover, geometric

deviation control can be conducted with ML-assisted methods to enhance the efficiency of powder-based AM methods and facilitate increased utilization in practical manufacturing processes.

3. Among the seven evaluated ML models, SVR algorithm outperformed others with the highest prediction accuracy in optimizing process parameters, achieving an R^2 score of 0.842, MAE of 0.601, and MSE of 0.640.

4. Extensive hyperparameter tuning using Grid Search led to optimized settings for each algorithm, revealing that fine-tuning of hyperparameters including C, kernel, and tol in SVR had the most significant impact on model accuracy and process optimization.

5. A strong correlation was observed between the key process parameters—laser power, scan speed, and hatch distance—and the relative density of the components. The optimized process parameters significantly improved the relative density of the components, reaching values close to or above 99%, indicating a successful reduction in porosity.

6. The optimized process parameters for L-PBF using SVR with hyperparameter tuning were determined to be laser power = 200 - 250 W, scan speed = 800 mm/s, and hatch distance = 0.13 mm, significantly enhancing the component relative density.

7. The application of ML techniques not only predicted a reliable process parameters defect content relationship but also led to an enhancement in the building rate, thus addressing both quality and productivity in the L-PBF process. The ML models developed can be applied to other AM processes or materials, demonstrating the versatility of data-driven optimization approaches in AM.

It is noteworthy that ML alone cannot address every problem. It is crucial to identify the specific conditions and contexts in which ML is advantageous and select the appropriate algorithm to address the issue. Although there are many promising applications, using ML to improve the production process of L-PBF and DED still faces numerous challenges. Overcoming these obstacles will require further inv

8. References

1. Saboori A, Aversa A, Marchese G, Biamino S, Lombardi M, Fino P. Application of directed energy deposition-based additive manufacturing in repair. Appl Sci. 2019;9(16):3316.
2. Rinaldi M, Ghidini T, Cecchini F, Brandao A, Nanni F. Additive layer manufacturing of poly (ether ether ketone) via FDM. Compos Part B Eng. 2018;145:162–72.
3. Mosallanejad MH, Niroumand B, Aversa A, Saboori A. In-situ alloying in laser-based additive manufacturing processes: A critical review. J Alloys Compd. 2021;872:159567.
4. Carrozza A, Marchese G, Saboori A, Bassini E, Aversa A, Bondioli F, et al. Effect of Aging and Cooling Path on the Super β-Transus Heat-Treated Ti-6Al-4V Alloy Produced via Electron Beam Melting (EBM). Vol. 15, Materials. 2022.
5. Bandekhoda MR, Mosallanejad MH, Atapour M, Iuliano L, Saboori A. Investigation on the Potential of Laser and Electron Beam Additively Manufactured Ti–6Al–4V Components for Orthopedic Applications. Met Mater Int. 2024;30(1):114–26.
6. Zhu Y, Zou J, Yang H yong. Wear performance of metal parts fabricated by selective laser melting: a literature review. J Zhejiang Univ A. 2018;19(2):95–110.
7. Liu K, Gu D, Guo M, Sun J. Effects of processing parameters on densification behavior, microstructure evolution and mechanical properties of W–Ti alloy fabricated by laser powder bed fusion. Mater Sci Eng A. 2022;829:142177.
8. Calignano F. Investigation of the accuracy and roughness in the laser powder bed fusion process. Virtual Phys Prototyp. 2018;13(2):97–104.
9. Eliasu A, Duntu SH, Hukpati KS, Amegadzie MY, Agyapong J, Tetteh F, et al. Effect of individual printing parameters on residual stress and tribological behaviour of 316L stainless steel fabricated with laser powder bed fusion (L-PBF). Int J Adv Manuf Technol. 2022;119(11):7041–61.
10. Milewski JO. Additive Manufacturing of Metals: From Fundamental Technology to Rocket Nozzles, Medical Implants, and Custom Jewelry. Addit Manuf Met. 2017;
11. Zhang M, Liu C, Shi X, Chen X, Chen C, Zuo J, et al. Residual stress, defects and grain morphology of Ti-6Al-4V alloy produced by ultrasonic impact treatment assisted selective laser melting. Appl Sci. 2016;6(11):304.
12. Ansarian I, Taghiabadi R, Amini S, Mosallanejad MH, Iuliano L, Saboori A. Improvement of Surface Mechanical and Tribological Characteristics of L-PBF Processed Commercially Pure Titanium through Ultrasonic Impact Treatment. Acta Metall Sin (English Lett [Internet]. 2024;37(6):1034–46. Available from: https://doi.org/10.1007/s40195-024-01696-y
13. Patel S, Vlasea M. Melting modes in laser powder bed fusion. Materialia. 2020;9:100591.
14. Oliveira JP, LaLonde AD, Ma J. Processing parameters in laser powder bed fusion metal additive manufacturing. Mater Des. 2020;193:108762.
15. Marrey M, Malekipour E, El-Mounayri H, Faierson EJ. A framework for optimizing process parameters in powder bed fusion (PBF) process using artificial neural network

(ANN). Procedia Manuf. 2019;34:505–15.
16. Rankouhi B, Jahani S, Pfefferkorn FE, Thoma DJ. Compositional grading of a 316L-Cu multi-material part using machine learning for the determination of selective laser melting process parameters. Addit Manuf [Internet]. 2021;38:101836. Available from: https://www.sciencedirect.com/science/article/pii/S2214860421000014
17. Gu Z, Sharma S, Riley DA, Pantawane M V, Joshi SS, Fu S, et al. A universal predictor-based machine learning model for optimal process maps in laser powder bed fusion process. J Intell Manuf. 2023;34(8):3341–63.
18. Johnson NS, Vulimiri PS, To AC, Zhang X, Brice CA, Kappes BB, et al. Invited review: Machine learning for materials developments in metals additive manufacturing. Addit Manuf. 2020;36.
19. DebRoy T, Wei HL, Zuback JS, Mukherjee T, Elmer JW, Milewski JO, et al. Additive manufacturing of metallic components – Process, structure and properties. Prog Mater Sci. 2018 Mar;92:112–224.
20. Sarker IH. AI-Based Modeling: Techniques, Applications and Research Issues Towards Automation, Intelligent and Smart Systems. SN Computer Science, Vol. 3. 2022.
21. Liu J, Ye J, Izquierdo DS, Vinel A, Shamsaei N, Shao S. A review of machine learning techniques for process and performance optimization in laser beam powder bed fusion additive manufacturing. J Intell Manuf. 2022;
22. Qi X, Chen G, Li Y, Cheng X, Li C. Applying Neural-Network-Based Machine Learning to Additive Manufacturing: Current Applications, Challenges, and Future Perspectives. Engineering. 2019 Jul;5.
23. Gupta P, Krishna C, Rajesh R, Ananthakrishnan A, Vishnuvardhan A, Patel SS, et al. Industrial internet of things in intelligent manufacturing: a review, approaches, opportunities, open challenges, and future directions. Int J Interact Des Manuf. 2022;
24. Geron A. Handson Machine Learning with Scikitlearn, Keras & TensorFlow. o'Reiley Media. Inc, Sebatopol, CA. 2019;
25. Meng L, McWilliams B, Jarosinski W, Park HY, Jung YG, Lee J, et al. Machine Learning in Additive Manufacturing: A Review. JOM. 2020;72(6):2363–77.
26. Wang C, Tan XP, Tor SB, Lim CS. Machine learning in additive manufacturing: State-of-the-art and perspectives. Addit Manuf. 2020;36:101538.
27. Yuan B, Guss GM, Wilson AC, Hau-Riege SP, DePond PJ, McMains S, et al. Machine-Learning-Based Monitoring of Laser Powder Bed Fusion. Adv Mater Technol [Internet]. 2018 Dec 1;3(12):1800136. Available from: https://doi.org/10.1002/admt.201800136
28. Scime L, Beuth J. Anomaly detection and classification in a laser powder bed additive manufacturing process using a trained computer vision algorithm. Addit Manuf [Internet]. 2018;19:114–26. Available from: https://www.scopus.com/inward/record.uri?eid=2-s2.0-85035797198&doi=10.1016%2Fj.addma.2017.11.009&partnerID=40&md5=62bd52d55f85a18d810bae1fce2d4c5a
29. Pandiyan V, Drissi-Daoudi R, Shevchik S, Masinelli G, Le-Quang T, Logé R, et al. Semi-supervised Monitoring of Laser powder bed fusion process based on acoustic

emissions. Virtual Phys Prototyp [Internet]. 2021;16(4):481–97. Available from: https://www.scopus.com/inward/record.uri?eid=2-s2.0-85113735790&doi=10.1080%2F17452759.2021.1966166&partnerID=40&md5=a83aff3082a28ab906127eccbd4390b4
30. Era IZ, Farahani MA, Wuest T, Liu Z. Machine learning in Directed Energy Deposition (DED) additive manufacturing: A state-of-the-art review. Manuf Lett [Internet]. 2023;35:689–700. Available from: https://www.sciencedirect.com/science/article/pii/S2213846323001360
31. Li S, Chen B, Tan C, Song X. In situ identification of laser directed energy deposition condition based on acoustic emission. Opt Laser Technol [Internet]. 2024;169. Available from: https://www.scopus.com/inward/record.uri?eid=2-s2.0-85173190474&doi=10.1016%2Fj.optlastec.2023.110152&partnerID=40&md5=ef9cc115dc6243b74d94a3b089a68207
32. Zhang Z, Liu Z, Wu D. Prediction of melt pool temperature in directed energy deposition using machine learning. Addit Manuf [Internet]. 2021;37. Available from: https://www.scopus.com/inward/record.uri?eid=2-s2.0-85096384152&doi=10.1016%2Fj.addma.2020.101692&partnerID=40&md5=f7a89a8b5651477ffc388afbf2b3867f
33. Sutton RS, Barto AG. Reinforcement learning: An introduction. MIT press; 2018.
34. DebRoy T, Mukherjee T, Milewski JO, Elmer JW, Ribic B, Blecher JJ, et al. Scientific, technological and economic issues in metal printing and their solutions. Nat Mater. 2019;18(10):1026–32.
35. Bose S, Ke D, Sahasrabudhe H, Bandyopadhyay A. Additive manufacturing of biomaterials. Prog Mater Sci. 2018 Apr;93:45–111.
36. Shinde MS, Ashtankar KM. Additive manufacturing–assisted conformal cooling channels in mold manufacturing processes. Adv Mech Eng. 2017 May;9(5):1687814017699764.
37. Qi D, Yu H, Liu M, Huang H, Xu S, Xia Y, et al. Mechanical behaviors of SLM additive manufactured octet-truss and truncated-octahedron lattice structures with uniform and taper beams. Int J Mech Sci. 2019;163:105091.
38. Technologies ACF on AM, Terminology ACF on AMTSF 91 on. Standard terminology for additive manufacturing technologies. Astm International; 2012.
39. Wang Q, Zhang S, Zhang C, Wu C, Wang J, Chen J, et al. Microstructure evolution and EBSD analysis of a graded steel fabricated by laser additive manufacturing. Vacuum. 2017;141:68–81.
40. Liu ZC, Jiang Q, Li T, Dong S, Yan S, Zhang HC, et al. Environmental benefits of remanufacturing: A case study of cylinder heads remanufactured through laser cladding. J Clean Prod. 2016 Jun;133.
41. Dass A, Moridi A. State of the Art in Directed Energy Deposition: From Additive Manufacturing to Materials Design. Coatings. 2019 Jun;9:418.
42. Ahn DG. Directed Energy Deposition (DED) Process: State of the Art. Int J Precis Eng Manuf Technol. 2021 Feb;8.
43. Khanzadeh M, Chowdhury S, Tschopp M, Doude H, Marufuzzaman M, Bian L. In-Situ Monitoring of Melt Pool Images for Porosity Prediction in Directed Energy

Deposition Processes. IISE Trans. 2017 Dec;51.
44. Thompson SM, Bian L, Shamsaei N, Yadollahi A. An overview of Direct Laser Deposition for additive manufacturing; Part I: Transport phenomena, modeling and diagnostics. Addit Manuf. 2015;8:36–62.
45. Rahmati S. 10.12 - Direct Rapid Tooling. In: Hashmi S, Batalha GF, Van Tyne CJ, Yilbas BBTCMP, editors. Oxford: Elsevier; 2014. p. 303–44.
46. Elmer J, GIBBS G, CARPENTER J, COUGHLIN D, HOCHANADEL PAT, VAJA JAY, et al. Wire-Based Additive Manufacturing of Stainless Steel Components. Weld J. 2020 Jan;99:8–24.
47. Gu D, Shen Y. Balling phenomena in direct laser sintering of stainless steel powder: Metallurgical mechanisms and control methods. Mater Des. 2009;30(8):2903–10.
48. Song YU, Song BU, Jung MK, Lee C, Choi JP, Lee I. Multi-fidelity Gaussian process modeling of a thin-walled structure for laser powder bed fusion (LPBF) process window. J Manuf Process. 2024;127:107–14.
49. Abd-Elaziem W, Elkatatny S, Abd-Elaziem AE, Khedr M, Abd El-baky MA, Hassan MA, et al. On the current research progress of metallic materials fabricated by laser powder bed fusion process: a review. J Mater Res Technol. 2022;20:681–707.
50. Sames WJ, List FA, Pannala S, Dehoff RR, Babu SS. The metallurgy and processing science of metal additive manufacturing. Int Mater Rev. 2016;61(5):315–60.
51. Lannunziata E, Zapparoli N, Iuliano L, Saboori A. Effect of powder atomising route on the surface quality and mechanical performance of AISI 316L samples produced via laser powder bed fusion process. Procedia CIRP. 2023;118:688–93.
52. Mukherjee T, DebRoy T. A digital twin for rapid qualification of 3D printed metallic components. Appl Mater Today. 2019;14:59–65.
53. Donoghue J, Antonysamy AA, Martina F, Colegrove PA, Williams SW, Prangnell PB. The effectiveness of combining rolling deformation with Wire–Arc Additive Manufacture on β-grain refinement and texture modification in Ti–6Al–4V. Mater Charact [Internet]. 2016;114:103–14. Available from: https://www.sciencedirect.com/science/article/pii/S1044580316300262
54. Koike M, Greer P, Owen K, Lilly G, Murr LE, Gaytan SM, et al. Evaluation of Titanium Alloys Fabricated Using Rapid Prototyping Technologies—Electron Beam Melting and Laser Beam Melting. Vol. 4, Materials. 2011. p. 1776–92.
55. Vayssette B, Saintier N, Brugger C, Elmay M, Pessard E. Surface roughness of Ti-6Al-4V parts obtained by SLM and EBM: Effect on the High Cycle Fatigue life. Procedia Eng [Internet]. 2018;213:89–97. Available from: https://www.sciencedirect.com/science/article/pii/S1877705818302327
56. Antonysamy AA, Meyer J, Prangnell PB. Effect of build geometry on the β-grain structure and texture in additive manufacture of Ti6Al4V by selective electron beam melting. Mater Charact [Internet]. 2013;84:153–68. Available from: https://www.sciencedirect.com/science/article/pii/S1044580313002131
57. Chowdhury S, Yadaiah N, Prakash C, Ramakrishna S, Dixit S, Gupta LR, et al. Laser powder bed fusion: a state-of-the-art review of the technology, materials, properties & defects, and numerical modelling. J Mater Res Technol [Internet]. 2022;20:2109–72. Available from:

https://www.sciencedirect.com/science/article/pii/S2238785422011607
58. Ataee A, Li Y, Song G, Wen C. Metal scaffolds processed by electron beam melting for biomedical applications. In: Metallic Foam Bone. Elsevier; 2017. p. 83–110.
59. Singh S. Implant Materials and Their Processing Technologies. In: Reference Module in Materials Science and Materials Engineering. 2016.
60. Oshida Y. Bioscience and bioengineering of titanium materials. Elsevier; 2010.
61. Zhang LC, Liu Y, Li S, Hao Y. Additive Manufacturing of Titanium Alloys by Electron Beam Melting: A Review. Adv Eng Mater. 2018;20(5):1700842.
62. Gao W, Zhang Y, Ramanujan D, Ramani K, Chen Y, Williams C, et al. The Status, Challenges, and Future of Additive Manufacturing in Engineering. Comput Des. 2015 Apr;69.
63. Francois MM, Sun A, King WE, Henson NJ, Tourret D, Bronkhorst CA, et al. Modeling of additive manufacturing processes for metals: Challenges and opportunities. Curr Opin Solid State Mater Sci. 2017 Aug;21(4):198–206.
64. Zhang Y, Gao X, Katayama S. Weld appearance prediction with BP neural network improved by genetic algorithm during disk laser welding. J Manuf Syst. 2015;34:53–9.
65. Taghian M, Mosallanejad MH, Lannunziata E, Del Greco G, Iuliano L, Saboori A. Laser powder bed fusion of metallic components: Latest progress in productivity, quality, and cost perspectives. J Mater Res Technol [Internet]. 2023;27:6484–500. Available from: https://www.sciencedirect.com/science/article/pii/S2238785423028235
66. Yasa E, Kruth JP, Deckers J. Manufacturing by combining selective laser melting and selective laser erosion/laser re-melting. CIRP Ann. 2011;60(1):263–6.
67. Sarkon GK, Safaei B, Kenevisi MS, Arman S, Zeeshan Q. State-of-the-Art Review of Machine Learning Applications in Additive Manufacturing; from Design to Manufacturing and Property Control. Arch Comput Methods Eng. 2022;29(7):5663–721.
68. Learned-Miller EG. Introduction to supervised learning. I Dep Comput Sci Univ Massachusetts. 2014;3.
69. Dedeloudi A, Weaver E, Lamprou DA. Machine learning in additive manufacturing & Microfluidics for smarter and safer drug delivery systems. Int J Pharm [Internet]. 2023;636:122818. Available from: https://www.sciencedirect.com/science/article/pii/S0378517323002387
70. Singh D, Singh B. Investigating the impact of data normalization on classification performance. Appl Soft Comput. 2020;97:105524.
71. Kumar S, Gopi T, Harikeerthana N, Gupta MK, Gaur V, Krolczyk GM, et al. Machine learning techniques in additive manufacturing: a state of the art review on design, processes and production control. J Intell Manuf. 2023;34(1):21–55.
72. Parsazadeh M, Sharma S, Dahotre N. Towards the next generation of machine learning models in additive manufacturing: A review of process dependent material evolution. Prog Mater Sci. 2023;135.
73. Eshkabilov S, Ara I, Azarmi F. A comprehensive investigation on application of machine learning for optimization of process parameters of laser powder bed fusion-processed 316L stainless steel. Int J Adv Manuf Technol [Internet]. 2022;123(7):2733–

56. Available from: https://doi.org/10.1007/s00170-022-10331-y
74. Peng X, Wu S, Qian W, Bao J, Hu Y, Zhan Z, et al. The potency of defects on fatigue of additively manufactured metals. Int J Mech Sci. 2022;221:107185.
75. Caiazzo F, Caggiano A. Laser Direct Metal Deposition of 2024 Al Alloy: Trace Geometry Prediction via Machine Learning. Vol. 11, Materials. 2018.
76. Khanzadeh M, Chowdhury S, Marufuzzaman M, Tschopp M, Bian L. Porosity prediction: Supervised-learning of thermal history for direct laser deposition. J Manuf Syst. 2018 Apr 1;47:69–82.
77. Bridgelall R. Tutorial on Support Vector Machines. 2022;
78. Tripathi S, Hemachandra N. Scalable linear classifiers based on exponential loss function. In: Proceedings of the ACM India Joint International Conference on Data Science and Management of Data. 2018. p. 190–200.
79. Duchi JC. CS 229 Supplemental Lecture notes Hoeffding ' s inequality. In 2016. Available from: https://api.semanticscholar.org/CorpusID:17783865
80. Krizhevsky A, Sutskever I, Hinton GE. Imagenet classification with deep convolutional neural networks. Adv Neural Inf Process Syst. 2012;25.
81. Nguyen VM, Chau VT. Enhancing the Dynamic Stability of Pylons via Their Drag and Lift Coefficients by Finite Volume Method. Buildings. 2023;13(5):1120.
82. Saha S. A Comprehensive Guide to Convolutional Neural Networks: The ELI5 Way [Internet]. [cited 2022 Jan 11]. Available from: https://towardsdatascience.com/a-comprehensive-guide-to-convolutional-neural-networks-the-eli5-way-3bd2b1164a53
83. Fu Y, Downey ARJ, Yuan L, Zhang T, Pratt A, Balogun Y. Machine learning algorithms for defect detection in metal laser-based additive manufacturing: A review. J Manuf Process. 2022;75:693–710.
84. Michau G, Fink O. Unsupervised transfer learning for anomaly detection: Application to complementary operating condition transfer. Knowledge-Based Syst [Internet]. 2021;216:106816. Available from: https://www.sciencedirect.com/science/article/pii/S0950705121000794
85. Shi Z, Mamun A Al, Kan C, Tian W, Liu C. An LSTM-autoencoder based online side channel monitoring approach for cyber-physical attack detection in additive manufacturing. J Intell Manuf [Internet]. 2023;34(4):1815–31. Available from: https://doi.org/10.1007/s10845-021-01879-9
86. Scime L, Beuth J. Anomaly Detection and Classification in a Laser Powder Bed Additive Manufacturing Process using a Trained Computer Vision Algorithm. Addit Manuf. 2017 Nov 1;19.
87. Donegan SP, Schwalbach EJ, Groeber MA. Zoning additive manufacturing process histories using unsupervised machine learning. Mater Charact [Internet]. 2020;161:110123. Available from: https://www.sciencedirect.com/science/article/pii/S1044580318334004
88. Snell R, Tammas-Williams S, Chechik L, Lyle A, Hernández-Nava E, Boig C, et al. Methods for Rapid Pore Classification in Metal Additive Manufacturing. JOM [Internet]. 2020;72(1):101–9. Available from: https://doi.org/10.1007/s11837-019-03761-9
89. Singh A, Nowak R, Zhu J. Unlabeled data: Now it helps, now it doesn't. Adv Neural

Inf Process Syst. 2008;21.
90. Okaro IA, Jayasinghe S, Sutcliffe C, Black K, Paoletti P, Green PL. Automatic fault detection for laser powder-bed fusion using semi-supervised machine learning. Addit Manuf. 2019;27(January):42–53.
91. Van Engelen JE, Hoos HH. A survey on semi-supervised learning. Mach Learn. 2020;109(2):373–440.
92. Sutton RS. Introduction: The challenge of reinforcement learning. In: Reinforcement learning. Springer; 1992. p. 1–3.
93. Yoon J, Arik S, Pfister T. Data valuation using reinforcement learning. In: International Conference on Machine Learning. PMLR; 2020. p. 10842–51.
94. Ryo M, Rillig MC. Statistically reinforced machine learning for nonlinear patterns and variable interactions. Ecosphere. 2017;8(11):e01976.
95. Mahmoud D, Magolon M, Boer J, Elbestawi MA, Mohammadi MG. Applications of machine learning in process monitoring and controls of l-pbf additive manufacturing: A review. Appl Sci. 2021;11(24).
96. Wasmer K, Le Quang T, Meylan B, Shevchik S. In Situ Quality Monitoring in AM Using Acoustic Emission: A Reinforcement Learning Approach. J Mater Eng Perform. 2019 Feb 1;28:666–72.
97. Knaak C, Masseling L, Duong E, Abels P, Gillner A. Improving Build Quality in Laser Powder Bed Fusion Using High Dynamic Range Imaging and Model-Based Reinforcement Learning. IEEE Access. 2021 Mar 19;PP:1.
98. Zhang Y, Wu L, Guo X, Kane S, Deng Y, Jung YG, et al. Additive Manufacturing of Metallic Materials: A Review. J Mater Eng Perform [Internet]. 2018;27(1):1–13. Available from: https://doi.org/10.1007/s11665-017-2747-y
99. Frazier WE. Metal additive manufacturing: a review. J Mater Eng Perform. 2014;23:1917–28.
100. Qin J, Hu F, Liu Y, Witherell P, Wang CCL, Rosen DW, et al. Research and application of machine learning for additive manufacturing. Addit Manuf. 2022 Apr;52:102691.
101. Mahmoudi M, Aziz Ezzat A, Elwany A. Layerwise Anomaly Detection in Laser Powder-Bed Fusion Metal Additive Manufacturing. J Manuf Sci Eng. 2018 Nov 28;141.
102. Zhang Y, Hong GS, Ye D, Zhu K, Fuh JYH. Extraction and evaluation of melt pool, plume and spatter information for powder-bed fusion AM process monitoring. Mater Des [Internet]. 2018;156:458–69. Available from: https://www.sciencedirect.com/science/article/pii/S026412751830532X
103. Ren Z, Gao L, Clark SJ, Fezzaa K, Shevchenko P, Choi A, et al. Machine learning–aided real-time detection of keyhole pore generation in laser powder bed fusion. Science (80-). 2023 Jan;379(6627):89–94.
104. Li W, Lambert-Garcia R, Getley ACM, Kim K, Bhagavath S, Majkut M, et al. AM-SegNet for additive manufacturing in situ X-ray image segmentation and feature quantification. Virtual Phys Prototyp. 2024 Dec;19(1).
105. Chen R, Sodhi M, Imani M, Khanzadeh M, Yadollahi A, Imani F. Brain-inspired computing for in-process melt pool characterization in additive manufacturing. CIRP J

Manuf Sci Technol. 2023 Apr;41:380–90.
106. Grasso M, Laguzza V, Semeraro Q, Colosimo BM. In-process monitoring of selective laser melting: spatial detection of defects via image data analysis. J Manuf Sci Eng. 2017;139(5):51001.
107. Yadav P, Singh VK, Joffre T, Rigo O, Arvieu C, Le Guen E, et al. Inline Drift Detection Using Monitoring Systems and Machine Learning in Selective Laser Melting. Adv Eng Mater. 2020;22(12).
108. Baumgartl H, Tomas J, Buettner R, Merkel M. A deep learning-based model for defect detection in laser-powder bed fusion using in-situ thermographic monitoring. Prog Addit Manuf. 2020;5(3):277–85.
109. Williams J, Dryburgh P, Clare A, Rao P, Samal A. Defect Detection and Monitoring in Metal Additive Manufactured Parts through Deep Learning of Spatially Resolved Acoustic Spectroscopy Signals. Smart Sustain Manuf Syst. 2018 Nov;2:20180035.
110. Dongsen Y, Fuh J, Zhang Y, Hong GS, Zhu K. Defects Recognition in Selective Laser Melting with Acoustic Signals by SVM Based on Feature Reduction. IOP Conf Ser Mater Sci Eng. 2018 Oct 23;436:12020.
111. Gobert C, Reutzel EW, Petrich J, Nassar AR, Phoha S. Application of supervised machine learning for defect detection during metallic powder bed fusion additive manufacturing using high resolution imaging. Addit Manuf. 2018;21:517–28.
112. Caggiano A, Zhang J, Alfieri V, Caiazzo F, Gao R, Teti R. Machine learning-based image processing for on-line defect recognition in additive manufacturing. CIRP Ann. 2019;68(1):451–4.
113. Scime L, Beuth J. A multi-scale convolutional neural network for autonomous anomaly detection and classification in a laser powder bed fusion additive manufacturing process. Addit Manuf [Internet]. 2018;24:273–86. Available from: https://www.sciencedirect.com/science/article/pii/S2214860418305165
114. Mojahed Yazdi R, Imani F, Yang H. A hybrid deep learning model of process-build interactions in additive manufacturing. J Manuf Syst. 2020;57:460–8.
115. Gaikwad A, Imani F, Yang H, Reutzel EW, Rao P. In Situ Monitoring of Thin-Wall Build Quality in Laser Powder Bed Fusion Using Deep Learning. Smart Sustain Manuf Syst. 2019 Nov 12;3.
116. Imani F, Gaikwad A, Montazeri M, Rao P, Yang H, Reutzel E. Process mapping and in-process monitoring of porosity in laser powder bed fusion using layerwise optical imaging. J Manuf Sci Eng. 2018;140(10):101009.
117. Yuan B, Giera B, Guss G, Matthews I, McMains S. Semi-Supervised Convolutional Neural Networks for In-Situ Video Monitoring of Selective Laser Melting. 2019 IEEE Winter Conf Appl Comput Vis. 2019;744–53.
118. Okaro IA, Jayasinghe S, Sutcliffe C, Black K, Paoletti P, Green PL. Automatic fault detection for laser powder-bed fusion using semi-supervised machine learning. Addit Manuf. 2019;27:42–53.
119. Montazeri M, Nassar AR, Dunbar AJ, Rao P. In-process monitoring of porosity in additive manufacturing using optical emission spectroscopy. IISE Trans. 2020;52(5):500–15.
120. Seifi SH, Tian W, Doude H, Tschopp M, Bian L. Layer-Wise Modeling and Anomaly

Detection for Laser-Based Additive Manufacturing. J Manuf Sci Eng. 2019 May 31;141:1.
121. Guo W, Tian Q, Guo S, Guo Y. A physics-driven deep learning model for process-porosity causal relationship and porosity prediction with interpretability in laser metal deposition. CIRP Ann. 2020 May 1;69.
122. Gaja H, Liou F. Defect classification of laser metal deposition using logistic regression and artificial neural networks for pattern recognition. Int J Adv Manuf Technol. 2018 Jan 1;94.
123. Khanzadeh M, Chowdhury S, Tschopp MA, Doude HR, Marufuzzaman M, Bian L. In-situ monitoring of melt pool images for porosity prediction in directed energy deposition processes. IISE Trans. 2019 May;51(5):437–55.
124. Jafari-Marandi R, Khanzadeh M, Tian W, Smith B, Bian L. From in-situ monitoring toward high-throughput process control: cost-driven decision-making framework for laser-based additive manufacturing. J Manuf Syst. 2019;51:29–41.
125. Francis J, Bian L. Deep Learning for Distortion Prediction in Laser-Based Additive Manufacturing using Big Data. Manuf Lett. 2019;20:10–4.
126. Zhang B, Liu S, Shin YC. In-Process monitoring of porosity during laser additive manufacturing process. Addit Manuf. 2019;28:497–505.
127. Gonzalez Val C, Pallas A, Panadeiro V, Rodriguez A. A convolutional approach to quality monitoring for laser manufacturing. J Intell Manuf. 2020 Mar 1;31.
128. Chen L, Yao X, Xu P, Moon S, Bi G. Rapid surface defect identification for additive manufacturing with in-situ point cloud processing and machine learning. Virtual Phys Prototyp. 2020 Oct 15;16.
129. Zhang Y, Hong GS, Dongsen Y, Fuh J, Zhu K. Powder-Bed Fusion Process Monitoring by Machine Vision With Hybrid Convolutional Neural Networks. IEEE Trans Ind Informatics. 2019 Nov 26;PP:1.
130. Tapia G, Elwany A, Sang H. Prediction of Porosity in Metal-based Additive Manufacturingusing Spatial Gaussian Process Models. Addit Manuf. 2016 May 1;12.
131. Minkowitz L, Arneitz S, Effertz PS, Amancio-Filho ST. Laser-powder bed fusion process optimisation of AlSi10Mg using extra trees regression. Mater Des. 2023 Mar;227:111718.
132. Mooraj S, Kim G, Fan X, Samuha S, Xie Y, Li T, et al. Additive manufacturing of defect-free TiZrNbTa refractory high-entropy alloy with enhanced elastic isotropy via in-situ alloying of elemental powders. Commun Mater. 2024 Feb;5(1):14.
133. Wang J, Jeong SG, Kim ES, Kim HS, Lee BJ. Material-agnostic machine learning approach enables high relative density in powder bed fusion products. Nat Commun. 2023 Oct;14(1):6557.
134. García-Moreno AI, Alvarado Orozco J, Ibarra-Medina J, Martinez Franco E. Image-based porosity classification in Al-alloys by laser metal deposition using random forests. Int J Adv Manuf Technol. 2020 Oct 1;110:1–19.
135. Lu ZL, Li DC, Lu BH, Zhang A, Zhu GX, Pi G. The prediction of the building precision in the Laser Engineered Net Shaping process using advanced networks. Opt Lasers Eng - OPT LASER ENG. 2010 May 1;48:519–25.
136. Gihr M, Rashid A, Melkote SN. Bead geometry prediction and optimization for corner

structures in directed energy deposition using machine learning. Addit Manuf [Internet]. 2024;84:104080. Available from: https://www.sciencedirect.com/science/article/pii/S221486042400126X
137. Wacker C, Köhler M, David M, Aschersleben F, Gabriel F, Hensel J, et al. Geometry and Distortion Prediction of Multiple Layers for Wire Arc Additive Manufacturing with Artificial Neural Networks. Vol. 11, Applied Sciences. 2021.
138. Dang L, He X, Tang D, Xin H, Zhan Z, Wang X, et al. Pore-induced fatigue failure: A prior progressive fatigue life prediction framework of laser-directed energy deposition Ti-6Al-4V based on machine learning. Theor Appl Fract Mech [Internet]. 2024;130:104276. Available from: https://www.sciencedirect.com/science/article/pii/S0167844224000259
139. Sohil F, Sohail M, Shabbir J. An introduction to statistical learning with applications in R: by Gareth James, Daniela Witten, Trevor Hastie, and Robert Tibshirani, New York, Springer Science and Business Media, 2013, $41.98, eISBN: 978-1-4614-7137-7. Stat Theory Relat Fields. 2021 Sep 26;6:1.
140. Goh GD, Sing SL, Yeong WY. A review on machine learning in 3D printing: applications, potential, and challenges. Artif Intell Rev. 2021 Jan 1;54.
141. Li Z, Zhang Z, Shi J, Wu D. Prediction of surface roughness in extrusion-based additive manufacturing with machine learning. Robot Comput Integr Manuf. 2019;57:488–95.
142. Tapia G, Elwany AH, Sang H. Prediction of porosity in metal-based additive manufacturing using spatial Gaussian process models. Addit Manuf. 2016;12:282–90.
143. Tapia G, Khairallah S, Matthews M, King W, Elwany A. Gaussian process-based surrogate modeling framework for process planning in laser powder-bed fusion additive manufacturing of 316L stainless steel. Int J Adv Manuf Technol. 2018 Feb;94.
144. Meng L, Zhang J. Process design of laser powder bed fusion of stainless steel using a Gaussian process-based machine learning model. Jom. 2020;72(1):420–8.
145. Kamath C. Data mining and statistical inference in selective laser melting. Int J Adv Manuf Technol. 2016;86:1659–77.
146. Chowdhury S, Anand S. Artificial neural network based geometric compensation for thermal deformation in additive manufacturing processes. In: International Manufacturing Science and Engineering Conference. American Society of Mechanical Engineers; 2016. p. V003T08A006.
147. Reddy NS, Panigrahi BB, Ho CM, Kim JH, Lee CS. Artificial neural network modeling on the relative importance of alloying elements and heat treatment temperature to the stability of α and β phase in titanium alloys. Comput Mater Sci [Internet]. 2015;107:175–83. Available from: https://www.sciencedirect.com/science/article/pii/S0927025615003511
148. Silbernagel C, Aremu A, Ashcroft I. Using machine learning to aid in the parameter optimisation process for metal-based additive manufacturing. Vol. ahead-of-p, Rapid Prototyping Journal. 2019.
149. Li P, Pei Y, Li J. A comprehensive survey on design and application of autoencoder in deep learning. Appl Soft Comput [Internet]. 2023;138:110176. Available from: https://www.sciencedirect.com/science/article/pii/S1568494623001941

150. Maleki E, Bagherifard S, Guagliano M. Application of artificial intelligence to optimize the process parameters effects on tensile properties of Ti-6Al-4V fabricated by laser powder-bed fusion. Int J Mech Mater Des. 2021;1–24.
151. Wang H, Li B, Zhang W, Xuan F. Microstructural feature-driven machine learning for predicting mechanical tensile strength of laser powder bed fusion (L-PBF) additively manufactured Ti6Al4V alloy. Eng Fract Mech. 2024 Jan;295:109788.
152. Scime L, Joslin C, Collins DA, Sprayberry M, Singh A, Halsey W, et al. A Data-Driven Framework for Direct Local Tensile Property Prediction of Laser Powder Bed Fusion Parts. Materials (Basel). 2023 Nov;16(23):7293.
153. Yang Z, Yang M, Sisson R, Li Y, Liang J. A machine-learning model to predict tensile properties of Ti6Al4V parts prepared by laser powder bed fusion with hot isostatic pressing. Mater Today Commun. 2022 Dec;33:104205.
154. Minerva G, Awd M, Tenkamp J, Walther F, Beretta S. Machine learning-assisted extreme value statistics of anomalies in AlSi10Mg manufactured by L-PBF for robust fatigue strength predictions. Mater Des. 2023 Nov;235:112392.
155. Jia Y, Fu R, Ling C, Shen Z, Zheng L, Zhong Z, et al. Fatigue life prediction based on a deep learning method for Ti-6Al-4V fabricated by laser powder bed fusion up to very-high-cycle fatigue regime. Int J Fatigue. 2023 Jul;172:107645.
156. Moon S, Ma R, Attardo R, Tomonto C, Nordin M, Wheelock P, et al. Impact of surface and pore characteristics on fatigue life of laser powder bed fusion Ti–6Al–4V alloy described by neural network models. Sci Rep. 2021 Oct;11(1):20424.
157. Elangeswaran C, Cutolo A, Gallas S, Dinh TD, Lammens N, Erdelyi H, et al. Predicting fatigue life of metal LPBF components by combining a large fatigue database for different sample conditions with novel simulation strategies. Addit Manuf. 2022 Feb;50:102570.
158. Barrionuevo GO, Walczak M, Ramos-Grez J, Sánchez-Sánchez X. Microhardness and wear resistance in materials manufactured by laser powder bed fusion: Machine learning approach for property prediction. CIRP J Manuf Sci Technol. 2023 Jul;43:106–14.
159. Hassanin H, Zweiri Y, Finet L, Essa K, Qiu C, Attallah M. Laser Powder Bed Fusion of Ti-6Al-2Sn-4Zr-6Mo Alloy and Properties Prediction Using Deep Learning Approaches. Materials (Basel). 2021 Apr;14(8):2056.
160. Lesko CCC, Sheridan LC, Gockel JE. Microhardness as a Function of Process Parameters in Additively Manufactured Alloy 718. J Mater Eng Perform. 2021 Sep;30(9):6630–9.
161. Zhang T, Zhou X, Zhang P, Duan Y, Cheng X, Wang X, et al. Hardness Prediction of Laser Powder Bed Fusion Product Based on Melt Pool Radiation Intensity. Materials (Basel). 2022 Jul;15(13):4674.
162. Zhang W, Desai P. MACHINE LEARNING ENABLED POWDER SPREADING PROCESS MAP FOR METAL ADDITIVE MANUFACTURING (AM). 2017.
163. Kumar P, Jain NK. Surface roughness prediction in micro-plasma transferred arc metal additive manufacturing process using K-nearest neighbors algorithm. Int J Adv Manuf Technol [Internet]. 2022;119(5):2985–97. Available from: https://doi.org/10.1007/s00170-021-08639-2

164. Cao Z, Liu Q, Liu Q, Yu X, Kruzic JJ, Li X. A machine learning method to quantitatively predict alpha phase morphology in additively manufactured Ti-6Al-4V. npj Comput Mater. 2023;9(1):195.
165. Özel T, Shaurya A, Altay A, Yang L. Process monitoring of meltpool and spatter for temporal-spatial modeling of laser powder bed fusion process. Procedia CIRP. 2018;74:102–6.
166. Mani M, Wong YS, Fuh JYH, Loh HT. Benchmarking for comparative evaluation of RP systems and processes. Rapid Prototyp J. 2004 Apr;10:123–35.
167. Zhu Z, Ferreira K, Anwer N, Mathieu L, Guo K, Qiao L. Convolutional Neural Network for geometric deviation prediction in Additive Manufacturing. Procedia CIRP [Internet]. 2020;91:534–9. Available from: https://www.sciencedirect.com/science/article/pii/S2212827120308623
168. Estalaki SM, Lough CS, Landers RG, Kinzel EC, Luo T. Predicting defects in laser powder bed fusion using in-situ thermal imaging data and machine learning. Addit Manuf. 2022 Oct;58:103008.
169. Gobert C, Reutzel EW, Petrich J, Nassar AR, Phoha S. Application of supervised machine learning for defect detection during metallic powder bed fusion additive manufacturing using high resolution imaging. Addit Manuf [Internet]. 2018;21:517–28. Available from: https://www.sciencedirect.com/science/article/pii/S2214860417302051
170. Ye Z, Liu C, Tian W, Kan C. In-situ point cloud fusion for layer-wise monitoring of additive manufacturing. J Manuf Syst [Internet]. 2021;61:210–22. Available from: https://www.sciencedirect.com/science/article/pii/S0278612521001886
171. Kaji F, Nguyen-Huu H, Budhwani A, Narayanan JA, Zimny M, Toyserkani E. A deep-learning-based in-situ surface anomaly detection methodology for laser directed energy deposition via powder feeding. J Manuf Process [Internet]. 2022;81:624–37. Available from: https://www.sciencedirect.com/science/article/pii/S1526612522004297
172. Gaikwad A, Giera B, Guss GM, Forien JB, Matthews MJ, Rao P. Heterogeneous sensing and scientific machine learning for quality assurance in laser powder bed fusion–A single-track study. Addit Manuf. 2020;36:101659.
173. du Plessis A. Effects of process parameters on porosity in laser powder bed fusion revealed by X-ray tomography. Addit Manuf. 2019;30:100871.
174. Jiang R, Smith J, Yi YT, Sun T, Simonds BJ, Rollett AD. Deep learning approaches for instantaneous laser absorptance prediction in additive manufacturing. npj Comput Mater. 2024;10(1):6.
175. Gorgannejad S, Martin AA, Nicolino JW, Strantza M, Guss GM, Khairallah S, et al. Localized keyhole pore prediction during laser powder bed fusion via multimodal process monitoring and X-ray radiography. Addit Manuf. 2023 Sep;78:103810.
176. Sun S, Brandt M, Easton M. 2 - Powder bed fusion processes: An overview. In: Brandt MBTLAM, editor. Woodhead Publishing Series in Electronic and Optical Materials. Woodhead Publishing; 2017. p. 55–77.
177. Thijs L, Verhaeghe F, Craeghs T, Humbeeck J Van, Kruth JP. A study of the microstructural evolution during selective laser melting of Ti–6Al–4V. Acta Mater.

2010;58(9):3303–12.
178. Sadowski M, Ladani L, Brindley W, Romano J. Optimizing quality of additively manufactured Inconel 718 using powder bed laser melting process. Addit Manuf. 2016;11:60–70.
179. Ara I, Azarmi F, Tangpong XW. Microstructure Analysis of High-Density 316L Stainless Steel Manufactured by Selective Laser Melting Process. Metallogr Microstruct Anal [Internet]. 2021;10(6):754–67. Available from: https://doi.org/10.1007/s13632-021-00798-8
180. Behjat A, Shamanian M, Iuliano L, Saboori A. Laser powder bed fusion in situ alloying of AISI 316L-2.5%Cu alloy: microstructure and mechanical properties evolution. Prog Addit Manuf. 2024;
181. Ukey K, Rameshchandra Sahu A, Sheshrao Gajghate S, Kumar Behera A, Limbadri C, Majumder H. Wire electrical discharge machining (WEDM) review on current optimization research trends. Mater Today Proc. 2023;
182. Spierings A, Schneider M, Eggenberger R. Comparison of Density Measurement Techniques for Additive Manufactured Metallic Parts. Rapid Prototyp J. 2011 Aug;17:380–6.
183. Casalino G, Campanelli SL, Contuzzi N, Ludovico AD. Experimental investigation and statistical optimisation of the selective laser melting process of a maraging steel. Opt Laser Technol. 2015;65:151–8.
184. Obaton AF, Lê MQ, Prezza V, Marlot D, Delvart P, Huskic A, et al. Investigation of new volumetric non-destructive techniques to characterise additive manufacturing parts. Weld World. 2018 Jun;62.
185. Standard Guide for Additive Manufacturing of Metal — Finished Part Properties — Methods for Relative Density Measurement. 10.04:6.
186. Kruth JP, Bartscher M, Carmignato S, Schmitt R, Chiffre L, Weckenmann A. Computed tomography for dimensional metrology. Cirp Ann Technol - CIRP ANN-MANUF TECHNOL. 2011 Dec;60:821–42.
187. Hsieh J. Computed Tomography: Principles, Design, Artifacts, and Recent Advances. In 2003.
188. Toorandaz S, Taherkhani K, Liravi F, Toyserkani E. A novel machine learning-based approach for in-situ surface roughness prediction in laser powder-bed fusion. Addit Manuf. 2024;91:104354.
189. Sohrabpoor H, Salarvand V, Lupoi R, Chu Q, Li W, Aldwell B, et al. Microstructural and mechanical evaluation of post-processed SS 316L manufactured by laser-based powder bed fusion. J Mater Res Technol. 2021;12:210–20.
190. Goldberg DE, Holland JH. Genetic algorithms and Machine Learning. Mach Learn. 1988;3:95–9.
191. Ballard Z, Brown C, Madni AM, Ozcan A. Machine learning and computation-enabled intelligent sensor design. Nat Mach Intell. 2021;3(7):556–65.
192. Sui X, Downing JR, Hersam MC, Chen J. Additive manufacturing and applications of nanomaterial-based sensors. Mater Today. 2021 Sep;48:135–54.
193. Razvi SS, Feng S, Narayanan A, Lee YT, Witherell P. A Review of Machine Learning Applications in Additive Manufacturing. 2019.

194. Wang Z, Liu P, Ji Y, Mahadevan S, Horstemeyer M, hu Z, et al. Uncertainty Quantification in Metallic Additive Manufacturing Through Physics-Informed Data-Driven Modeling. JOM. 2019 Jun;71:1–10.